Characterization and electronic properties of moiré superlattices in van der Waals heterostructures

A thesis submitted to the University of Manchester

for the degree of Doctor of Philosophy

in the Faculty of Science and Engineering

2019

Yibo Wang

Department of Physics and Astronomy

in the School of Natural Sciences

List of Contents

List of Figures

List of Tables

List of Abbreviations

2D	Two-dimensional materials
hBN	Hexagonal boron nitride
TMDCs	Transition metal dichalcogenides
0D	Zero-dimensional
1D	One-dimensional
3D	Three-dimensional
QHEs	Quantum Hall effects
SEM	Scanning electron microscope
CVD	Chemical vapour deposition
BN	Boron nitride
rBN	Rhombohedral BN
cBN	Cubic BN
wBN	Wurtzite BN
STM	Scanning Tunnelling Microscope
AFM	Atomic Force Microscopy
PID	Proportional-integral-derivative
C-AFM	Conductive mode AFM
QNM	Quantitative Mechanical Property Mapping
EFM	Electrostatic Force Microscopy
KPFM	Kelvin Probe Force Microscopy
PL	Photoluminescence
EBL	Electron Beam Lithography
PMMA	Polymethylmethacrylate
PMGI	Polymethylglutarimide
PDMS	Polydimethylsiloxane
DI	Deionzed

Abstract

This work is dedicated to the studies of novel van der Waals heterostructures using atomic force microscopy, Raman spectroscopy, cryogenic magnetotransport measurements and convergent beam electron holographic technique. We start from the description of the fundamental properties of graphene and related two-dimensional materials, and then turn to discuss the methodology used to obtain the main results presented in this work. In particular, a detailed description of the procedures used to fabricate complex van der Waals heterostructures, to which this thesis is devoted, along with the operation principles of the advanced modes of atomic force microscopy will be given.

The scientific problems which had been investigated in the thesis are listed as **I.** The electronic transport properties of composite super-moiré superlattices in double aligned graphene heterostructures. **II.** The strain-induced piezoelectricity in monolayer hexagonal boron nitride. **III.** Convergent beam electron holography for analysis of van der Waals heterostructures.

When one two-dimensional material is brought into a close proximity to another one, the forming of moiré pattern leads to alteration of electronic and excitonic spectra and crystal reconstruction. In this thesis, we developed an approach to align graphene with two hexagonal boron nitride (hBN) simultaneously. This approach results in electron scattering by the differential moiré potentials, which can have arbitrarily large wave-vector and, thus alter the band structure at arbitrary low energies.

The second part of this thesis is devoted to two-dimensional (2D) hBN, which is a wide-bandgap van der Waals crystal with remarkable properties, including exceptional strength, large oxidation resistance at high temperatures and single-photon emission. Due to the non-centrosymmetric of monolayer hBN, it has been predicted to exhibit piezoelectric properties, but no experimental evidence yet. In this case, we use the method: strain-induced piezoelectricity by bubbles forming from monolayer hBN on graphene, with the help of atomic force microscopy and electrostatic force microscopy to observe the piezoelectric behaviour. No piezoelectricity was found in bilayer and bulk hBN, where the centre of symmetry is restored. These results make monolayer hBN a desirable candidate for novel electromechanical and stretchable optoelectronic devices.

Finally, we perform the studies of van der Waals heterostructures by means of newly developed convergent beam electron holographic technique which allows imaging of the stacking order in such heterostructures, reconstruction of relative rotation, stretching, and out-of-plane corrugation of the layers with atomic precision and extraction of quantitative information about the 3D structure of the typical defects.

Declaration

I declare that no portion of the work referred to in the thesis has been submitted in support of an application for another degree or qualification of this or any other university or other institute of learning.

Copyright statement

Acknowledgements

Many thanks should be given to everyone in School of Physics and Astronomy who helped me for my learning and practising during PhD time. Also, to stuffs in National Graphene Institute who support students a practical and fine working environment.

Among all of these,

I would gratefully to say ‘thank you’ to show my highest respect to my PhD supervisor Prof. Sir Kostya Novoselov, who give me a chance to study in this group, support and help me a lot since the beginning of my PhD. His patience to students and wonderful skills in operating any machine inspired me a lot. As a brilliant scientist, his unique ideas and persistence in science set me an excellent example in my life.

I would also want to acknowledge my highly respect and appreciation to Dr. Colin Woods, who taught me the operation of all versions Atomic Force Microscopy machines hand by hand from the beginning without any preservation. Not only than that, he also taught me skills from basic sample fabrication till final characterization steps. As an fabrication expert, there are still a lot I should learn from him.

I would like to share my thankful to my group members Alexey Berdyugin, Dr. Denis Bandurin, Dr. Davit Ghazaryan, Prof. Yang Cao, Prof. Sheng Hu, Prof. Kaige Zhou, Dr. Lee Hague, Dr. Alexander Zhukov, Dr. Artem Mishchenko etc. and all other people in the group, who taught me a lot in physics and sample fabrication skills in cleanroom.

I would share my deeply thankful to my mother, who support me without any condition during my study time in life.

Chapter 1

Graphene and other two-dimensional materials

1.1 Introduction

In this chapter, the properties of graphene, and other two-dimensional (2D) materials, such as hexagonal boron nitride (hBN) and transition metal dichalcogenides (TMDCs) are discussed. Starting with the discovery of carbon allotropes, atomic orbitals and the electronic band structures of graphene and production methods, a fundamental introduction to graphene is presented. The atomic structures and electronic properties of hBN and TMDCs as other 2D materials, compared with graphene, are discussed. The unique indirect-direct bandgap transition properties of TMDCs and the optoelectronic applications are reviewed.

1.2 Discovery of Graphene allotropes

As the basic compound element in life, carbon plays an important role in fundamental research. Various carbon-based materials with different physical properties have appeared over time and their discoveries have constituted significant milestones in the scientific world. Due to highly flexible molecular chains, carbon compounds present different characteristics in different structures[1]. Starting from the basic understanding of carbon atoms, some allotropes, such as fullerenes, carbon nanotube, and graphene are discussed[1]. Fullerenes are spherical molecules containing carbon atoms arranged in pentagonal and hexagonal lattices[2]. Fullerenes are considered as zero-dimensional (0D) objects[3]. Carbon nanotubes[4] are in roll shaped tube formations with carbon atoms in one-dimensional (1D) hexagonal lattices[3]. Graphene has a single layer of carbon atoms packed in a honeycomb structure, with a two-dimensional (2D) hexagonal lattice[3], shown in Fig. 1.1.

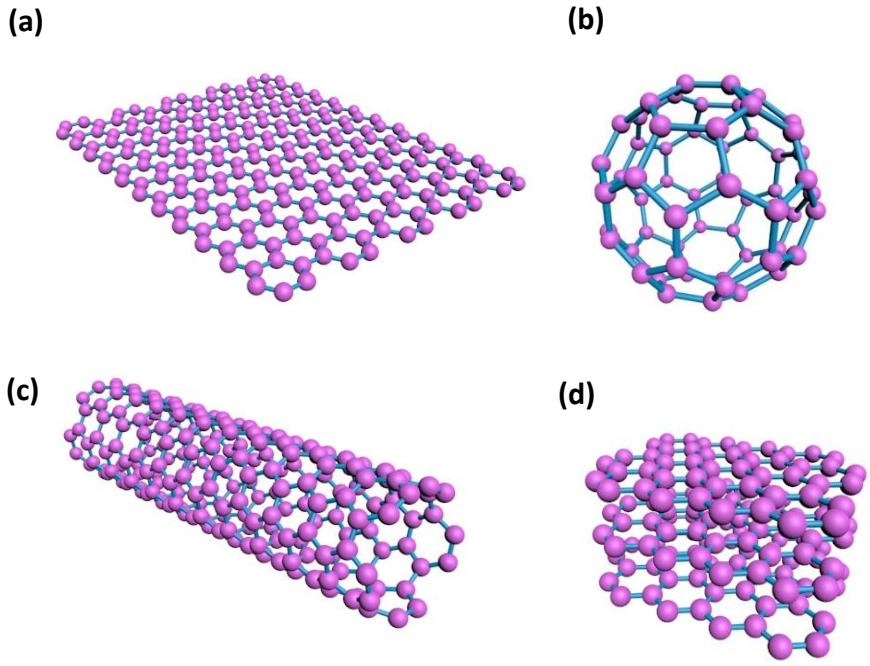

Fig. 1. 1 Structure of graphene, fullerene, carbon nanotube and graphite. (a) Graphene with carbon atoms in a hexagonal lattice. (b) Fullerenes with carbon atoms pack in pentagonal and hexagonal lattices. (c) Graphene rolls into cylinders as nanotube (1D). (d) Stacks with number of layers as graphite (3D)[3]. Image taken from Reference[1].

The isolation of graphene from bulk graphite is one of the most important scientific works of this century, achieved by K.S. Novoselov and A.K. Geim in the University of Manchester[5]. Graphene has brought about tremendous results in the scientific community although it had been described as a 'state that could not exist' 70 years ago[3].

In 1935[6], Landau and Peierls argued that infinite two-dimensional crystals are not stable upon thermal fluctuations and were predicted to curl up and form 3D islands[3,7]. The only known exception was 2D films epitaxially grown on monocrystals with matching crystal lattice (see e.g. Refs[8-9]).This has been regarded as the only experimentally effective method of producing atomically thin films[3,11,12].

It was only in 2004, as the first 2D single layer carbon atoms were isolated from graphite by mechanical exfoliation[5], that graphene proved that single layer carbon atoms could exist freely without a monocrystal base. Also, it could exist perfectly well on membranes[13] and in liquid suspension[14].

Graphene is characterized by numerous excellent properties, such as exceptional mechanical stiffness, one of the highest among other materials electrical and thermal conductivity[15,16]. The versatile properties combined in graphene have led to it's being hailed as a once in a century breakthrough material that is expected to revolutionise the world. The fact that high-quality, clean graphene[16] can be obtained in a simple and economical way in a laboratory has accelerated research on graphene and other 2D materials. Research has proved that graphene reaches the limit of theoretical prediction of its many properties, such as high room-temperature electron mobility (up to $2.5 \times 10^5 cm^2 V^{-1} s^{-1}$)[17], high thermal conductivity[18], high density of electric current sustainability[19] and so on.

1.3 Atomic orbitals of Graphene

Carbon is an element that can create versatile compounds due to different types of bonds (single, double and triple)[20]. In order to understand the carbon bonds formed in graphite, the electronic configuration[20] of carbon in its ground state, and its orbit hybridisation format[20] are discussed below.

In general, the electronic configuration of the carbon atom in its ground state[20] is expressed as $1s^2 2s^2 2p^2$, and the four valance electrons that are available for bonding are expressed as $2s^2 2p^2$. Because the forming of bonds decreases the system energy, the reconfiguration of valance electrons takes place and this is referred to as '*hybridization*'[20]. In short, only sp, sp^2, sp^3 hybridizations are discussed in Fig. 1.2.

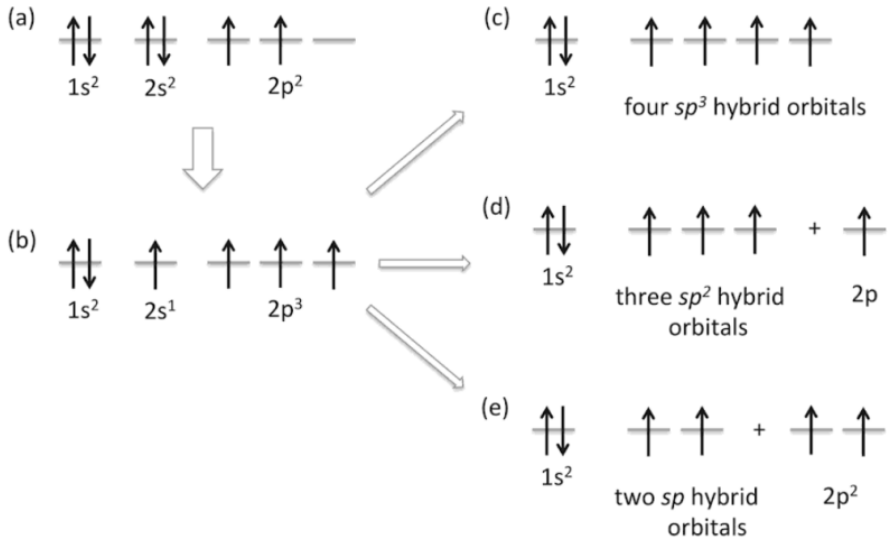

Fig. 1. 2 sp, sp^2, sp^3 hybridizations of electrons in carbon atom. (a) Electrons in ground state (b) excited state (c) sp^3 hybridization (d) sp^2hybridization (e) sp hybridization. Image taken from Reference[20].

When hybridization occurs, one electron in $1s$ orbital is promoted into $2p_z$ orbital, to form an excited state[20]. The electrons in the carbon atom start to hybridize from the excited state into sp, sp^2, sp^3 hybrid orbitals. Graphite consists of stacked layers of sp^2 hybridized carbon atoms located in a hexagonal lattice. The $2s$ and $2p_x$, $2p_y$ orbitals hybridise to sp^2 hybrid orbitals with one electron filled in each[20]. The newly formed orbitals have trigonal planar geometry with an orbital angle of 120°[20] (Fig. 1.3). The remaining $2p_z$ orbital (not involved in hybridization) is located perpendicular to this plane[20]. The three sp^2 hybrid orbitals form a σ covalent bond (which determines the energy stability and elasticity of graphene) with their nearest neighbours, and the $2p_z$ orbital forms delocalised π bonds in layers[20] with adjacent paralleled neighbours. The interaction between layers is weak[20] and this makes graphite easier to exfoliate.

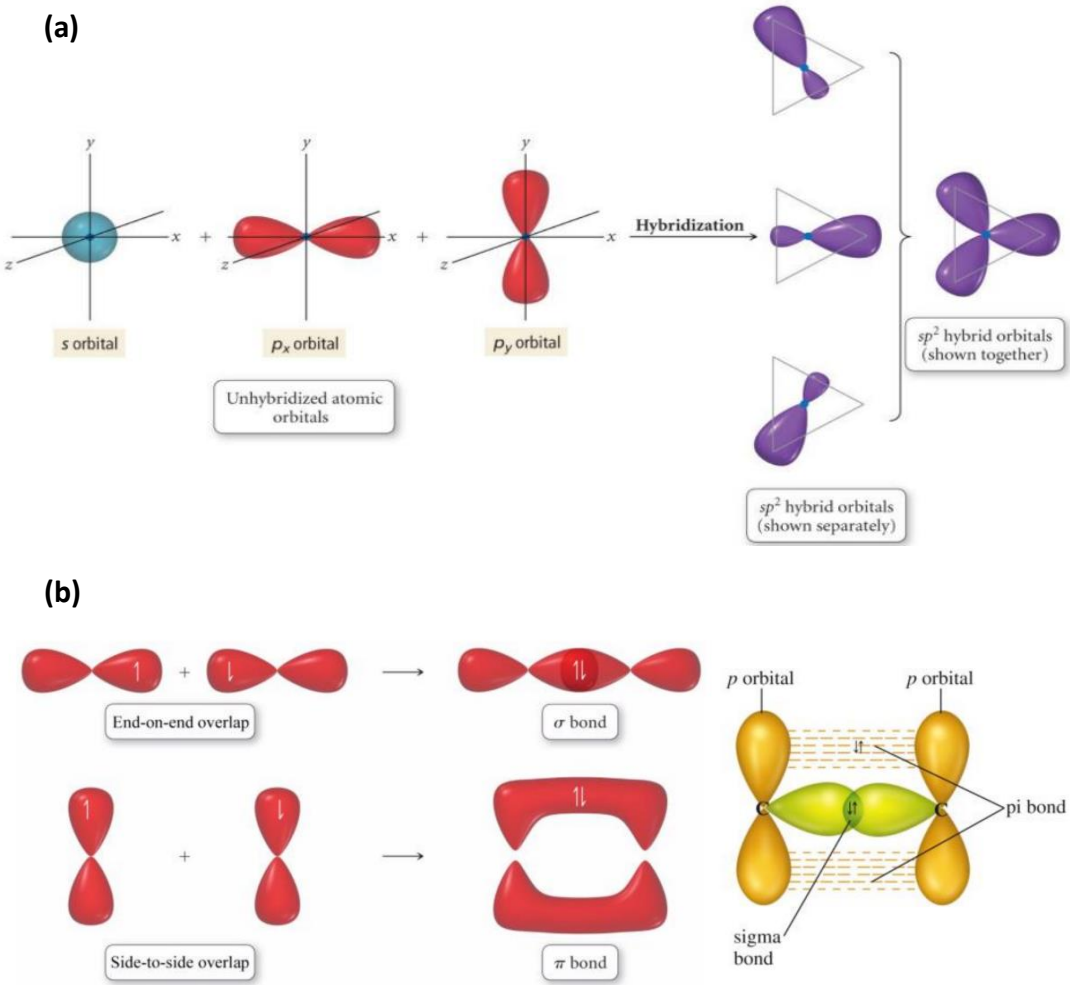

Fig. 1. 3 Orbital hybridization and bond overlaps. (a) $\boldsymbol{sp^2}$ hybrid orbitals. One $\boldsymbol{s}$ orbital and two $\boldsymbol{p}$ orbitals hybridize to $\boldsymbol{sp^2}$ orbitals, with trigonal planar geometry with orbital angle of 120°. (b) $\boldsymbol{sp^2}$ hybrid orbitals end-on-end overlap to form $\boldsymbol{\sigma}$ bond, remaining $\boldsymbol{2p_z}$ orbital side-to-side overlap to form $\boldsymbol{\pi}$ bond. Image taken from Reference[21].

1.4 Electronic band structure of Graphene

The carbon atoms of graphene are arranged in hexagonal lattice[1], the structure can be considered as two atoms (A and B) contained in triangular Bravais lattice per unit cell, shown in Fig.1.4(a)[1].

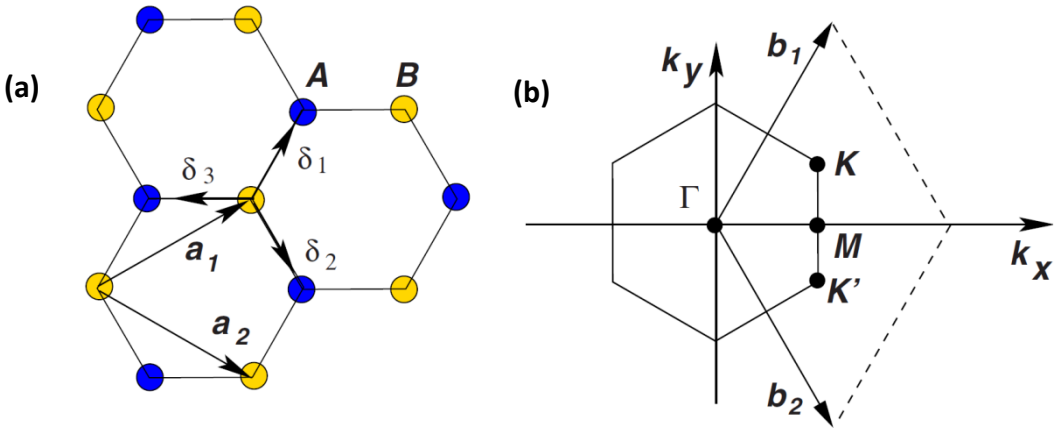

Fig. 1. 4 Graphene Bravais lattice and Brillouin zone. (a) Carbon atoms from graphene in hexagonal lattice. (b) Graphene Brillouin zone. Image taken from Reference[1].

The lattice constant vectors are expressed as $(\boldsymbol{a_1}, \boldsymbol{a_2})$[1]

$$\boldsymbol{a_1} = \frac{a}{2}(3, \sqrt{3}), \qquad \boldsymbol{a_2} = \frac{a}{2}(3, -\sqrt{3}),$$

where $a \approx 1.42\text{Å}$ is the carbon-carbon distance[1]. Blue dots and yellow dots represent Type A atoms and Type B atoms respectively. Also, the reciprocal lattice constant vectors $(\boldsymbol{b_1}, \boldsymbol{b_2})$ are expressed as[1],

$$\boldsymbol{b_1} = \frac{2\pi}{3a}(1, \sqrt{3}), \qquad \boldsymbol{b_2} = \frac{2\pi}{3a}(1, -\sqrt{3})$$

By the function[22] $\boldsymbol{a_i} \cdot \boldsymbol{b_j} = 2\pi\boldsymbol{\delta_{ij}} = \begin{cases} 2\pi & (i = j) \\ 0 & (i \neq j) \end{cases} \quad (i, j = 1, 2)$

There are two points in the corners of graphene Brillouin zone expressed as K and K'[20]. In momentum space their positions can be expressed as[1]:

$$\boldsymbol{K} = \left(\frac{2\pi}{3a}, \frac{2\pi}{3\sqrt{3}a}\right), \qquad \boldsymbol{K'} = \left(\frac{2\pi}{3a}, -\frac{2\pi}{3\sqrt{3}a}\right),$$

In real space, the three vectors of adjacent carbon atoms are expressed as[1]:

$$\delta_1 = \frac{a}{2}(1, \sqrt{3}), \qquad \delta_2 = \frac{a}{2}(1, -\sqrt{3}), \qquad \delta_3 = -a(1,0)$$

The six vectors of secondly-adjacent carbon atoms are expressed as[1]:

$$\delta_1' = \pm \boldsymbol{a_1}, \qquad \delta_2' = \pm \boldsymbol{a_2}, \qquad \delta_3' = \pm(\boldsymbol{a_2} - \boldsymbol{a_1}),$$

The tight-binding Hamiltonian model is used for modelling electronic band structure and the electrons can hop to nearest[1]. The energy bands derived from this Hamiltonian are expressed as[20,23,24]:

$$E_{\pm}(k_x, k_y) = \pm t\sqrt{1 + 4\cos\left(\frac{\sqrt{3}k_x a}{2}\right)\cos\left(\frac{k_y a}{2}\right) + 4\cos^2\frac{k_y a}{2}}$$

where $k = (k_x, k_y)$ belongs to the first Brillouin zone, E_+ refers to upper π^* band and E_- refers to lower π band; t ($\approx 2.8\ eV$) is the nearest hopping energy[1,23]. The graphene full band structure is shown in Fig. 1.5 below, from which it can already be seen that in the vicinity of the K and K' points bands disperse linearly with increasing momentum. The valence band and conduction band are symmetrical at the *K* point in the Brillouin zone, where the Fermi level of charge neutral graphene is positioned. (Each Bravais lattice contains two carbon atoms, each carbon atom contributes one π electron, thus the graphene valence band is full and the conduction band is empty[1]. The Fermi level of the charge neutral graphene is therefore located exactly between the conduction band and the valence bands)[1]. The energy spectrum is symmetric at zero energy.

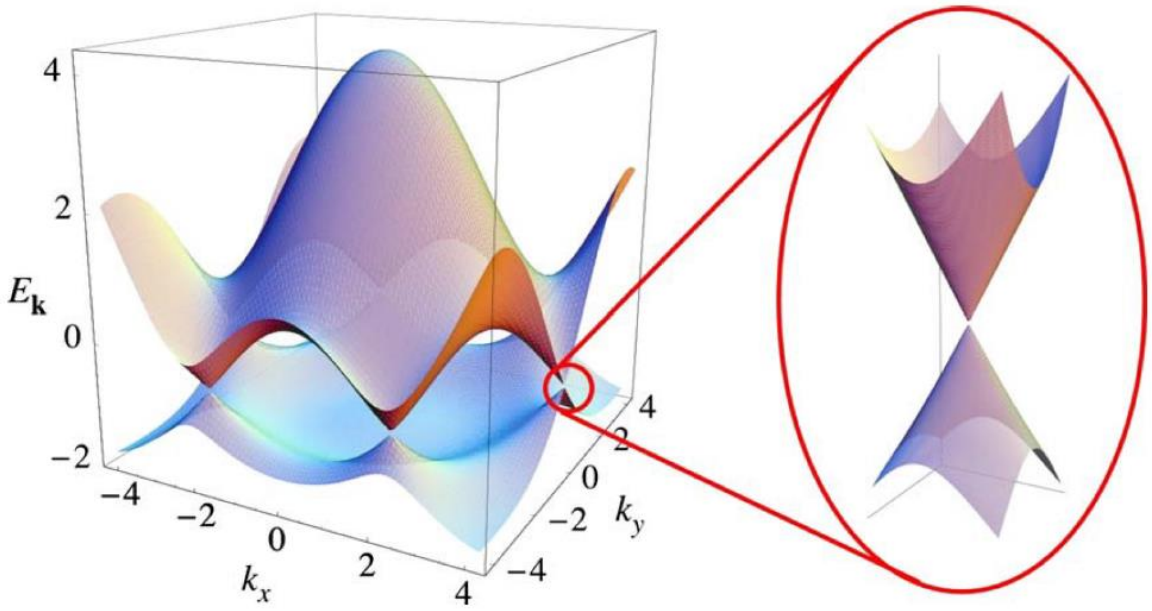

Fig. 1. 5 Full band structure of graphene. Image taken from Reference[1].

A zoomed-in image of the dispersion relation in the vicinity of the K (or K') points is shown in Fig. 1.5. At K and K' points, the dispersion can be obtained by substitution $\mathbf{k}$ as $\mathbf{k} = \mathbf{K} + \mathbf{q}$, with $|\mathbf{q}| \ll \mathbf{K}$, [24]

$$E_{\pm}(\mathbf{q}) \approx \pm v_F|\mathbf{q}| + [(q/K)^2]$$

where $\boldsymbol{q}$ is momentum relative to Dirac points, $v_F = 3ta/2$ $(\simeq 1 \times 10^6\ m/s)$[1] is the Fermi velocity[1,24]. Note, unlike conventional two-dimensional electron gases, the Fermi velocity in graphene is momentum-independent[1].

1.5 Mechanical exfoliation of Graphene from Graphite

Monolayer graphene is produced by a mechanical exfoliation method using 'scotch tape'[5]. This technique provides clean graphene with a defect-free structure on a substrate. The exfoliation method is based on repeatedly peeling off bulk graphite on the scotch tape surface and applying normal force or sheer force on the graphite layers (shown in Fig. 1.6(a))[25]. The graphite layers become thinner and expose increasingly fewer layers, or single layer graphene in the process[25]. The graphene flake under Scanning electron microscope (SEM) presents zigzag and armchair edges, shown in Fig. 1.6(b)[3].

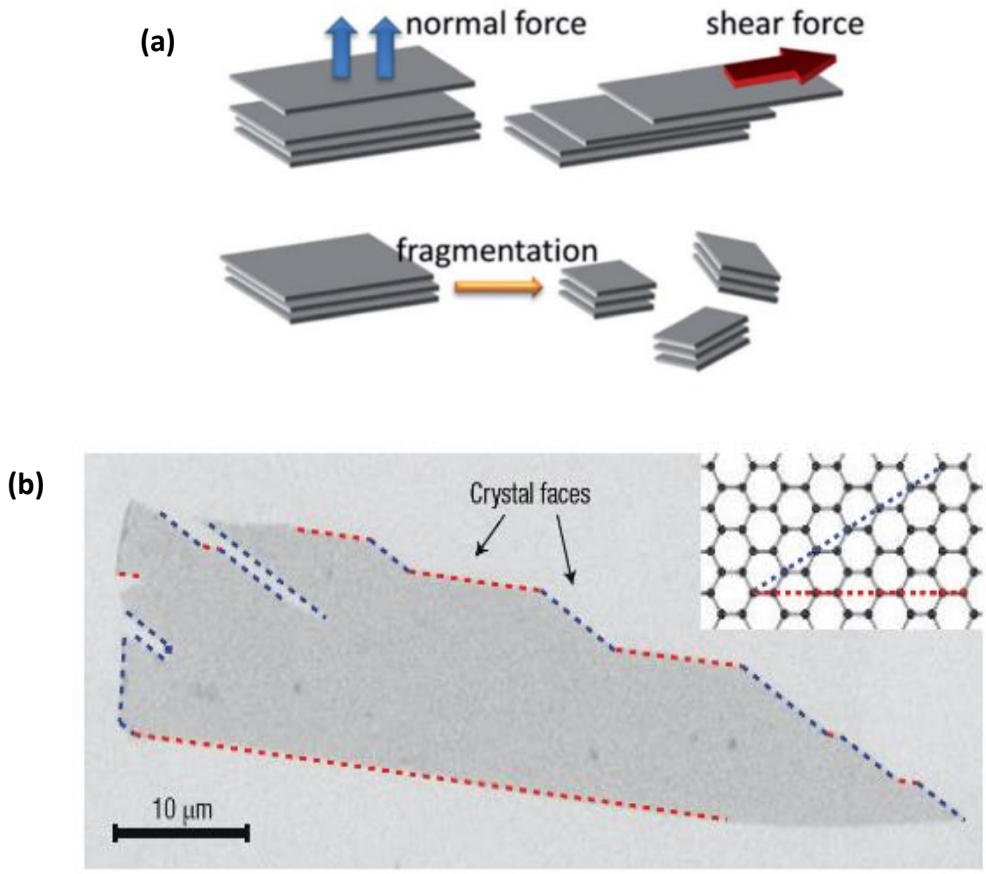

Fig. 1. 6 Exfoliation process and graphene crystal under SEM. (a) Scenarios of mechanical exfoliation route in graphite exfoliation, results from normal force, shear force or fragmentation[25]. (b) Large graphene crystal with zigzag (blue lines) and armchair (red lines) edges[3]. Image taken from Reference[3,25].

1.6 Chemical vapour deposition (CVD) growing Graphene

In recent years, a new method of growing graphene, named chemical vapour deposition (CVD), has attracted a great deal of attention (Fig. 1.7)[26]. Graphene is grown on the surface of a matrix by dehydrogenation at high temperature, using carbon compounds (CH_4, C_2H_2, etc.) as a carbon source[27]. By using catalytic substrates, such as copper foil or other metal substrates (Ni, Pt, etc.)[27], or even insulating substrates (hBN, SiO_2)[27], graphene can be grown uniformly with fewer grain boundaries[27]. In comparison with reduced graphene oxide or graphene epitaxially grown on silicon carbide, the CVD copper method provides high-quality graphene in large sizes (30 inches)[27,28,29].

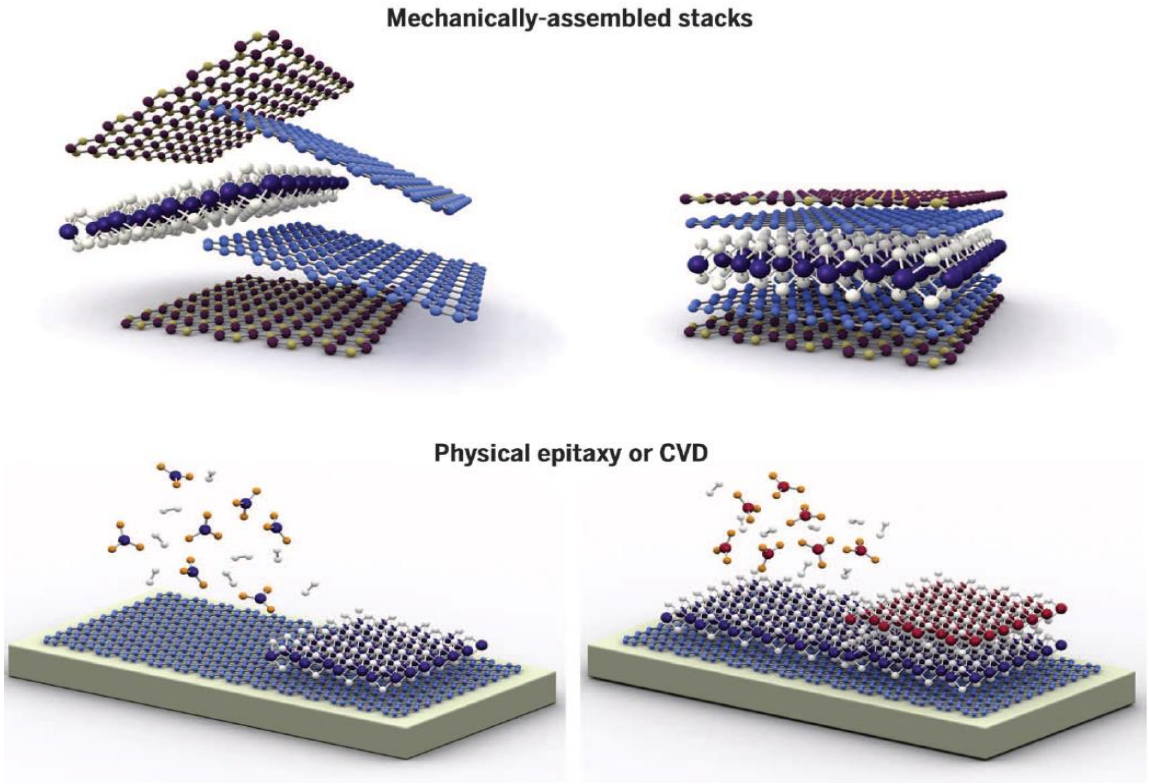

Fig. 1. 7 Schematic comparison of mechanically-assembled stacks and physical epitaxy or CVD method[26]. Image taken from Reference[26].

Usually, the graphene crystals obtained by the CVD method tend to be multi-crystalline, so that the grain boundaries are formed by a series of heptagon-pentagon pairs[30], shown in Fig. 1.8(a). The existence of grain boundaries alters the mechanical and electronic properties[31] of graphene sheets, shown in Fig. 1.8(b) and (c)[30]. The elastic modulus and

breaking force of graphene sheets are decreased by force indentation along the grain boundaries[30,32].

In addition, the electronic properties display an increased resistance across boundary areas[33], which is suspected to be due to additional scattering[33], shown in Fig. 1.8(d) and (e)[33].

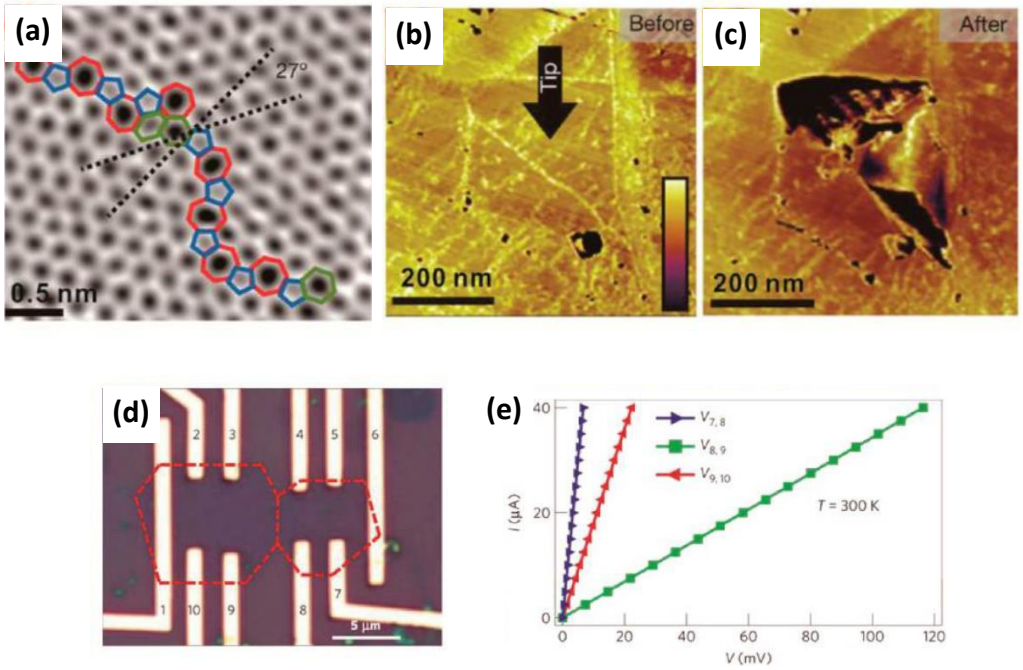

Fig. 1. 8 CVD graphene grain boundaries, strain resistance and electronic properties. (a) Grain boundaries with aperiodic heptagon-pentagon pairs. AFM force indentation before (b) and after (c) along grain boundaries area[30]. (d) optical images of contacts on CVD graphene with grain boundaries. (e) Increased resistance (green line) across boundary areas[33]. Image taken from Reference[30,33].

In order to obtain millimetre-sized graphene grains by the CVD method, pre-treatment of Cu foil before the process is studied. The variations used are: electrochemically-polished[31] and high-pressure annealed Cu foils[31] (Fig. 1.9(a)), Cu foil enclosed structures, Cu melted and re-solidified, and oxygen-enriched Cu foils[31]. All of these methods are focused on making a smooth Cu foil surface to provide a flat substrate for growing graphene uniformly[31].

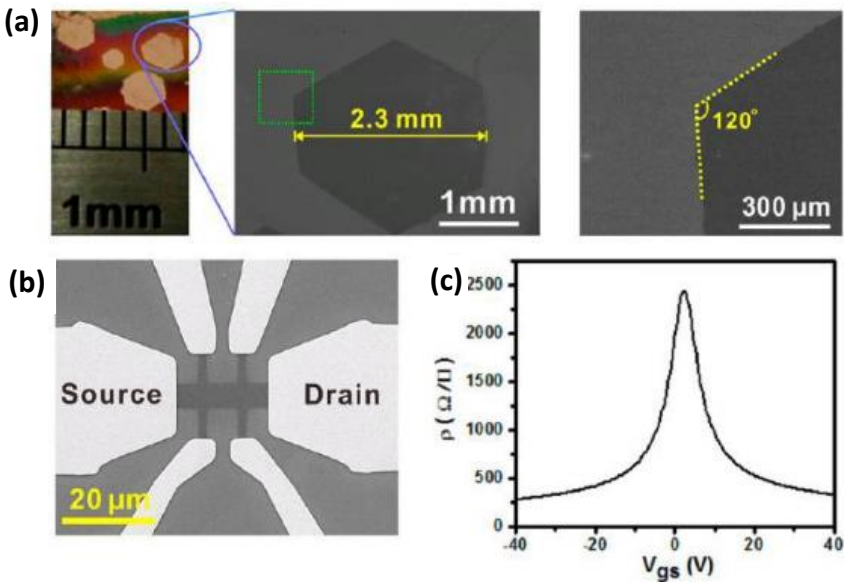

Fig. 1. 9 CVD graphene grains scale. (a) Monolayer graphene grains in millimetre-scale (2.3mm with 120º angle grain boundaries)[31]. (b) Exfoliated graphene device and (c) carrier mobility[31]. Image taken from Reference[31].

Fig. 1.9 (a) shows the monolayer graphene grains obtained by electrochemical polishing and high-pressure controlled pre-treatments[31]. The methods remove Cu protection layers (for avoiding wrinkles and defects) and anneal Cu foils at 2 atm (H_2) in the CVD system for 7 hrs[31, 34]. Millimetre-scale graphene grains with fewer wrinkles and defects were synthesized[34]. Also, the CVD graphene produced in this way displays high carrier mobility at $1.1 \times 10^5 cm^2 V^{-1} s^{-1}$[35] ((b) and (c) is exfoliated graphene).

1.7 Other 2D materials

1.7.1 Hexagonal boron nitride (h-BN)

Boron nitride (BN) is a compound of boron and nitrogen, which has a similar crystal structure and properties to natural carbon[36]. BN polymorphs have four different crystalline structures: hexagonal BN (h-BN), rhombohedral BN (rBN), cubic BN (cBN) and wurtzite BN (wBN)[36]. Each of them has a parallel with a carbon allotrope, e.g. hBN with graphite, rBN with rhombohedral graphite, cBN with diamond, wBN with lonsdaleite (wurtzitic diamond)[36].

A particularly interesting structure is hBN, a layered honeycomb-like crystal lattice with boron and nitrogen atoms occupying an inequivalent A and B sublattices in a Bernal structure[37]. The hexagonal layers of hBN are stacked in sequence as form AA'AA'[38].

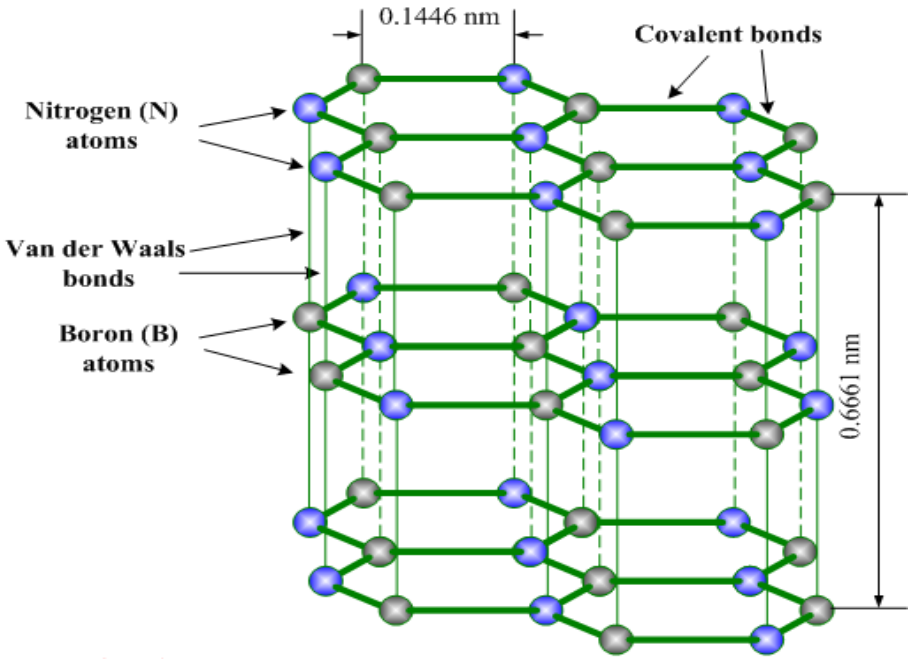

Fig. 1. 10 Lattice structure of hBN. Nitrogen (N) atoms are with blue colour and Boron (B) atoms are with grey colour. The B and N atoms are combined with covalent bonds[36]. Different layers are combined with van der Waals force[36].Image taken from Reference[39].

The sp^2 hybridisation of atom orbitals in this layered structure builds strong covalent bonds σ between boron and nitrogen atoms in each lattice, although the interatomic bond between each of the layers is weak[36]. The two atoms (B and N) in the crystal have

different electronegativity[36]. The electronegativity of the N atom is higher, which makes the π electron locate mostly near the N atom [36] making hBN is a perfect insulator.

Over the past years, hBN is considered as the most suitable substrate to improve the quality of graphene devices[38]. The reason being is hBN's atomically flat surface, the ability to synthesize free from impurities crystals and high energy of optical phonons. Moreover, due to the high-temperature stability and large breakdown electric field strength of $0.7V/nm^{-1}$, hBN can work as an excellent gate insulating substrate for a graphene devices[38,40]. It can also avoid surface roughness and scattering caused by charged surface states and the impurities[41,42] of SiO_2, so that it further increases carrier mobility[43].

The original work was done by Dean et al.[38], and their electronic transport measurements of monolayer graphene on hBN substrate showed steadily improving results (Fig. 1.11 below). The sharp resistivity peaks corresponding to overall charge neutrality points appear at near-zero gate voltage[38]

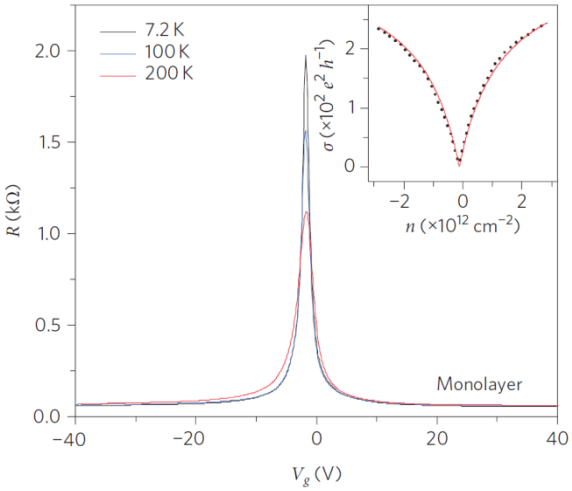

Fig. 1. 11 Resistance of monolayer graphene on hBN as a function of backgate voltage. Conductivity as function of carrier density (inset)[38]. Image taken from Reference[38].

1.7.2 Transition metal dichalcogenides (TMDCs)

1.7.2.1 Atomic structure of TMDCs

Transition metal dichalcogenides (TMDCs) are a group of materials with the formula MX_2 (M represents transition metal and X represents chalcogen)[26]. TMDCs have a wide range of electronic properties (from insulating to semiconducting). The transition metal comes from the IV (Ti, Zr etc.), V (V, Nb etc.) and VI (Cr, Mo, W etc.) groups; the chalcogen elements are S, Se or Te[44]. TMDCs also have a hexagonal structure, with each monolayer consists of three layers of stacked atoms[26]. The transition metal atoms are packed in between two layers of chalcogen atoms with the form X-M-X, shown in Fig. 1.12.

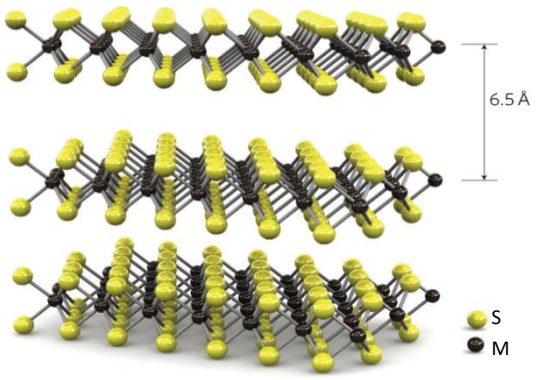

Fig. 1. 12 Layered structures of X-M-X in TMDCs. M represents transition metal, X represents chalcogen. Image taken from Reference[45].

As with graphene and other 2D materials, TMDCs can be produced by mechanical exfoliation from bulk crystal; some other promising techniques have also been developed. One of the methods, named liquid phase[44] preparations, can obtain large quantities of thin TMDC layers, which can be further used in synthesising composites[46,47].

At the same time, CVD growth on a metal substrate[48] and epitaxial growth on SiC substrates[49] is also used to provide uniform large-area layers[44]. Fig. 1.13 shows some of the CVD methods used to grow MoS_2[50–52].

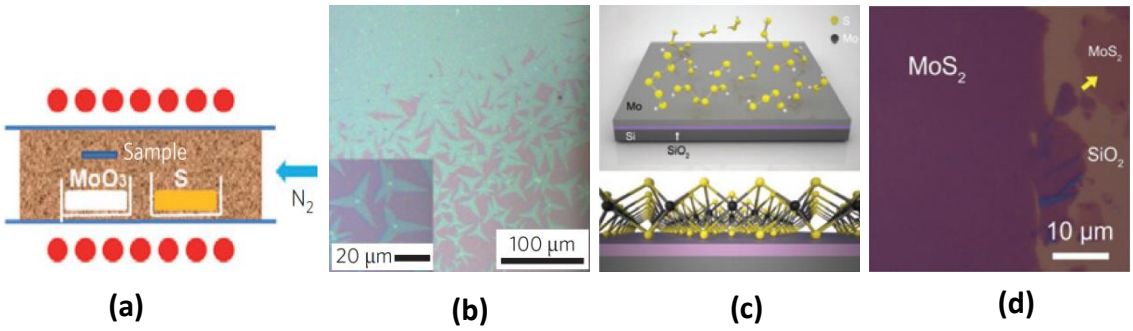

Fig. 1. 13 CVD growing TMDCs process. (a) CVD method with solid S and MoO_3 precursors filled with N_2 resulting (b) MoS_2 film. Red dots represent furnace heating[44]. (c) CVD method with solid Mo layer exposed in S vapour resulting (d) MoS_2 layers[44]. Image taken from Reference[44].

1.7.2.2 Electronic properties of TMDCs

TMDCs have a wide range of electronic and optical properties. In some semiconducting TMDCs (i.e. MoS_2), the transition from indirect bandgap (1.2 eV in bulk) to direct bandgap (1.8 eV in monolayer) occurs[44]. The direct bandgap leads to photoluminescence and predicts further application in optoelectronics[44]. Fig.1.14 shows the different band structures of monolayer and bulk MoS_2 and WS_2[44].

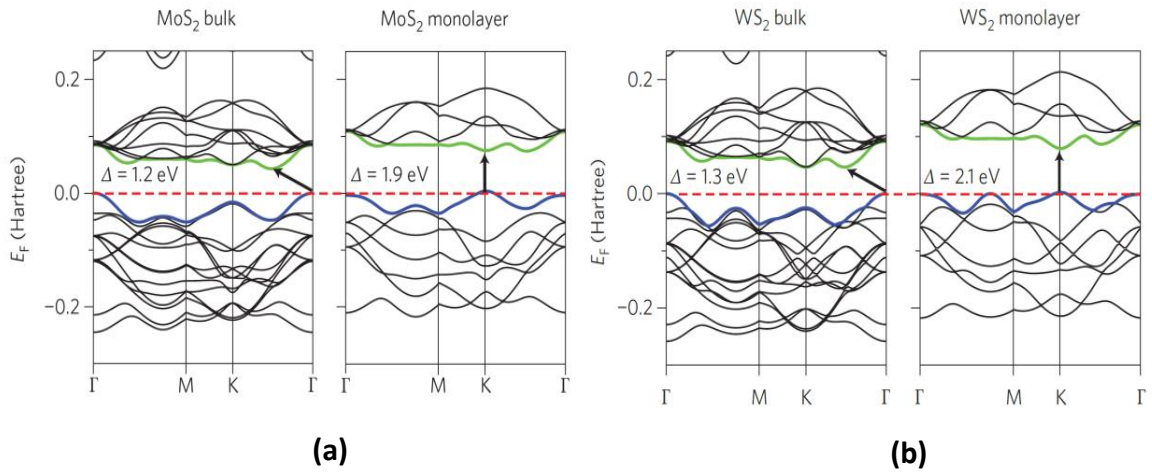

Fig. 1. 14 Band structures of bulk and monolayer (a) MoS_2 and (b) WS_2. The arrow refers bandgap pointing from top valance band (blue) and bottom conduction band (green)[44]. Image taken from Reference[44].

Bulk MoS_2 is characterized by an indirect band gap at Γ point. With decreasing thickness down to monolayer, MoS_2 undergoes indirect-to-direct band gap transition. The direct band gap of monolayer MoS_2 emerges at K, K' points of the Brillouin zone[44]. This is because the quantum confinement in the monolayer leads to the change of hybridization on the p_z orbitals (S atoms) and d orbitals (Mo atoms)[44,53-55]. At K point, the d orbitals (located on the Mo atoms) in the middle sandwich layer of S-Mo-S have not been affected by interlayer coupling[44]. However, at Γ point, the combination of anti-bonding p_z orbitals (S atoms) and d orbitals (Mo atoms) provides strong interlayer coupling[44,54]. Also, it has been found that all MoX_2 and WX_2 materials go through a similar indirect–direct bandgap transition from bulk to thin layers, with a bandgap energy range from 1.1–1.9 eV[55–61].

1.7.2.3 Optical properties of TMDCs

The indirect–direct transition increases the bandgap energy, which further affects the optical properties of TMDCs. For MoS_2, the changes in photoluminescence and photoconductivity are observed[44] with the indirect–direct transition[62,53,54].

The photoluminescence quantum yield rises up to 10^4 factor for monolayer MoS_2 compared to bulk MoS_2[44]. Fig. 1.15 shows a higher quantum yield in the suspended regions of the MoS_2 monolayer in holes.[53]

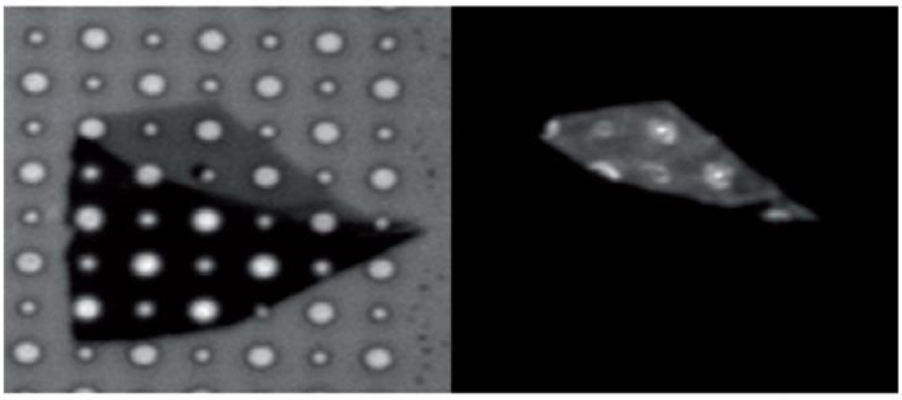

Fig. 1. 15 Photoluminescence of suspended MoS_2 flake. (a) Optical images and (b) photoluminescence of suspended monolayer and multilayer MoS_2 flake on top of holes. Enhanced photoluminescence emission is detected in monolayer region in (b). Image taken from Reference[44].

It has also been shown that there is a strong photoluminescence (PL) in thin-layer MoS_2 crystals, while bulk MoS_2 almost PL-inactive[54]. The reason being is that bulk MoS_2 is an indirect band gap semiconductor and therefore the radiative recombination of excited electron-hole pairs is suppressed. In contrast, MoS2 monolayer has a direct band gap which results in its strong PL activity[54]. Thus, the direct-bandgap monolayer TMDCs ideally have light-emitting properties that could be used in future optoelectronics[44]. Fig. 1.16 shows the photoluminescence spectra of MoS_2 flakes of different thickness.[44]

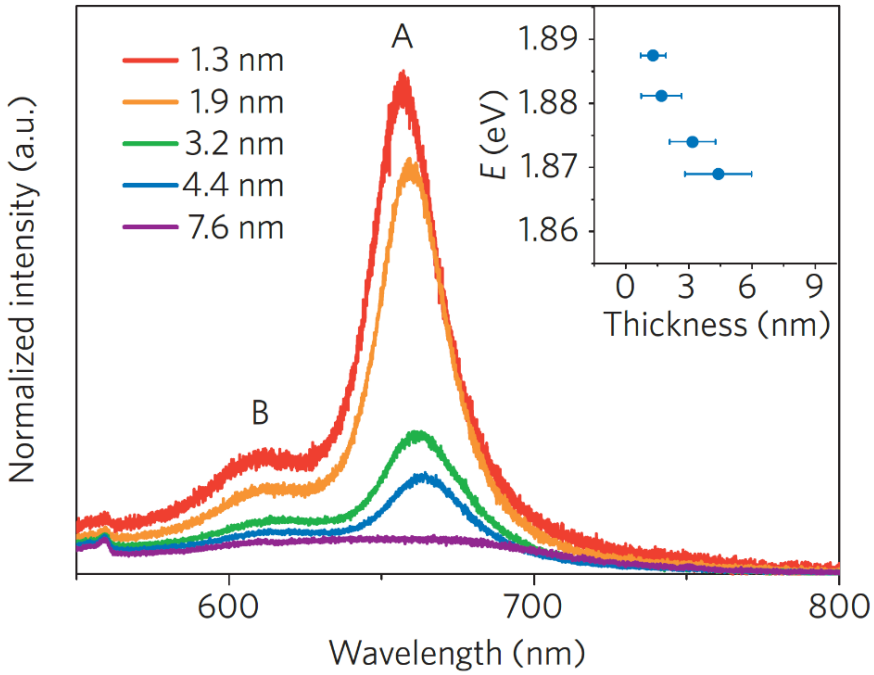

Fig. 1. 16 The photoluminescence spectrum intensity of MoS_2 with different thickness (1.3 to 7.6nm). Inset is A exciton peak energy varies with thickness. Image taken from Reference[44].

Recent studies[63,64] have also reported that moiré superlattices in TMDC heterostructures modify the optical properties of both intra- and interlayer excitons[63]. In $MoSe_2$/ MoS_2-aligned heterostructures, the in-plane periodic potential leads to the splitting of $MoSe_2$ exciton and trion in the emission absorption spectrum[63]. By comparing the PL spectrum of the hBN-encapsulated $MoSe_2$ monolayer and the hBN-encapsulated $MoSe_2/MoS_2$ $\sim 0^{\circ}$ stacking angle aligned heterostructure, the splitting of exciton is shown in the reflectivity spectrum, as seen in Fig. 1.17[63].

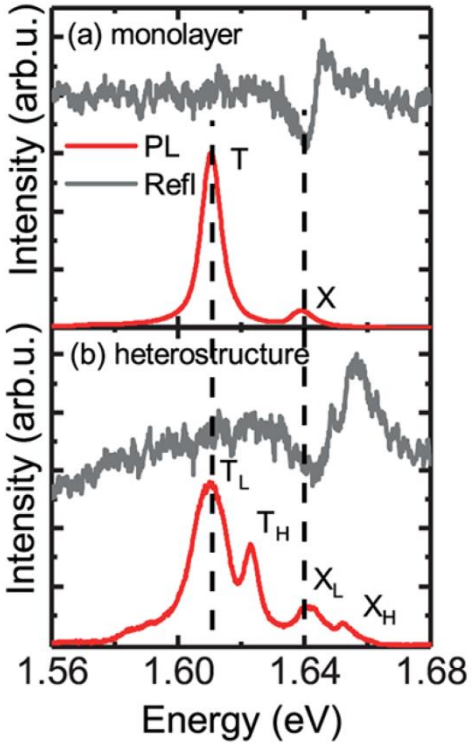

Fig. 1. 17 The photoluminescence spectrum intensity difference of hBN encapsulated monolayer MoS_2 and hBN encapsulated aligned $MoSe_2/MoS_2$. Image taken from Reference[63].

Chapter 2

Graphene based van der Waals heterostructures

2.1 Introduction

In this chapter, moiré superlattices of graphene hBN heterostructure are introduced. The wavelength and relative rotation angle between two lattices are discussed. The electronic properties of the new generated sets of Dirac points and Raman intensity changing with alignment are presented. Also, the wavelength changing with the rotation angle of different TMDCs heterostructures are calculated.

2.2 Moiré pattern

Moiré pattern is first introduced by Rayleigh from the near superposition of two sets equispaced parallel straight lines[65].This phenomenon is then further modified by J. Guild[66] and Y.Nishijima referring that moiré pattern could also be obtained from replica gratings[67] and sets of circular figures[67].

In general, moiré pattern means points of intersection of two overlapped figures[68], each figure needs to have periodically wavelength. The period of moiré pattern changes with the intersection angle.[68]

2.3 Graphene on hBN heterostructure moiré superlattices

Based on the topic of 2D materials[69], the small difference $\delta = a_{hBN}/a_G - 1 \approx 1.8\%$ between two crystals lattice constant and misalignment along with each crystallographic axes generate a quasi-periodic hexagonal pattern[69,70], which further referring as moiré superlattices[71,72] (shown in Fig. 2.1).

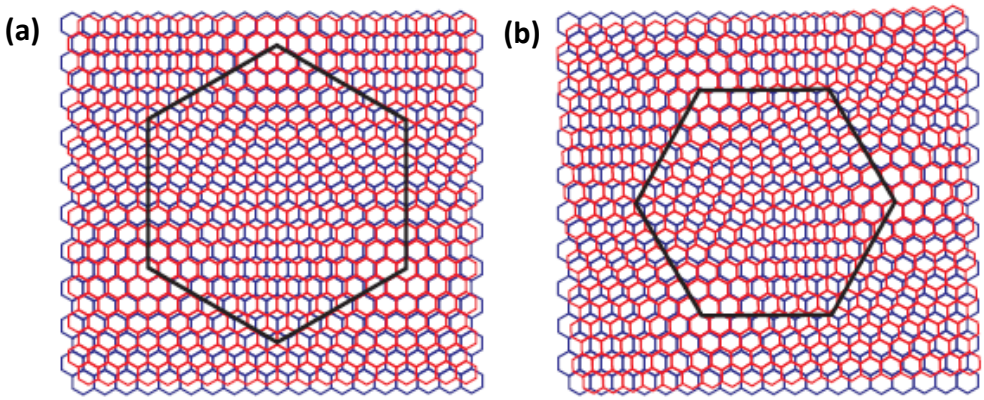

Fig. 2. 1 Moiré superlattices of graphene (red) on hBN (blue) with (a) relative rotation angle $\boldsymbol{\phi = 0°}$and (b) $\boldsymbol{\phi = 3°}$. Image taken from Reference[69].

From the lattice mismatch δ between graphene and hBN, as well as relative rotation angle ϕ between two lattices, the moiré wavelength can be expressed as[73]:

$$\lambda = \frac{(1+\delta)a}{\sqrt{2(1+\delta)(1-\cos\phi)+\delta^2}}$$

Where a is graphene lattice constant[73]. Also, the relative rotation angle θ of moiré superlattices with regard to graphene lattice can be further expressed as[73]:

$$\tan\theta = \frac{\sin\phi}{(1+\delta)-\cos\phi}$$

The moiré wavelength and rotation angle θ as the function of ϕ is shown[73] below in Fig. 2.2. The largest wavelength is up to 14nm[73].

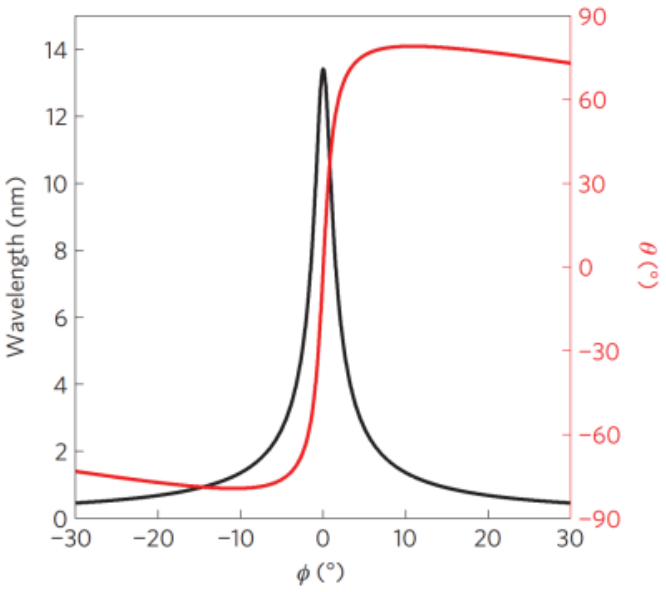

Fig. 2. 2 The wavelength and rotation angle dependence. The wavelength $\boldsymbol{\lambda}$ and relative rotation angle $\boldsymbol{\theta}$ (between moiré superlattices with graphene lattice) as the function of relative rotation angle $\boldsymbol{\phi}$ (between graphene and hBN lattice). Image taken from Reference[73].

2.4 Electronic properties of Graphene hBN superlattices

Superlattices in 2D systems have attracted much interest because of its effect on charge carriers, leading to a modification of the spectra of electronic systems[74]. For the case of the graphene hBN superlattices, second-generation Dirac points appear as sharp peaks in resistivity with the reversal of Hall effect[74]. This indicates that charge carriers change with graphene conduction and valence band[74,75].

Fig. 2.3 (a) shows the behaviour of longitudinal (ρ_{xx}) and Hall resistivities (ρ_{xy}) for graphene hBN aligned samples. The main peak appears at graphene main neutrality point ($n = 0$), and the other two peaks appear on each side of main neutrality point in symmetry, at high doping $n = \pm n_s$[74]. At low temperature, the hole side secondary peak is stronger than its main neutrality point counterpart[74], while the electron side secondary peak is ~10 times weaker[74]. In Fig. 2.3 (b) shows miniband feature of isolated secondary Dirac points. This is because hBN induces extra neutrality points to superlattices potential[74]. It also shows the Hall resistivity (ρ_{xy}) change sign at high electron and hole doping, displaying well-isolated Dirac points[74].

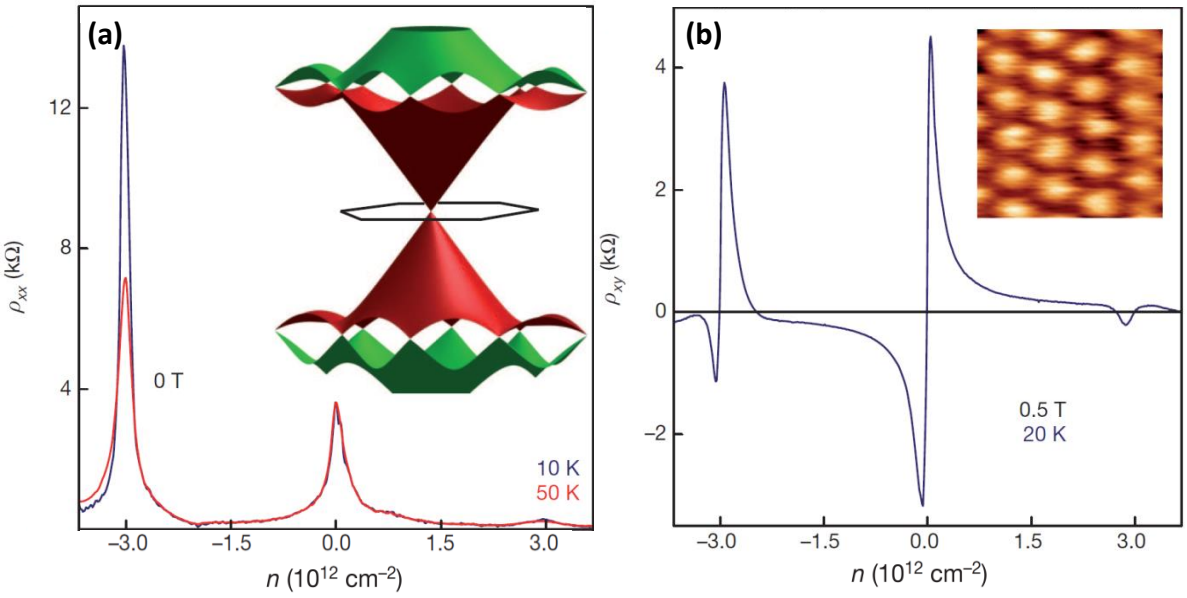

Fig. 2. 3 Electronic properties of graphene hBN superlattices. (a) Longitudinal resistivity ($\boldsymbol{\rho_{xx}}$) and (b) Hall resistivity ($\boldsymbol{\rho_{xy}}$) as a function of $\boldsymbol{n}$ (Positive $\boldsymbol{n}$: electrons, negative $\boldsymbol{n}$: holes) [74]. Image taken from Reference[74]

Previous research[69,76] also investigated the strain distribution and self-rotation in graphene on hBN heterostructures for different misorientation angles along two crystalline structures, by atomic force microscopy (AFM) and Raman spectroscopy[76]. They observe a commensurate-incommensurate transition when ϕ is approximately δ ($\approx 1\%$)[69]. For $\phi < \delta$ (Period $> 10nm$), graphene relaxes to an energetically favourable state[69] for van der Waals interactions with hBN, leading to large areas of commensuratation[69]. For $\phi > \delta$, graphene and hBN lattices keep unsynchronized with no accumulated strain[69].

C.R. Woods et al.[76] prepared graphene on hBN by dry transfer method, and ensured the crystallographic directions of graphene and hBN are misoriented by $\theta = 1° - 2°$[76] by optical observation. They studied the moiré pattern before annealing and after annealing (self-orientation)[76] by AFM and Raman spectroscopy, and observed that uniform alignment and increased level of commensuration[76] happens after annealing. Fig. 2.4 shows the period of moiré pattern increases by 15% which indicates greater alignment[76]. The uniform alignment is also confirmed by Raman spectroscopy[76].

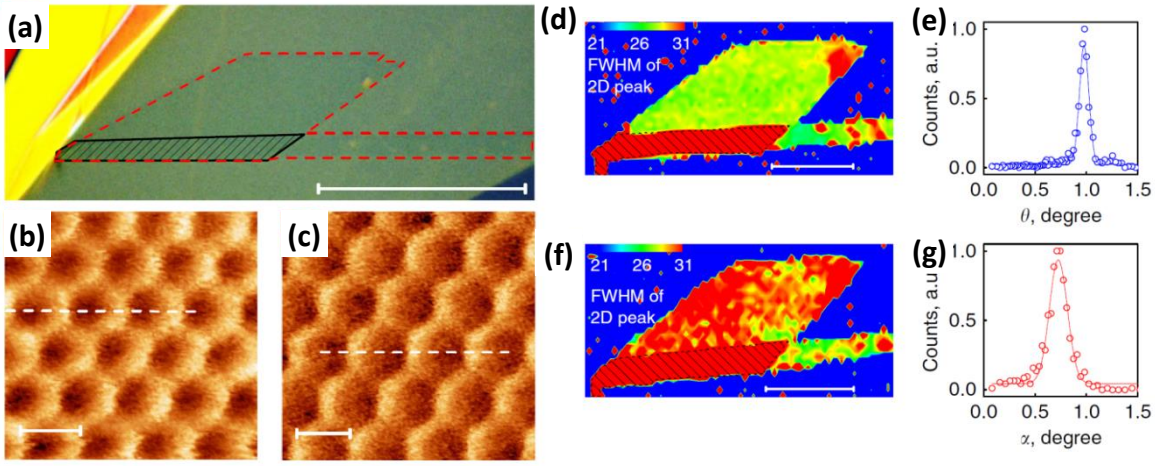

Fig. 2. 4 Optical image, AFM images, and Raman data of graphene hBN superlattices. (a) Young's modulus images of graphene and hBN moiré superlattices before (b) and after (c) annealing. The moiré period increases by 15% and shows clear edges. Corresponding with Raman FWHM 2D peaks and calculated alignment angles before (d,e) and after (f,g) annealing[76]. Image taken from Reference[76].

Chapter 3

Characterization and fabrication techniques

3.1 Introduction

This chapter mainly introduces the techniques of superlattices characterization and device fabrication. Atomic force microscopy is used for surface alignment characterization and heterostructure thickness determination, which count as major part in this work. Raman and photoluminescence spectroscopy provide quick structural characterization for graphene, few-layer graphite and thin layer TMDCs. Electron beam lithography is used for device contacts exposure process.

3.2 Atomic Force Microscopy (AFM)

In 1982, the first Scanning Tunnelling Microscope (STM) was invented by Gerd Binnig and Heinrich[77]. The technique aims at investigating the surface topographies at the atomic scale by using a tunnelling current to finely control distance between a probe and the sample. The principle of STM is relatively straightforward shown in Fig. 3.1. A metal tip scans the surface maintaining a constant tunnel current[77]. The displacement of tip is driven by voltage applied to a piezoelectric tube (piezotube)[77], which is controlled by a feedback loop with the tunnelling current. The surface topographic images are presented as results. The resolution of STM images depends on the tunnelling current between distances of the two tunnel electrodes[77] and how sharp the metallic probe is.

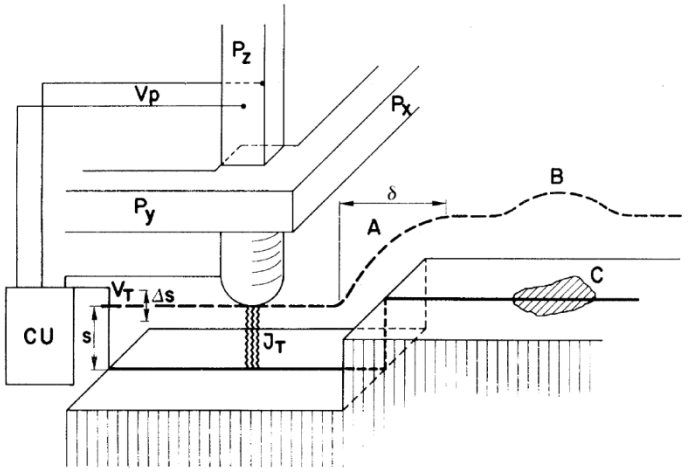

Fig. 3. 1 Schematic of the operation principle of a STM. Piezotubes $\boldsymbol{P_x}$ and $\boldsymbol{P_y}$ control the lateral scan direction of metal tip. CU controller output voltage $\boldsymbol{V_p}$ to piezotube $\boldsymbol{P_z}$ for tunnel current $\boldsymbol{J_T}$ with tunnel voltage $\boldsymbol{V_T}$[77]. The tunnel distance represents by $\boldsymbol{s}$ ($\Delta\,\boldsymbol{s}$). The dash line follows the $\boldsymbol{z}$ displacement in $\boldsymbol{y}$ scan with A (step) B (contamination area) and C (lower work function) [77]. The surface topography images are generated by the voltage applied to $\boldsymbol{P_x}$, $\boldsymbol{P_x}$ and $\boldsymbol{P_y}$ with constant work function[77]. Image taken from Reference[77].

The tunnel current through the tunnel barrier is presented as[77]:

$$J_T \propto \exp\left(-A\varphi^{1/2}s\right),$$

Where $A = \left(\frac{4\pi}{h}\right)2m^{1/2} = 1.025\text{Å}^{-1}eV^{-1/2}$, m is free-electron mass, φ is the average height of the barrier and s is its width[77]. When the tunnel barrier is a few electron-volts, the change of tunnel barrier width due to an atomic step ($\sim 2-5\text{Å}$) [77] causes a variation of tunnel current by up to three orders of magnitude[77].

Subsequently, a variety of Scanning Probe Microscopy (SPM) techniques have been innovated[78]. Among these, is another outstanding technique named Atomic Force Microscopy (AFM). AFM was invented by Gerd Binnig, Christoph Gerber (IBM), Calvin Quate (Stanford) in 1986[79]. The approach aims to measure the electrostatic force between the surface and the tip[80] and record the level of sensitivity of cantilever motion[79] and finally present topographies in high resolution. Importantly, AFM is capable of imaging insulators as well as conductors in the atomic scale, since its feedback is not dependent upon electronic current.

The schematic set up of AFM is shown in Fig. 3.2: a piezoelectric tube controls the distance between the tip and sample surface, meanwhile, a feedback loop converts the laser deflection difference of tip cantilever to electric signal and delivering to display system[80]. By analyzing the signal measured, AFM finally present a 3D atomic surface image.

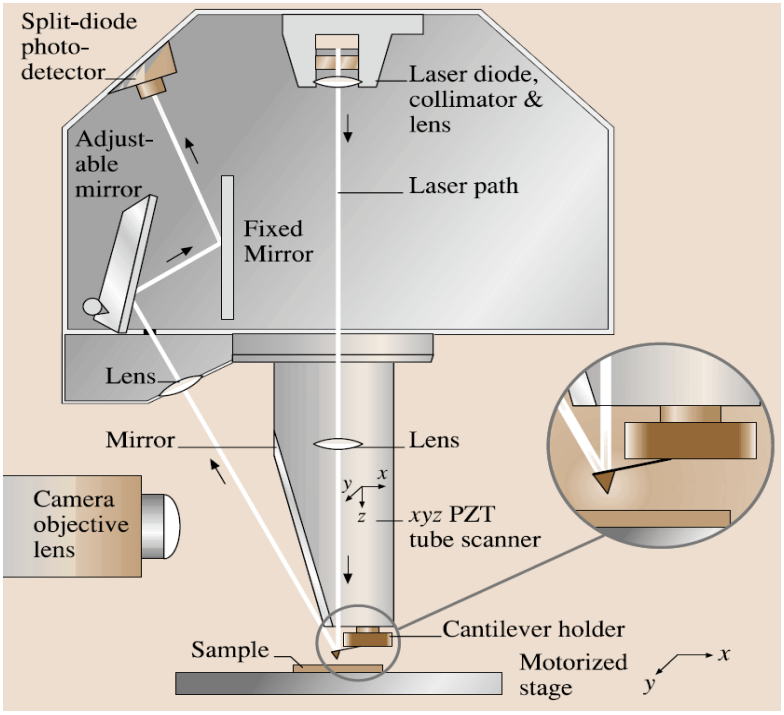

Fig. 3. 2 Schematic setup of AFM and laser cantilever deflection on photodetector. The piezotube locates on top of the cantilever holder. The laser diode goes through lens and reflects on cantilever holder, then catches by an adjustable mirror and arrives on split-diode photodetector. Image taken from Reference[81].

AFM can be operated in mainly four different modes relate with feedback loop, as well as presented different topographic information on different surface. The four modes: tapping mode, contact mode, conductive mode and ramping are discussed below[82].

3.2.1 Contact mode AFM

In contact mode AFM, the tip is in contact with the surface continuously when scanning (shown in Fig. 3.3). The tip is dragged through the sample surface with a constant force (called the setpoint which is typically nN). By recording the cantilever's deflection signal from photodetector, surface topographic information[83] is observed. The tip obtains the compressive force between tip and surface, as well as shear force[83] from cantilever torsion and the later leads to lateral force mode[83].

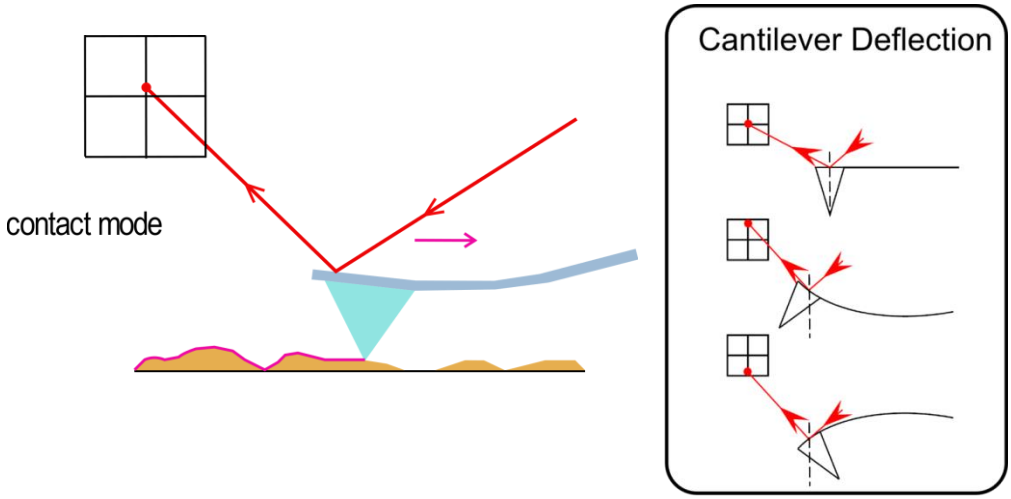

Fig. 3. 3 Schematic demonstration of contact mode AFM. The tip drags through surface and photodetector records cantilever deflection. Image taken from Reference[82].

The output images of contact mode include height, deflection error, and friction. For deflection error images, changes in the topographic image are intensified by deflection signal[84]. Since deflection acts as a feedback parameter, the variation of feature in this channel is considered as 'error'[84]. The feedback loop then compensates the changes to maintain deflection setpoint constantly. In friction images, the friction refers to the torsion from cantilever while scanning. Also, due to the torsion discussed above, another mode named Lateral force microscopy appeared[84].

In Lateral force microscopy, the cantilever scanning movement is perpendicular[84] with the long axis of cantilever (shown in Fig. 3.4). This mode provides the friction signal effectively by measuring cantilever torsion from side to side twisting[84]. Friction force can be converted into an absolute signal by the calibration of cantilever torsion spring constant[84].

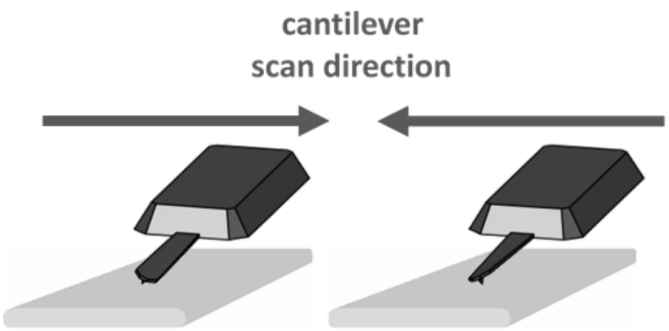

Fig. 3. 4 Cantilever scan direction is perpendicular with long axis of cantilever in Lateral Force mode. Image taken from Reference[84].

3.2.2 Tapping mode

In tapping mode AFM, the cantilever of tip oscillates at a constant frequency with a small amplitude (~10s of nm)[83] near its resonance. During operation of tapping mode, the tip is only affected by the van der Waals interaction for small-time region[83] when surface heights changing. The resonant frequency of the oscillation shifts relative to the free-space resonance. This means the amplitude of the oscillation at a given frequency will move up or down depending on the relative strength of the interaction between the probe and the sample. The piezoelectric tube adjusts vertical position of the tip until the amplitude returns to the setpoint[83]. The feedback loop records the voltage supplied to the piezotube required to maintain the same amplitude[83]. The schematic of a tapping mode AFM set up is shown in Fig. 3.5. The cantilever oscillation is detected by a photodetector, output to lock-in amplifier which obtains the phase and amplitude information. The amplitude signal is compared with set point and the resulting error signal is put to proportional-integral-derivative (PID) controller, which controls the piezo tube[81]. The external unit generates the driving signal to the tip, and provides the reference signal for lock-in amplifier[81].

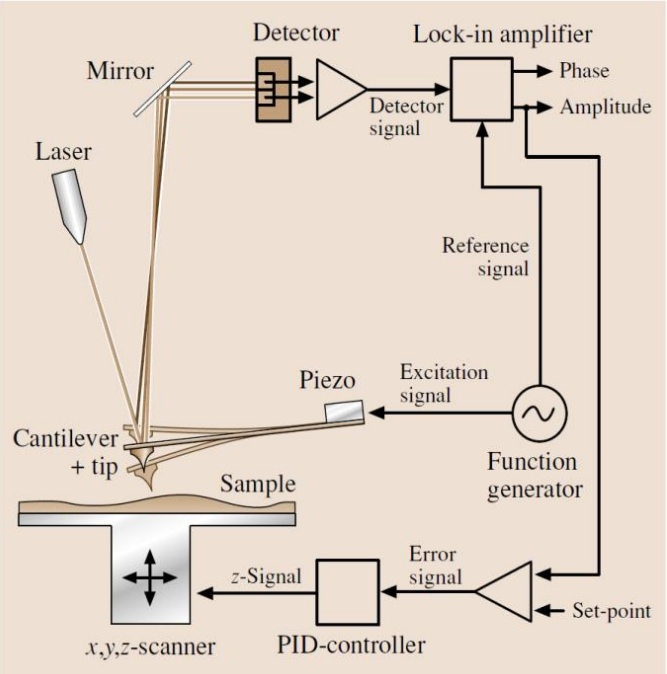

Fig. 3. 5 Schematic set-up of tapping mode AFM. The cantilever oscillates at a constant frequency without touching the surface. Image taken from Reference[81].

Comparing to contact mode, tapping mode avoids lateral force and reduces damage to the tip's sharpness, also providing relatively high-resolution images.

Tapping mode AFM channels include height, amplitude, amplitude error, and phase. The amplitude error channel shows the amplitude difference between actual cantilever oscillation and amplitude setpoint[85]. The phase channel shows to the phase shift between detector signal from cantilever oscillation and drive signal from piezo (Fig.3.6) [86].

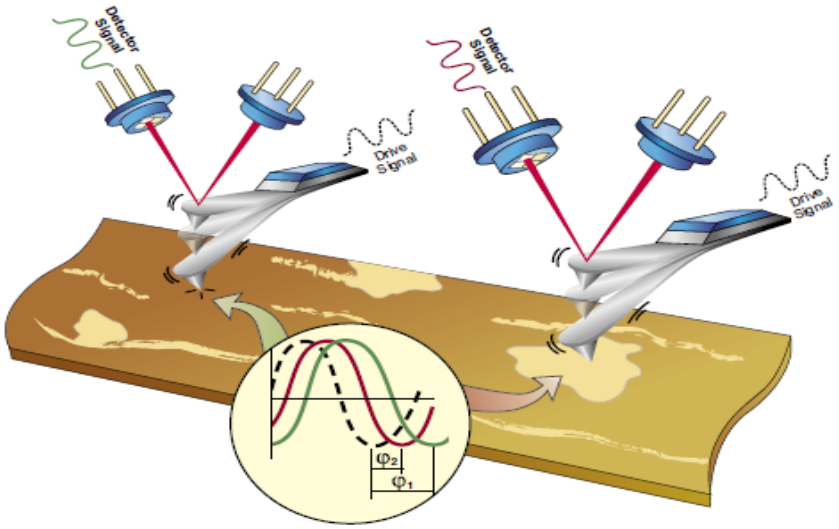

Fig. 3. 6 The phase shift of detector signal and drive signal in phase channel. The drive signal oscillates at constant frequency, and the phase shifts with $\boldsymbol{\varphi_1}$ and $\boldsymbol{\varphi_2}$ in different surface materials[86]. Image taken from Reference[86].

The tip oscillation is described as follow:

$$d = A\sin(2\pi f t + \varphi)$$

Where d is the deflection signal, where A is the amplitude, f is the frequency, t is the time, and φ is the phase shift[87].

3.2.3 Cantilever tuning

It is required for functional tapping mode AFM to tune the cantilever before starting measurements. The drive frequency typically set as 5% below[88] cantilever natural resonant frequency ($f_{drive} = 0.95 f_0$). When the drive frequency is close to resonant frequency, a small change of tip-sample separation can lead to large cantilever oscillation amplitude changes (good vertical sensitivity)[88]. Thus in tapping mode, the cantilever is driven at constant amplitude and frequency. When the cantilever comes close to surface, the tip-surface force gradient shifts the cantilever resonant frequency causing the oscillation amplitude to reduce[88], as shown in Fig. 3.7. An attractive force shifts the cantilever resonant frequency lower while repulsive force shifts the cantilever resonant frequency higher[88].

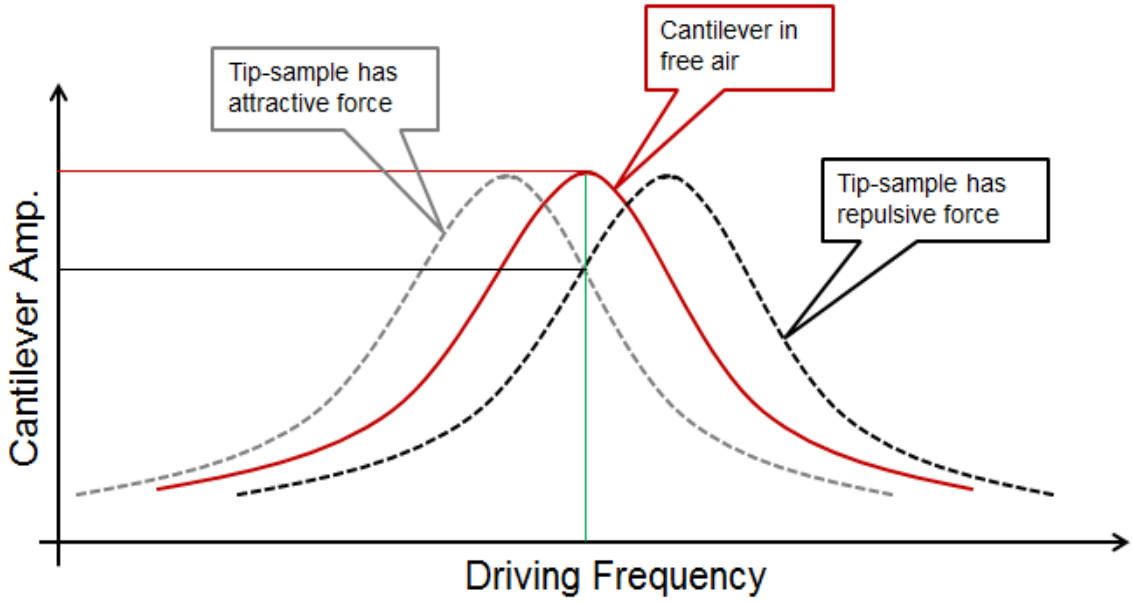

Fig. 3. 7 Cantilever amplitude oscillation vs. driving frequency. Cantilever resonant frequency shifts (grey dash line indicates cantilever resonant frequency lower shifts; black dash line indicates cantilever resonant frequency higher shifts). Image taken from Reference[88].

3.2.4 Conductive mode

Conductive mode AFM (C-AFM) uses an electrically conductive tip to measure surface topographic information and current distribution simultaneously. C-AFM operates in contact mode and simultaneously measures electrical properties[89] of the samples.

When a conductive tip is brought into contact with the sample surface, a bias voltage is applied between the conductive tip and surface[89]. Current flow can be measured and a current map is presented while the tip raster scanning across surface[89], shown in Fig. 3.8. Similar to STM, C-AFM provides current information. However, most importantly, it provides the topographic information and current flow independently, unlike STM, where the topographic and current images have cross-talk between one another[89]. This eliminates artefacts and convolution of two signals[89].

Typically, the conductive tip is coated with a thin layer of platinum-Iridium or gold. However, some cantilevers are made with purely conductive material or use a diamond[89] at the tip's apex. In each case, due to the small tip-surface contact area (~ 10 nm)[89], the current density may be very high. In order to preserve tip conductive layer, a resistor is used to control the current and reduce the risk of burning tip conductive layer.

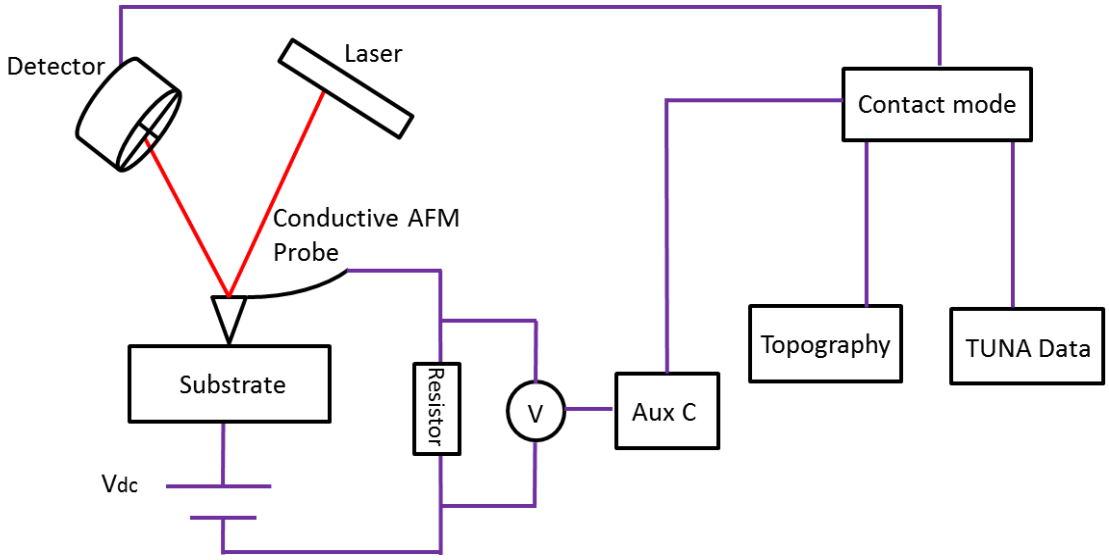

Fig. 3. 8 Schematic set-up of C-AFM. C-AFM operates in contact mode with a conductive AFM probe in circuits. Image taken from Reference[90].

3.2.5 Force Mode (Ramping)

AFM Force mode, which is also called ramping, refers to single point indentation of the tip into the surface. The cantilever approaches the sample surface then withdraws while monitoring the cantilever deflection vs. piezotube variation[91]. The information can be converted to force vs. surface distance curves which further provide mechanical properties of sample[91]. The parameters; spring constant and deflection sensitivity, are needed in these measurements[91].

Fig. 3.9 shows Z voltage vs. time curves for continual ramping. The X-Y voltage is kept constant and a triangular waveform is applied to Z electrodes. The ramping size and scan period keep constantly[92].

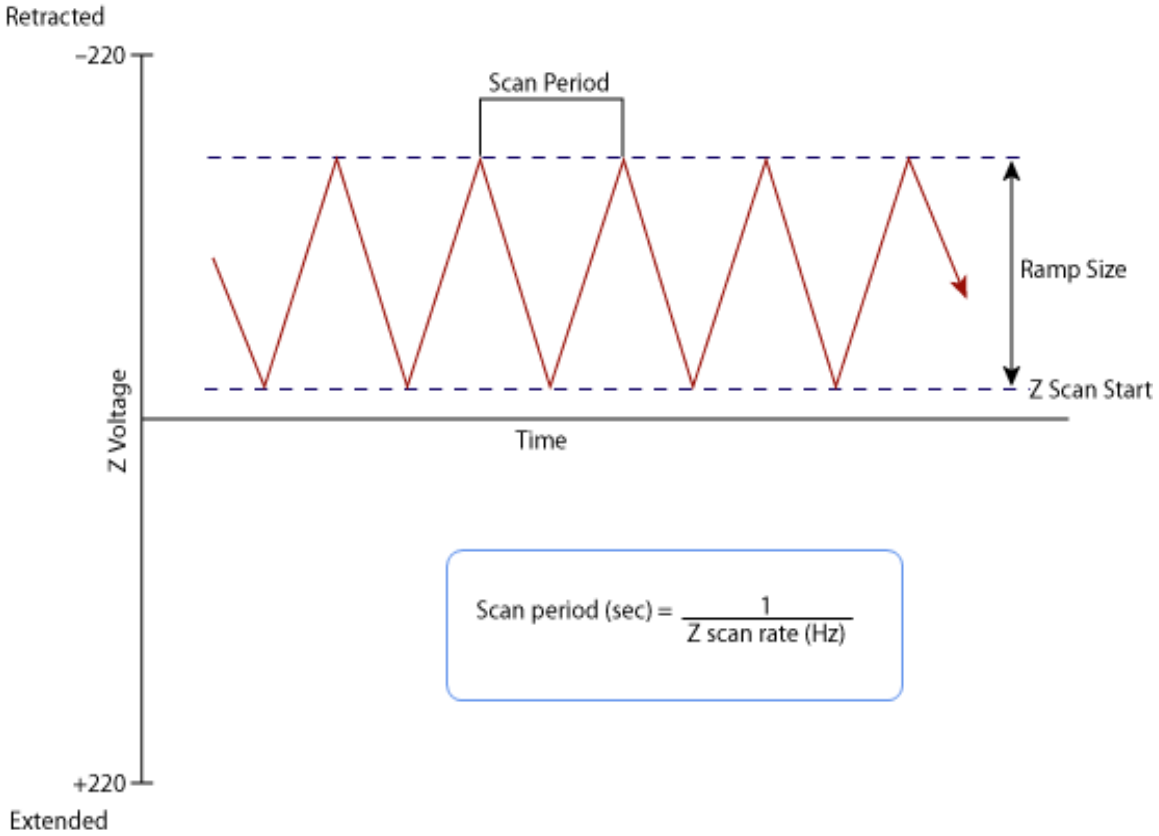

Fig. 3. 9 Continuous ramp waves and deflection variation of ramping. The ramp size and scan period is shown. Image taken from Reference[92].

In force mode AFM, the cantilever moves up and down from the sample surface and generates the deflection error (nm) with the change of z-position (Fig. 3.10). By ramping before proceeding to contact mode, the cantilever sensitivity is calibrated by analyzing the stiffness against the surface.

Fig. 3.10 demonstrates a tip-surface full ramping period. The blue line indicates the approaching movement from tip to surface, and the red line indicates the withdrawing movement. The tip moves to surface from far away distance (zero deflection), then captured by van der Waals or electrostatic force which causing negative deflection signal. Since the Z position then continuously moves down the cantilever bends to the other direction and giving positive deflection signal. Then the tip withdraws and deflection curve ends when long-range forces vanish[93]. The details of cantilever bending with the variation of force appearing in full cycle will be explained in Chapter 3.2.7.

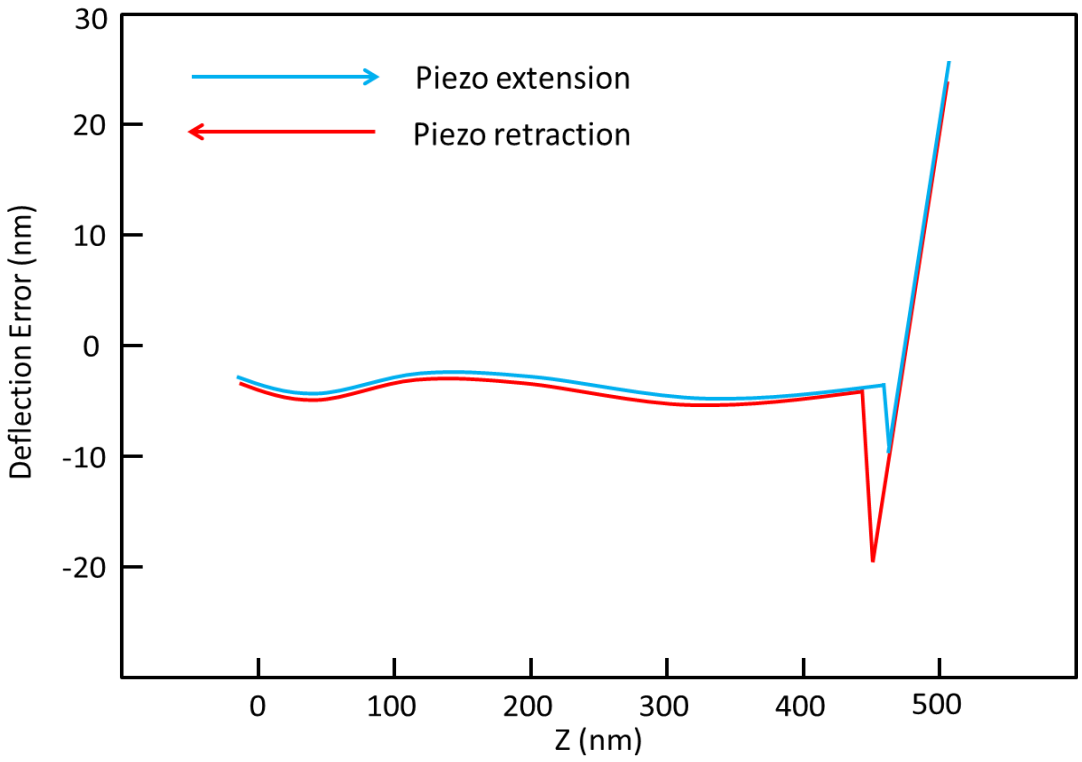

Fig. 3. 10 The deflection error (nm) vs. z-position curves. Image taken from Reference[94].

Ramping is a good technique which helps the investigation of force variation in a single indentation. It is an important element in the more advanced Peak Force QNM mode. Force modulation mode and Force volume mode are considered as evolved methods of Force mode.

Force modulation mode uses an oscillating cantilever at a constant frequency to indent the surface in a small region, by comparing the variation value of cantilever deflection to decide the stiffness of surface (smaller deflection in soft surface and larger deflection in hard surface)[95].

Force volume mode provides the topographic images and force ramping data simultaneously and output them in the same image[96]. Force Volume mode also records the height and tip retracts when the force reaches a trigger value for single indentation[96]. Then force mode starts to detect each (X, Y) position with force curves in selected range[96]. It provides a 3D indentation map, which further provides elastic and adhesion information[96].

3.2.6 Tip

Fig. 3.11 shows an advanced AFM tip (Fastscan-A) designed for imaging in air by Dimension FastScan AFM[97]. The cantilever is fabricated from Silicon Nitride by a photolithography technique. Table 1 shows the parameters of a Fastscan-A tip. The long triangular cantilever has a 1400kHz resonant frequency with 17N/m force constant[97]. The silicon tip radius is 5nm sharp, which keeps the images with high resolution even in hard surface while high-speed scanning[97].

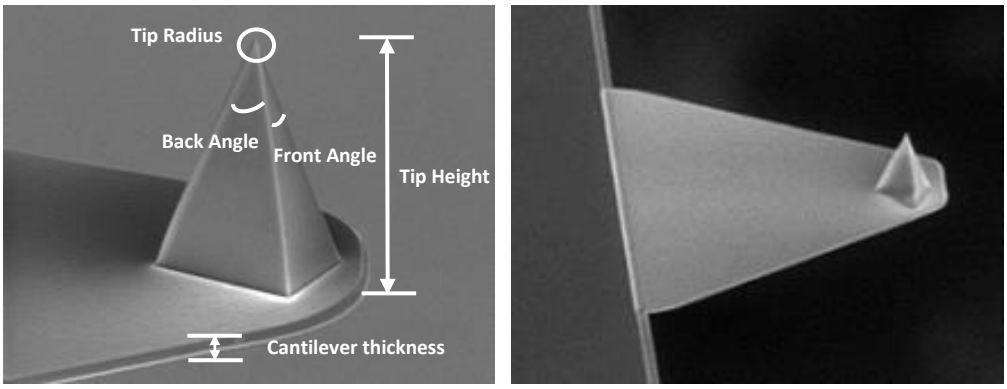

Fig. 3. 11 Fastscan-A tip SEM images. Image taken from Reference[97].

Table 1. Parameters of a Fastscan-A tip. Taken from Reference[97].

Tip Height (h)	2.5-8 μm
Tip Radius (Nom)	5nm
Front Angle (FA)	15±2.5°
Back Angle (BA)	25±2.5°
Cantilever thickness (Nom)	0.58 μm

3.2.6.1 Tip radius

For all AFM measurements, elastic and adhesion interactions in each indentation are strongly related with tip shape[98]. In contact mechanics models (Hertzian behaviour, 1885), the elastic half-space indentation by rigid object is first explained[98]. The function of indentation force in linear elastic surface is expressed as[98]:

$$F = \lambda \delta^{\beta}$$

Where F is the indentation force, δ is indentation depth. λ and β values refer the 'indenter shape' for sphere (Hertz), sharp cone and sharp pyramid tip[98]. Fig. 3.12 and Table 2 shows the spherical, conical, and pyramidal tip parameters.

Table 2. Force indentation parameters for different models. Taken from Reference[98].

Model	λ	β
Hertz: sphere of radius R	$\frac{4ER^{1/2}}{3(1-\nu^2)}$	$3/2$
Sharp cone of tip angle 2ϕ	$\frac{2E\tan\phi}{\pi(1-\nu^2)}$	2
Sharp pyramid of tip angle 2ϕ: Bilodeau solution	$\frac{1.4906E\tan\phi}{2(1-\nu^2)}$	2
Rico et al. solution	$\frac{E\tan\phi}{2^{1/2}(1-\nu^2)}$	2

(ν is Poisson's ratio and E is Young's modulus)

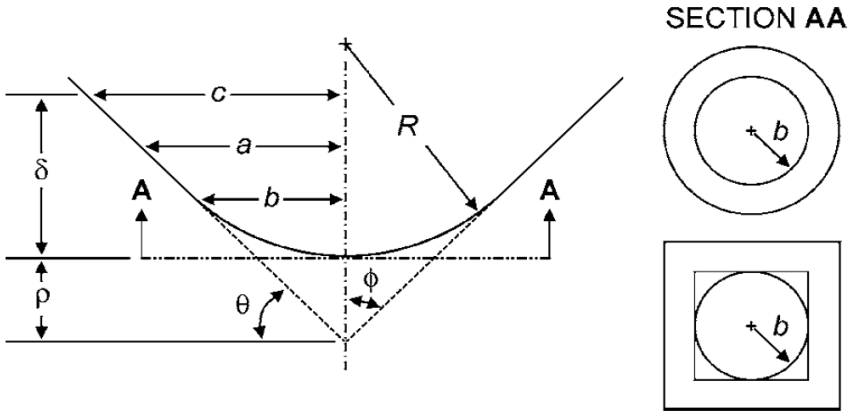

Fig. 3. 12 Blunt and sharp tip parameters. $\boldsymbol{a}$ is contact radius, **c** is indentation radius. $\boldsymbol{\theta}$ is incline angle of paramid tip. Image taken from Reference[98].

The equation for blunt tip is expressed as[98]:

$$F = \frac{2E}{1-\nu^2}\left\{a\delta - m\frac{a^2}{\tan\phi}\left[\frac{\pi}{2} - \arcsin\left(\frac{b}{a}\right)\right] - \frac{a^3}{3R} + (a^2-b^2)^{1/2}\left[m\frac{b}{\tan\phi} + \frac{a^2-b^2}{3R}\right]\right\}$$

Where 2ϕ is tip angle, b is the radius where the tip side becomes sphere with a tip radius R[98]. m is a constant value with cone $(=1/2)$, pyramid $\left(=2^{1/2}/\pi\right)$[98].

The contact radius with indentation depth equation is expressed as[98]:

$$\delta + \frac{a}{R}\left[(a^2-b^2)^{1/2} - a\right] - n\frac{a}{\tan\phi}\left[\frac{\pi}{2} - \arcsin\left(\frac{b}{a}\right)\right] = 0$$

Where $n = 1$ for cone and $n = 2^{3/2}/\pi$ for pyramid. If $\delta < b^2/R$, the Hertz model applied, if $R = b = 0$, the sharp tip model applied. $R \to \infty$ could be considered as truncated cone tip[98].

3.2.7 PeakForce Quantitative Mechanical Property Mapping (QNM)

Peak Force QNM is a new technique as a branch of tapping mode developed by Bruker, it captures the topography and force curves simultaneously. Similar to tapping mode, the tip and surface are in touch with each other intermittently for a short time region to avoid lateral forces[93]. The difference is that feedback loop controls a maximum vertical force on the tip (Peak force) rather than constant amplitude oscillation (normal tapping mode)[93,99].

Peak Force mode not only keeps tapping mode advantages to avoid lateral force and tip damage, but also provides other mechanical properties images by analyzing force curves in each pixel[93]. Peak Force QNM system has several astonishing benefits listed below, which also presents the theory of this technique.

1. High-resolution mapping of different mechanical properties.
2. Tip and surface protection while scanning with low lateral force.

3. Measurements of various materials with different types of tips.

Peak Force QNM provides channels of Height, Peak Force Error, DMT Modulus, Deformation Adhesion, Dissipation, Height Sensor, etc (Fig. 3.13 (c)). Following the manual, by analyzing the force curves (Fig.3.13) from each pixel, high resolution of mechanical properties mapping can be presented.

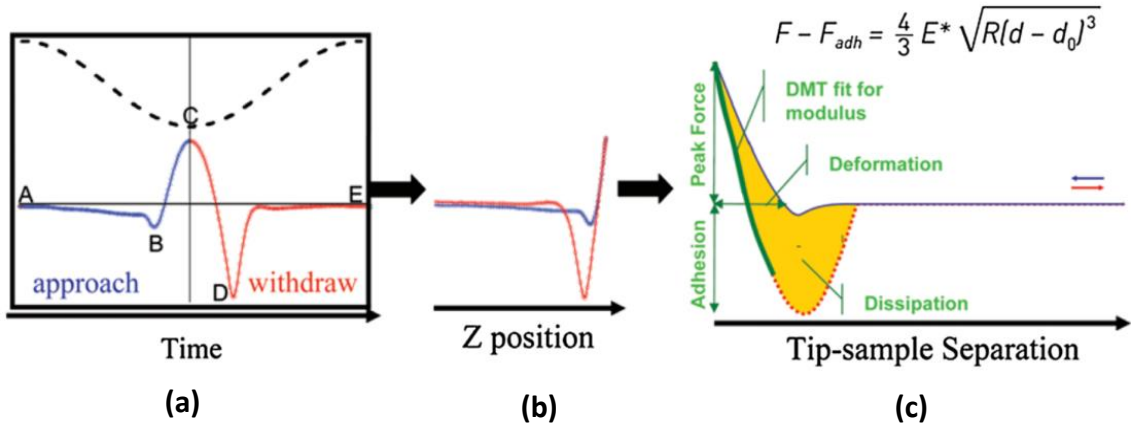

Fig. 3. 13 Peak Force QNM tip-surface indentation information. (a) tip-surface full indentation interaction. (b) force curves as a function of Z position. (c) mechanical properties from single force curve[99]. Image taken from Reference[93].

Fig. 3.13 (a) presents a tip-surface full indentation interaction. The top dashed line shows the Z-position modulation as a function of time for one period[93]. The X-axis is time and Y-axis is deflection signal. The blue line indicates the approaching period from tip to surface, while red line indicates the withdrawing period.

Following the same manual[93]: the modulation frequency is $2k$Hz and time from A to E is $0.5\,ms$. The tip indentation starts from point A, where the tip still is far from the surface (zero deflection). Then the piezo stretches, pulling Z position down, and the cantilever starts to bend over towards surface by van der Waals or electrostatic force, etc[93]. At point B, there is an attractive force on the tip as it is 'captured' by surface, this is associated with capillary forces due to surface moisture. As the Z position moves down to the end, the repulsive bending force of the cantilever overcomes the attractive force, and cantilever starts to bend in the opposite direction and reach point C, which refers the Peak Force indentation. The peak force at C during indentation is kept constant. The Z velocity is then reversed and moves upward until the adhesion force starts to overwhelm the cantilever stiffness again, until it reaches point D, the maximum adhesion point[93].

Then the tip is pulling off from surface, the curve reaches point E when the long-range forces vanish[93].

Following the same manual[93]: Fig. 3.13 (b) represents the force curves as a function of Z position to eliminate time variation, as a comparison with force-time curves. Fig 3.13 (c) demonstrates the mechanical properties values obtained from single force curve.

(1) Young's modulus

The green slope fitted line in Fig 3.13 (c) represents Young's modulus, which is extracted by applying the Derjaguin-Muller-Toporov (DMT) model[100].

$$F - F_{adh} = \frac{4}{3} E^* \sqrt{R(d - d_0)^3}$$

Where $F - F_{adh}$ represents the force on a cantilever, R is the tip radius, $d - d_0$ is sample deformation. E^* represents the reduced modulus. The Young's modulus E_s can be obtained from the equation below if tip Poisson's ratio is known. Assume tip modulus E_{tip} is infinite[93].

$$E^* = \left[\frac{1 - v_s^2}{E_s} + \frac{1 - v_{tip}^2}{E_{tip}} \right]^{-1}$$

(2) Adhesion

The source of adhesion force acquired from measurements in Fig 3.13 (c) could be any kind of attractive force. The electrostatic force and van der Waals force all contribute to relative strength depending on different parameters (i.e. surface charge and hydrophilicity). The adhesion value increases with the increasing of tip area. Also, the energy dissipation is dominated by adhesion work if there is certain value of peak force, and the non-elastic deformation area is negligible. If the tip is functionalized, the adhesion force can reflect chemical interaction between tip and sample[93,101].

(3) Deformation

Deformation is defined as the indentation distance of tip into surface at peak force value. Deformation increases with the force loading value until peak force set point. It includes

both elastic and plastic contributions. The deformation can be calculated from the distance where force is zero till peak force point[93].

(4) Dissipation

Dissipation is defined as the integration of force times velocity integrated over one period, shown in gold area in Fig. 3.13 (c) and can be expressed as:

$$W = \int \vec{F} \cdot d\vec{Z} = \int_0^T \vec{F} \cdot \vec{v}\, dt$$

Where W is the energy dissipation in single indentation cycle, presents in the unit of electron volts and refers the mechanical energy lost per cycle. F represents the indentation force vector and dZ represents the displacement vector. In pure elastic deformation, the dissipation is low due to small hysteresis between repulsive parts in loading-unloading curve, and it is dominated by adhesion work[93].

The tip used for Peak Force QNM measurements is ScanAsyst-Fluid +, shown in Fig. 3.14. It has a sharp tip ($2nm$ tip radius) and a low spring constant cantilever ($0.7N/m$) which is ideal for high-resolution measurements[102].

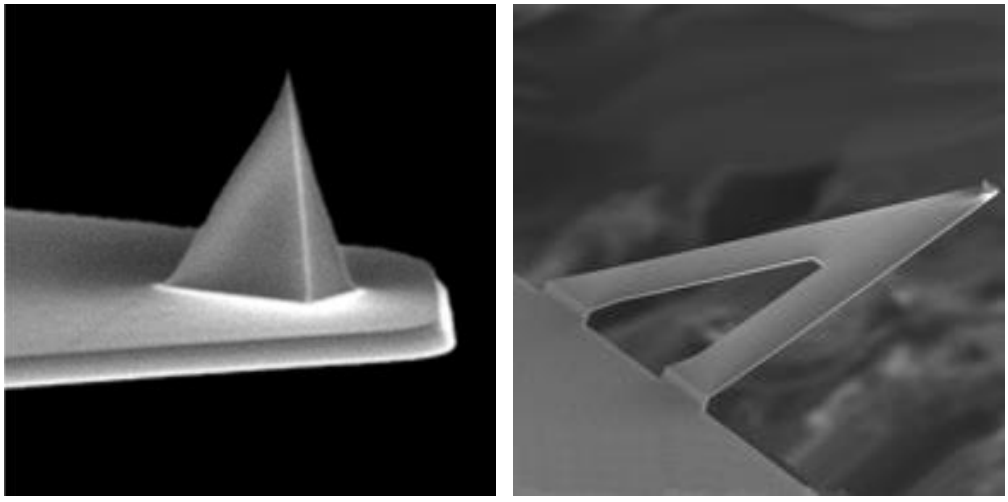

Fig. 3. 14 ScanAsyst-Fluid+ tip SEM images. Image taken from Reference[102].

3.3 Electrostatic Force Microscopy (EFM) and Kelvin Probe Force Microscopy (KPFM)

In AFM measurements, the tip-surface interaction typically contains various forces. When the tip is approaching the surface, short-range repulsive force, van der Waals force, chemical binding force, long-range electrostatic force, etc. all affect the interaction[103]. An expression for the electrostatic force, which is the relevant force for EFM and KPFM, can be obtained by considering the tip-sample system as a capacitor[103]. The force can be deduced from the energy of a capacitor, $U_{el} = 1/2CV^2$, which leads to[103]:

$$F_{el} = -\nabla U_{el} = \frac{1}{2}\frac{\partial C}{\partial r}V^2 + CV\frac{\partial V}{\partial r}$$

where C is the capacitance and V is the total voltage[103]. To simplify the system, only a metallic tip and sample is considered. Thus $\frac{\partial V}{\partial r} = 0$. Since the main interaction in an AFM measurement comes from the forces perpendicular to the sample (in the z direction), the equation above could be simplified to[103]:

$$F_{el} = \frac{1}{2}\frac{\partial C}{\partial z}V^2$$

In EFM and KPFM measurements, an electrostatic force field is generated by applying an ac-voltage $V_{ac}\sin(\omega_{ac}t)$ at frequency ω_{ac}, which will generate a cantilever oscillating at this frequency ω_{ac}[103]. Since the tip-sample system can be considered as a capacitor, F_{el} can be expressed as[103]:

$$F_{el} = \frac{1}{2}\frac{\partial C}{\partial z}[V_{dc} - V_{CPD} + V_{ac}\sin(\omega_{ac}t)]^2$$

$$F_{el} = \frac{1}{2}\frac{\partial C}{\partial z}[V_{dc} - V_{CPD} + V_{ac}\sin(\omega_{ac}t)]^2 = \frac{1}{2}\frac{\partial C}{\partial z}\left[(V_{dc} - V_{CPD})^2 + 2(V_{dc} - V_{CPD})V_{ac}\sin(\omega_{ac}t) + {V_{ac}}^2\sin(\omega_{ac}t)^2\right] = \frac{1}{2}\frac{\partial C}{\partial z}\left[(V_{dc} - V_{CPD})^2 + 2(V_{dc} - V_{CPD})V_{ac}\sin(\omega_{ac}t) + {V_{ac}}^2(1 - \cos(2\omega_{ac}t))/2\right] = \frac{\partial C}{\partial z}\left[\frac{(V_{dc}-V_{CPD})^2}{2} + \frac{{V_{ac}}^2}{4}\right] + \frac{\partial C}{\partial z}(V_{dc} - V_{CPD})V_{ac}\sin(\omega_{ac}t) - \frac{\partial C}{\partial z}\cos(2\omega_{ac}t))/4$$

Where $\partial C/\partial z$ is the capacitance gradient of the tip-sample system and CPD stands for the Contact Potential Difference or surface potential[103]. F_{dc} is an additional static force contributing to the topography output signal, $F_{\omega_{ac}}$ is the force at the ac-frequency used to measure CPD in KPFM[103] and $F_{2\omega_{ac}}$ is the force at two times the ac-frequency, which can be used to obtain capacitance information[104].

$$F_{dc} = \frac{\partial C}{\partial z}\left[\frac{1}{2}(V_{dc} - V_{CPD})^2 + \frac{V_{ac}^2}{4}\right]$$

$$F_{\omega_{ac}} = \frac{\partial C}{\partial z}(V_{dc} - V_{CPD})V_{ac}\sin(\omega_{ac}t)$$

$$F_{2\omega_{ac}} = -\frac{\partial C}{\partial z}\frac{V_{ac}^2}{4}\cos(2\omega_{ac}t)$$

The most common implementation of EFM is carried out in a two-pass scheme: in the first pass it tracks the topography, which can also contain the influence of the electrostatic force, and then in the second pass it lifts the cantilever up to more than $10nm$, to avoid the topographic interaction, while a bias voltage is applied[103]. In this way the electrostatic force is measured avoiding the topographic influence[103]. Nevertheless, the EFM output signal could be influenced by the capacitance gradient and the CPD[103].

KPFM is built by combining non-contact AFM and EFM with the Kelvin probe technique (invented in 1898 by Lord Kelvin for macroscopic surface potential research)[105]. KPFM uses the same approach by adding a dc-voltage (V_{dc}) that equals the CPD, thus nullifying the electrostatic force component at frequency ω_{ac}[106].

The CPD is the tip-surface work function Φ difference and can be expressed as [103]:

$$V_{CPD} = \Delta\Phi/e = (\Phi_{surface} - \Phi_{tip})/e$$

Where e is elementary charge[103]. Using a calibrated tip of known work function (Φ_{tip}), the surface's work function ($\Phi_{surface}$) can be calculated from the measured CPD.

In KPFM, typically two modes are used: amplitude modulation (AM-mode) and frequency modulation (FM-mode) [103]. AM-mode directly detects the electrostatic force through the cantilever oscillation at the ac-frequency and uses a dc-voltage to minimize

the amplitude of the cantilever oscillation at this ac-frequency[103]. In the FM-mode, the ac-bias voltage induces an oscillation of the frequency shift Δf_0 at the ac-frequency, resulting in a detection of the electrostatic force gradient[103]. Then, this frequency shift is minimized with a dc-voltage. A schematic setup of KPFM is shown in Fig. 3.15.

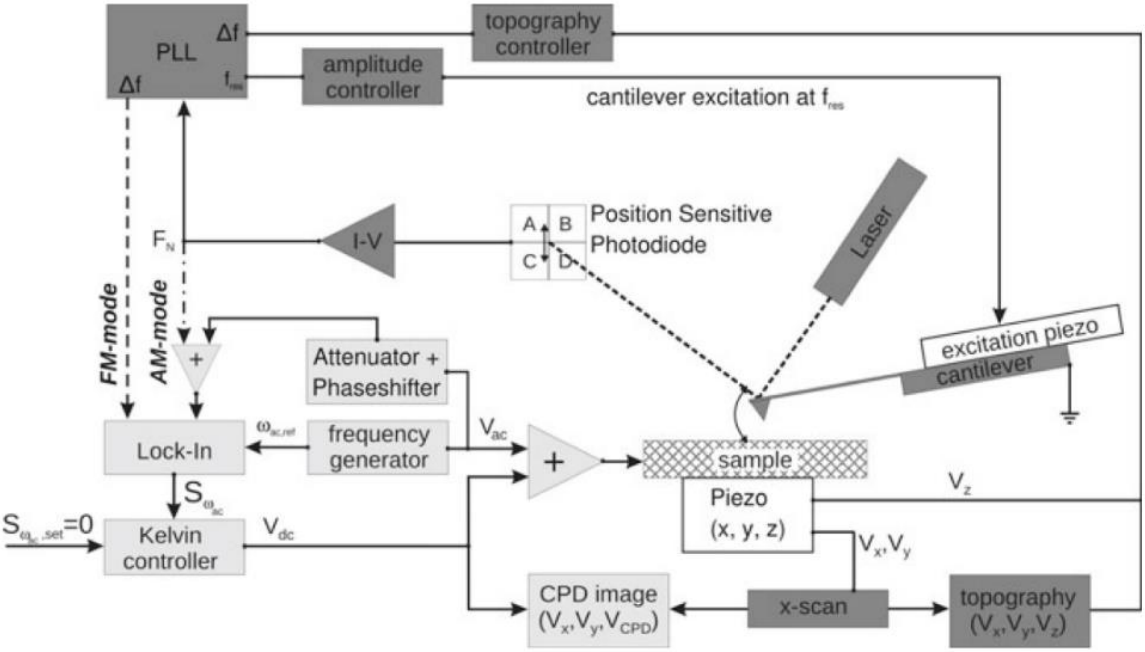

Fig. 3. 15 The schematic diagram of KPFM route. Image taken from Reference[103].

The dashed line in Fig. 3.15 refers to FM-mode, while the dashed-dotted line refers to AM-mode. Dark grey boxes correspond to the regular non-contact AFM topography part of the setup and the light grey boxes are the KPFM part[103]. The cantilever oscillation is detected by a photodiode, then the signal is delivered to a frequency detector which can be a phase-locked loop (PLL) or a frequency demodulator[103]. The PLL keeps the cantilever oscillation in its fundamental resonance frequency f_{res}[103]. For the electrostatic measurements, a frequency generator provides the ac voltage (V_{ac}) applied to the sample and generates a reference frequency for the Lock-in amplifier[103]. For the FM-mode, the Δf_0 from the PLL is delivered to the Lock-in amplifier directly[103]. The Lock-in amplifier then measures the magnitude of the frequency shift[103]. For the AM- mode, the output photodiode signal with the amplitude of the cantilever oscillation is driven to the Lock-in amplifier directly[103]. In order to distinguish the fundamental resonance frequency and the ac-frequency from the photodiode, high/low-pass filters can be applied[103]. The Lock-

in amplifier output ($S_{\omega_{ac}}$) is the input for the Kelvin controller[103]. The Kelvin controller provides an output dc-voltage (V_{dc}) that matches the contact potential difference V_{CPD} nullifying the input signal $S_{\omega_{ac}}$. V_{dc} is then added to the ac signal so to the total voltage applied to the sample is $V_{ac} + V_{dc}$[103]. The CPD images are obtained by recording the applied V_{dc} with the XY scan of sample[103].

3.4 Raman Spectroscopy and Photoluminescence (PL) Spectroscopy

Raman spectroscopy is a technique, based on the research from C.V. Raman in 1928, which identified Raman scattering. Raman scattering is inelastic scattering of photon from phonons, which results in a discrete energy shift[107]. This technique is used to obtain the structure of molecules and crystals[107].

Molecular energy includes contributions from translational energy, rotational energy, and vibrational energy[108]. The electromagnetic radiation is expressed by wavelength (λ) and frequency (ν) with following functions[108]:

$$\lambda = \frac{c}{\nu}$$

$$\nu = \frac{\Delta E}{h}$$

$$\omega = \frac{\nu}{c} = \frac{1}{\lambda}$$

Where c is light velocity, h is Planck's constant, ΔE is photon energy and ϖ is wave number. In Raman Spectroscopy, the scattered radiation on vibrational and rotational states of molecules are measured[108]. Raman spectroscopy uses single frequency radiation to irradiate the sample, and measure the energy shift of the resultant light[109]. Since the molecular vibrational and rotational states are quantised, the shift falls at well-defined peaks.

It is a useful tool for structural characterisation, strain or defects detection and functionalisation of graphite and graphene, especially in the determination of the number of layers and stacking order in graphene[110]. Two of the outstanding features that appear in monolayer graphene's Raman spectrum are named the G band (1582 cm^{-1}) and G' band (2700 cm^{-1}) (Fig. 3.16)[110].

The monolayer G' band at room temperature exhibit full width at half maximum (FWHM) of $\sim 24\ cm^{-1}$ [110]. Also, the intensity of G' band is very large comparing to G band[110].

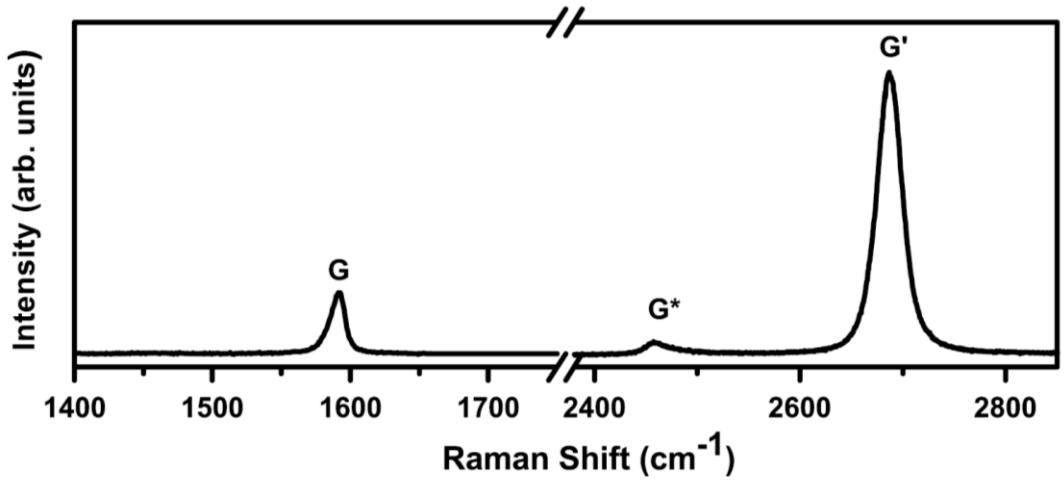

Fig. 3. 16 The peak intensity vs. Raman shift map of monolayer graphene. Image taken from Reference[110].

Photoluminescence (PL) is a radiative process and is caused by photon absorption (photoexcitation)[111], it is used in material science and solid-state physics, for example in the investigation of mid-gap states, impurities, defects in the sample etc[111]. It can analyze and characterize lasing materials by the stimulated photon emission process[111]. PL has two types: fluorescence and phosphorescence. The fluorescent material absorbs photon by light excitation, transfers its energy to a ground state electron and promotes it to an excited state[111]. The electrons in higher excited states rapidly relax to lowest excited states by exciting molecular vibrations[111]. Then electrons recombine to the ground state by emitting photons. The resultant emission has an energy associated with the materials excitation spectrum and not the incident light[111]. The difference of fluorescence with phosphorescence is that electrons in a singlet excited state relax into a triplet excited state, in which electron spin is not paired with ground state[111]. Therefore, the decay process is considered quantum mechanically '*forbidden*' and, as such has a lifetime much longer than a '*permitted*' transition. Emission between triplet excited state and singlet state (or any two energy levels with a forbidden transition) is called phosphorescence[111]. Emission between singlet excited state and singlet ground state (or any two energy levels with same spin states) called fluorescence[111]. In fluorescence, the

average lifetime of an electron in an excited state is $10^{-5}\sim10^{-8}s$ and decay happens once the excitation source is removed. In phosphorescence, the average lifetime of electron in excited state is $10^{-4}\sim10^{4}s$, which means phosphorescence continues for longer period after excitation source is removed[111].

In fact, when a sample is illuminated by a laser, both Raman scattering and PL happen, but the PL relative intensity is much higher. Thus, the advanced Raman spectroscopy contains Raman and PL on a single microscope and provide both vibrational and electronic properties of samples[112].

Research found two methods can induce bandgap in graphene: nanoribbons (quantum dots/channels) and chemical treatment, thus the luminescence is detected in graphene[113]. In some previous work, individual graphene flakes have bright luminescent properties after the treatment by oxygen plasma, shown in Fig. 3.17[113]. The photoluminescence map and the elastic scattering image are compared[113].

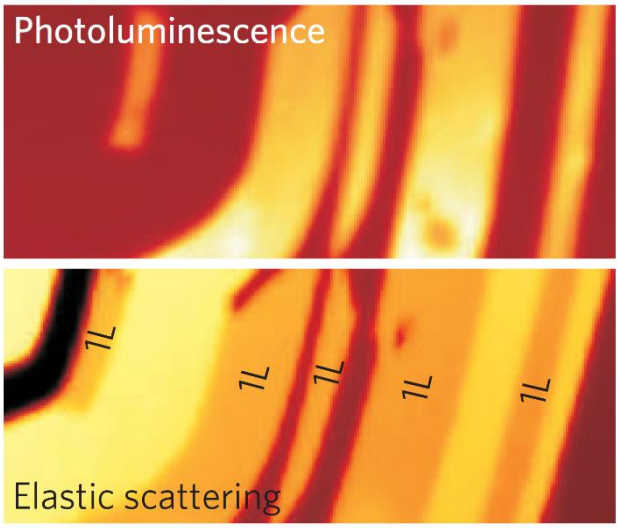

Fig. 3. 17 The photoluminescence map and the elastic scattering image of graphene treated with oxygen plasma**.** Image taken from Reference[113].

3.5 Electron Beam Lithography (EBL)

Electron beam lithography (EBL) is a technique derived from scanning electron microscopy (SEM); the technique uses a focused electron beam to create fine patterns on a surface with resist films[114]. The resist films are sensitive to electrons and the acquired patterned film is obtained by exposure[115]. The patterned films act as a mask for subsequent processes, such as etching and gold vapour deposition etc[115]. The ultimate electron spatial resolution is in the range of 0.06~0.15nm[115]. In short, the EBL system is combined with a few subsystems, including electron optical column, analogue and digital electronics, XY position stage, vacuum systems, fast computer processors and extensive software, as shown in Fig. 3.18[115]. EBL has advantages such as: 1) a high-resolution atomic level; 2) suitability for a variety of materials: and 3) the ability to expose a number of fine patterns with a variety of materials[116].

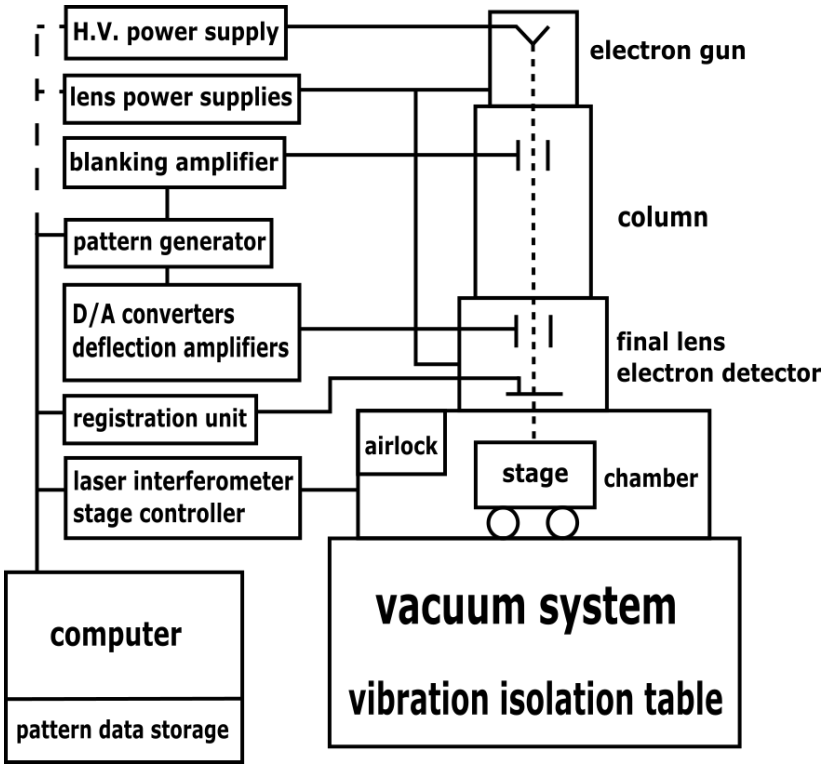

Fig. 3. 18 The schematic setup of major subsystems in traditional EBL, including vacuum system, column and electron gun. Image taken from Reference[116].

The first EBL machine was developed in the 1960s and, soon after, polymethylmethacrylate (PMMA) was used as a resist for this technique[117]. PMMA acts as a good resist because it has: 1) high contrast and good resolution; 2) a continuous and

homogeneous film on the surface; 3) high-etch resistance; and 4) good thickness and high stability[118].

The pattern data are designed then converted to a format that is suitable for EBL writing[115]. The digital data paths are automatically converted and sent to the electron beam system.[115] The electron beam then scans the writing field using electric or magnetic fields and breaks the molecular chain of the PMMA resist[115]. By dipping the already exposed surface into the developer, the final shape pattern area is obtained[115]. Fig. 3.19 schematically demonstrates the process described above.

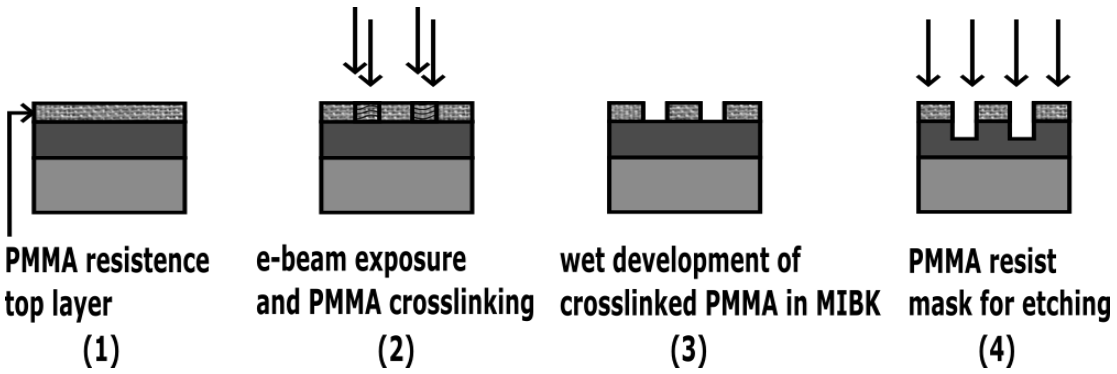

Fig. 3. 19 Positive-tone resist process. (1) PMMA resistance top layer covered (2) electron beam scan on resist layer (3) wet development process (4) PMMA resist mask protection for etching. Image taken from Reference[115].

Chapter 4

Fabrication process

4.1 Introduction

In this chapter, the mechanical exfoliation process and flake selection through different filters are presented. The transfer machine and technique: polymethylmethacrylate (PMMA)/polymethylglutarimide (PMGI) method and polydimethylsiloxane (PDMS) method are discussed. The method of fabricating aligned heterostructures, lithography and contact evaporation process are introduced.

4.2 Micromechanical exfoliation and flake selection

In this work, graphene and other monolayer /thin layer 2D materials (hBN, TMDCs) are produced by the micromechanical cleavage method. The process of exfoliating graphene is as followed and shown in Fig. 4.1:

(1) Peel bulk graphite using scotch tape several times until the graphite flakes are spread across the surface of the tape.

(2) Place flakes on top of a pre-heated SiO_2 290nm wafer (hot plate 135°C).

(3) Cool down to room temperature for 10mins.

(4) Carefully peel the scotch tape off one corner of SiO_2 290nm wafer.

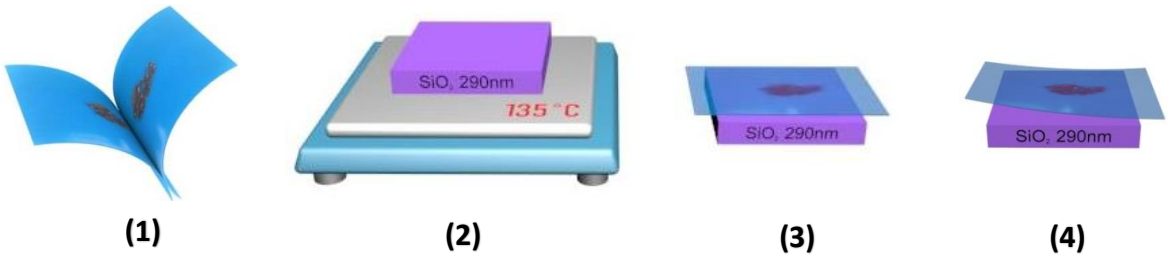

Fig. 4. 1 Micromechanical cleavage method. (1) Peel bulk graphite with scotch tape. (2) Heat SiO_2 wafer to **135**°C and put flakes on SiO_2 290nm wafer (3) Cool down for 10 min. (4) Peel off scotch tape from substrate.

Different scotch tape types (BT-130E-SL, BT-150E-KL, BT-50E-FR, 1009R-6.0) are used in this work. The micromechanical cleavage method provides high quality flakes with multiple layers and less contamination. The thickness of SiO_2 is quite important, for thin layer graphene flakes, to allow them to be visible under an optical microscope. SiO_2 with 70nm, 90nm, 290nm thickness are used as a substrate[16]. By adjusting the exposure time and gain in both bright field and dark field of the optical microscope, monolayer and thin layer flakes can be distinguished by the variation in the flake colour (bright field) and the variation of the thickness of flake edge (dark field), as shown in Fig. 4.2 below.

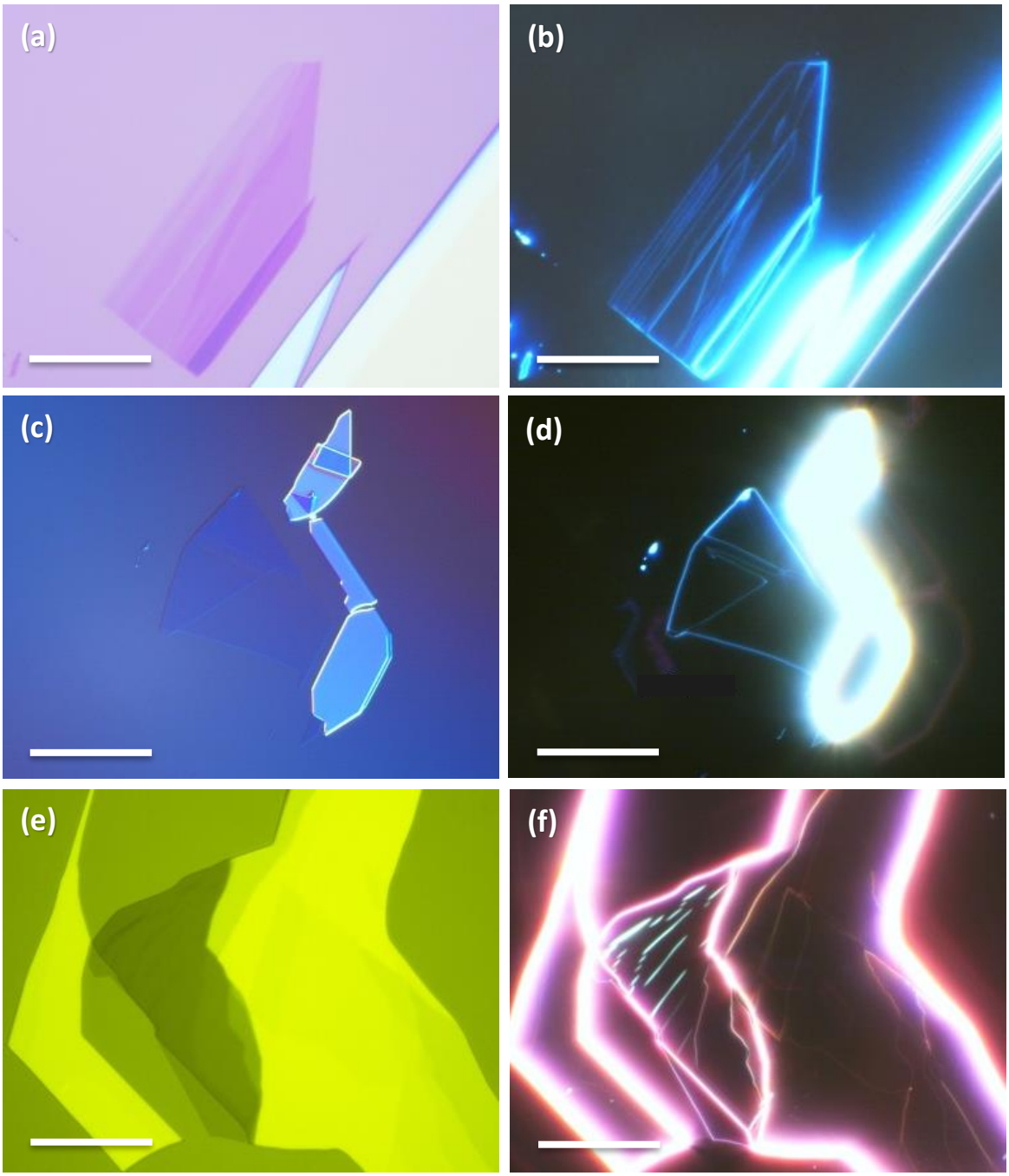

Fig. 4. 2 Graphene, hBN and TMDCs under microscope. Monolayer and thin layer graphene from one flake on SiO_2 290nm substrate under 100x microscope exposure (a) bright field (b) dark field. hBN flakes with different layers on SiO_2 290nm substrate under 100x microscope magnification (c) DIC filter (d) dark field. $MoSe_2$ flakes with different layers on PMMA/PMGI/Test Si substrate under 100x microscope magnification (e) Colour filter (f) dark field.

4.3 Transfer technique

Transfer technique is used to produce heterostructures by ‘pick-up’ and ‘put-down’ procedures, in this work. In this paragraph, the most commonly produced sandwich-like heterostructure (hBN/graphene/hBN) is presented as an example (Fig. 4.3).

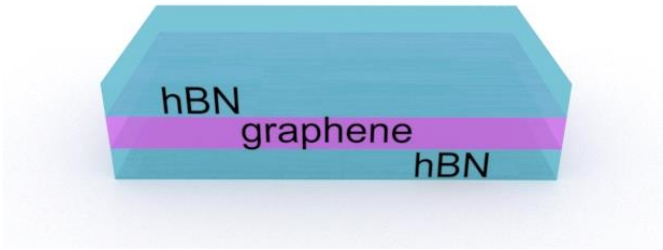

Fig. 4. 3 hBN/graphene/hBN heterostructure.

The transfer machine used in this work consists of 3 main parts: temperature control panel, optical microscope, transfer stage (including mechanical transfer arms and vacuum pumping machine), shown in Fig. 4.4.

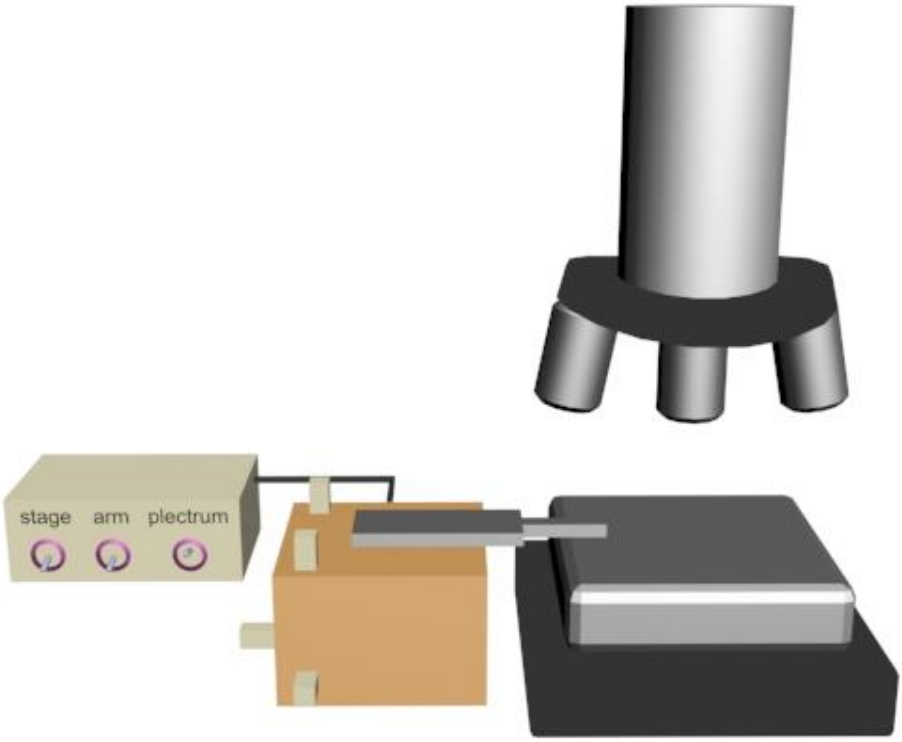

Fig. 4. 4 Transfer machine set-up. Including optical microscope, transfer stage and temperature control panel.

The temperature control panel is capable of heating to a maximum of 150℃. Normally 60~80 °C is used for transfer. By switching on the plectrum, arm and stage vacuums, the position of flakes are fixed, to achieve a successful ‘pick-up’ or ‘put down’.

There are two transfer methods used in this work: (1) PMMA/PMGI and (2) PDMS (which is further explained in Chapter 4.31 and 4.32). By using the top layer flake (hBN) to pick up the graphene and put it down on the substrate hBN, the heterostructure (hBN/graphene/hBN) is produced.

4.3.1 Polymethylmethacrylate (PMMA)/ Polymethylglutarimide (PMGI) method

PMGI and PMMA (950 A8) (950K molecular weight, 8% in anisole) are used in this method. We spin the PMGI on top of the Test-Si wafer, at a spin speed of 3000/rpm (full wafer). After baking for 5 mins on a hot plate at 135°C, we spin the PMMA (950 A8) on top of the Test-Si wafer with the PMGI covered. By exfoliating flakes using Scotch tape on a pre-spin PMMA/PMGI wafer, different thicknesses of flakes are selected with the help of a filter on the optical microscope. We use sharp tweezers to scratch a circle under a 5x optical microscope; then, we carefully add droplets of MF-319 solvent to dissolve the bottom layer of the PMGI, and then we float PMMA membrane with flakes on top of the DI water, then use a plectrum to scoop out the PMMA membrane and dry it in air for 10 mins at room temperature (process shown in Fig. 4.5).

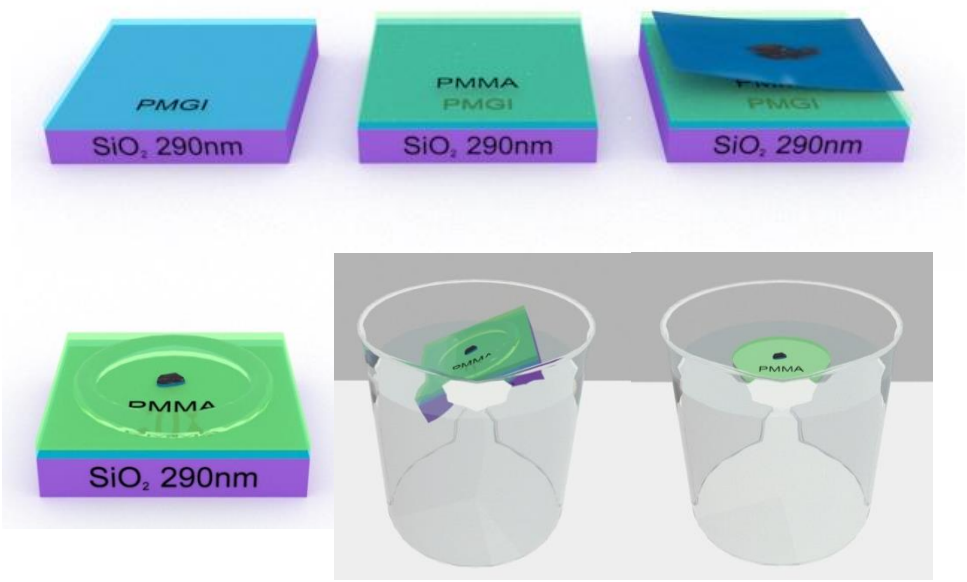

Fig. 4. 5 PMMA/PMGI method of exfoliating graphene and transfer preparation. MF-319 solvent dissolves PMGI layer and PMMA membrane floating on DI water.

Use transfer machine to pick up or put down flakes. After baking on hot plate for 10 mins, 135°C. PMMA is washed-off by acetone and IPA.

4.3.2 Polydimethylsiloxane (PDMS) method

PDMS is a new method that has the advantage of speed controlling when picking up/putting down flakes. By controlling the transfer speed and temperature, this method minimises the bubbles between the flakes, which further increases the quality of the samples. We mix the PMDS and a silicone elastomer base (1:10) uniformly in glassware, and vacuum the mixture for 30 mins and until all the bubbles have vanished. We bake for 30 mins at 130°C until the crosslink is finished. We spin the PPC (5%/15%) or PMMA (8%) on top of the PDMS polymer and cut it into small pieces. When the pick-up temperature is 50°C and the put-down temperature is 150°C, the bubbles between the flakes are squeezed out at a low speed and high temperature (process shown Fig. 4.6).

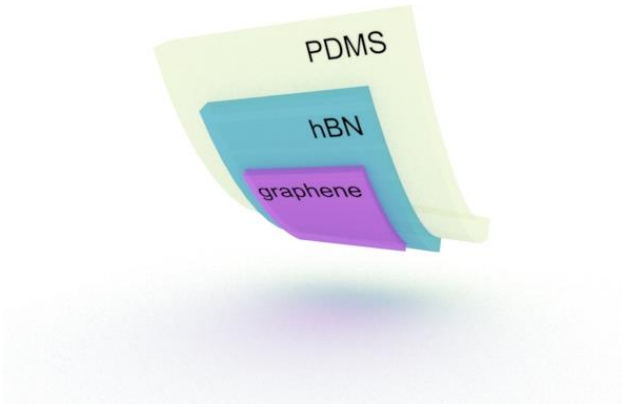

Fig. 4. 6 PDMS method for hBN picking up graphene.

4.4 Fabrication of single aligned graphene /hBN heterostructures

In this paragraph, hBN and graphene flakes are used as an example to present the fabrication process for aligned heterostructures. As shown in Fig. 4.7, the edges with angles on both flakes are measured at approximately 120° and 150° (highlighted in Fig.4.7). These are chosen as the alignment edges. When graphene is transferred on top of the hBN, the two alignment edges are adjusted parallel to each other (a small angle difference will appear when two flakes make contact with each other); alignment will occur if both selected edges are armchair or zigzag.

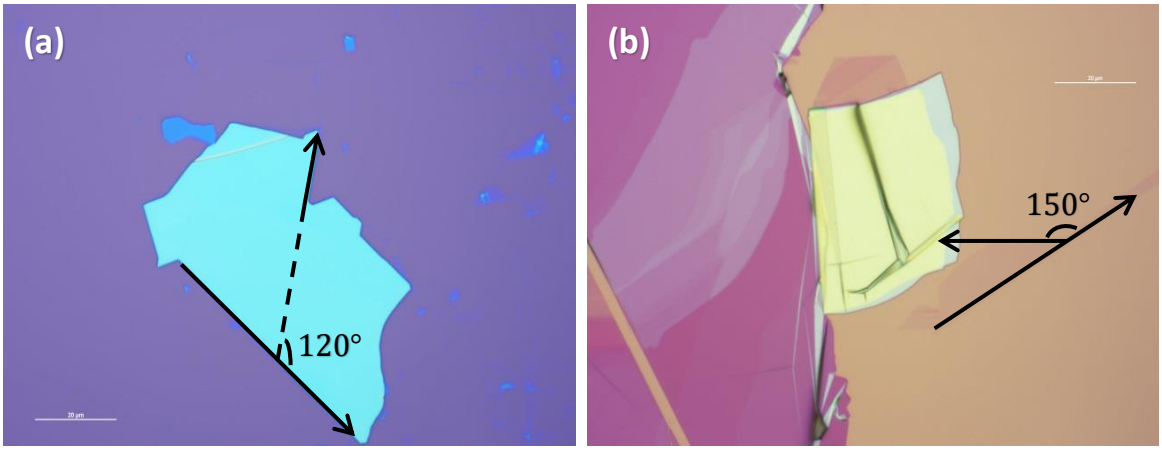

Fig. 4. 7 Alignment edges selection. Optical images of (a) hBN flake with edge angle of 120 ° and (b) graphene flake with edge angle of 150°.

4.5 Fabrication of double aligned hBN/graphene/hBN heterostructures

The top hBN flake is exfoliated on a pre-spin PMGI/PMMA Test Si wafer. We use the selected hBN flake from the PMMA membrane to pick up graphene from SiO_2 290nm, then transfer onto the pre-selected bottom hBN (on SiO_2 290nm). In this process, three red lines represent selected alignable edges; the middle layer of graphene is aligned with both the top hBN and the bottom hBN. The hBN/graphene/hBN double-aligned stack is shown in Fig. 4.8.

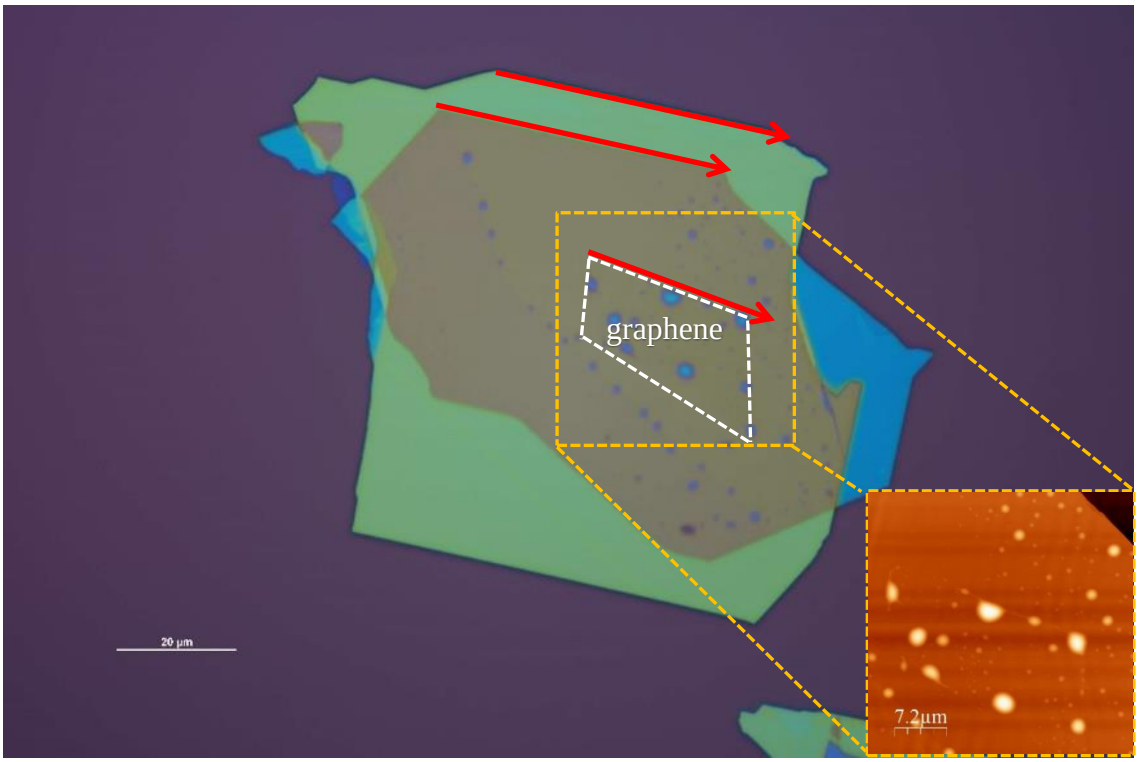

Fig. 4. 8 Optical images of double aligned hBN/graphene/hBN heterostructure.

4.6 EBL exposure, etching, contact evaporation and lift off

1) EBL exposure

PMMA (495K A3) and PMMA (950K A3) are prepared for EBL exposure. We spin one layer of PMMA (495K A3) and bake for 5 mins at $150^{\circ}C$. We spin another layer of PMMA (950K A3) and bake for 5 mins. Using a lower molecular weight of PMMA can help to lift off easier. Solvent MIBK：IPA（1：3）and IPA are used for pattern developing. We immerse the wafer in MIBK：IPA（1：3）for 30s, then in IPA for another 30s.

2) Etching and contact evaporation

After the designed nanoscale pattern is exposed on the PMMA layers, etching is performed to remove part of the flake and leave the flake with the designed pattern. Gold is evaporated on top of the surface to produce electric contacts (1D contact) for the flakes.

3) Lift off

We immerse the samples in a beaker of hot acetone ($60^{\circ}C$) and cover with a beaker cap for 15 mins. We flush the sample surfaces with acetone at room temperature. We keep the sample surfaces wet with acetone until the gold is fully lifted off, and wash off the acetone residue with IPA.

Finally, we use EBL to expose the hall bar shape using this method and etch the shape of the hall bar.

The process is showing as follows:

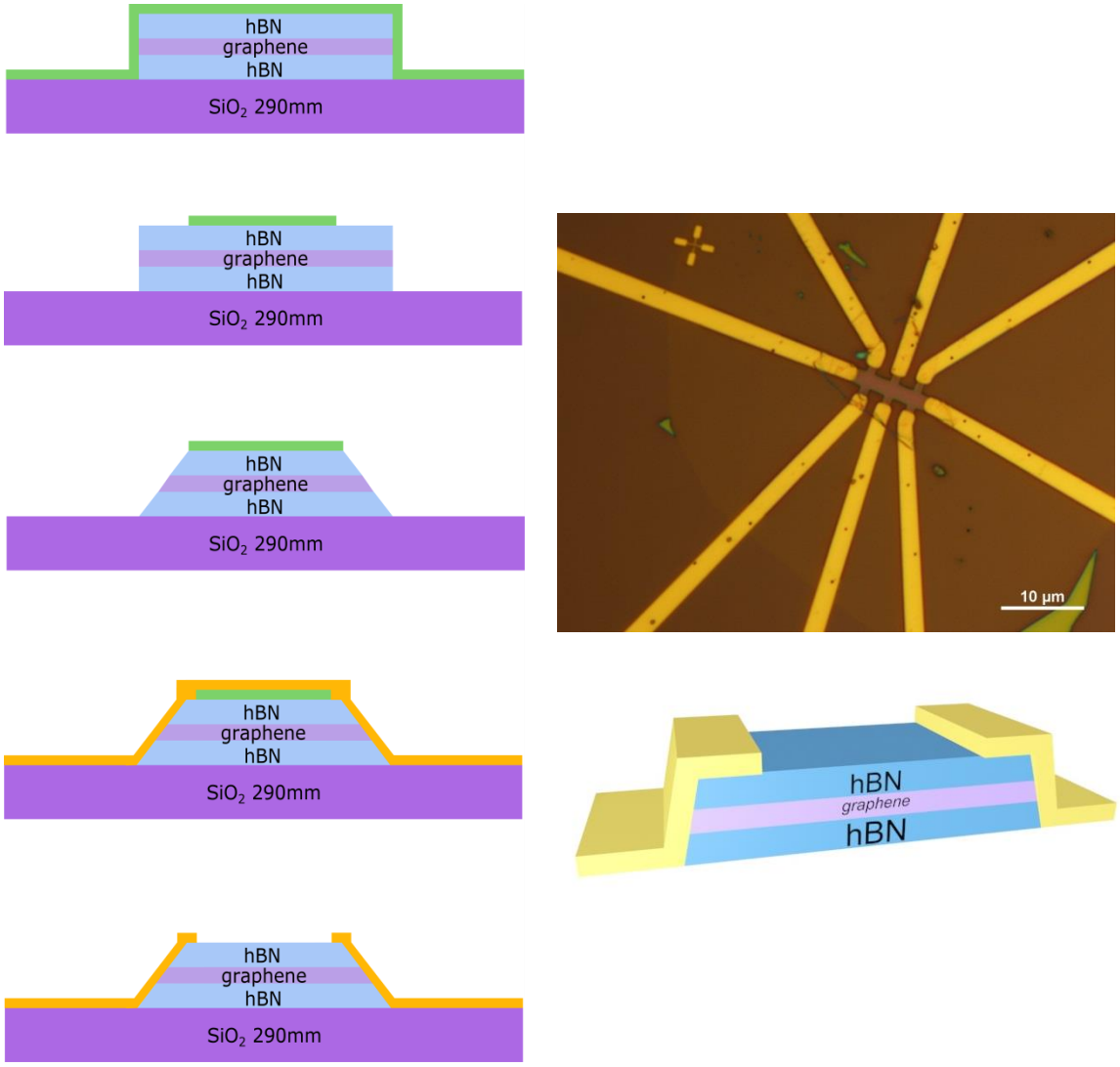

Fig. 4. 9 Schematic images of EBL exposure, etching and gold evaporation. Left (from top to bottom): EBL exposes pattern on PMMA covered flakes. Exposed pattern developing and flake etching. Gold evaporation and lift off. Right (from top to bottom): Image of heterostructure device with gold contacts and the zoomed in image of 1D contact.

Chapter 5

Results and discussion of AFM characterization

5.1 Introduction

In this chapter, the results of the AFM characterisation of single and double aligned hBN/graphene/hBN heterostructures are discussed. Moiré superlattices topography from the flat surface and bubbles are investigated. This method of investigation helps to provide quick proof of the existence of double alignment.

5.2 AFM characterization of aligned heterostructures

5.2.1 Moiré superlattices of aligned graphene/hBN heterostructures

FastScan AFM (Bruker Ltd.) PeakForce QNM mode is used to investigate the alignment of the graphene/hBN heterostructures. The Scanasyst-Fluid+ AFM tip is selected. To achieve high-resolution images, the adhesion force (nN) from the force curves is kept at $0 \sim -2nN$, to preserve a sharp tip when scanning. Nanoscope analysis and WSxM software are used to analyse the raw data. Fig. 5.1 demonstrates the height images of the moiré pattern from the graphene/monolayer hBN/bulk hBN aligned sample. The period of the moiré pattern is 15 nm.

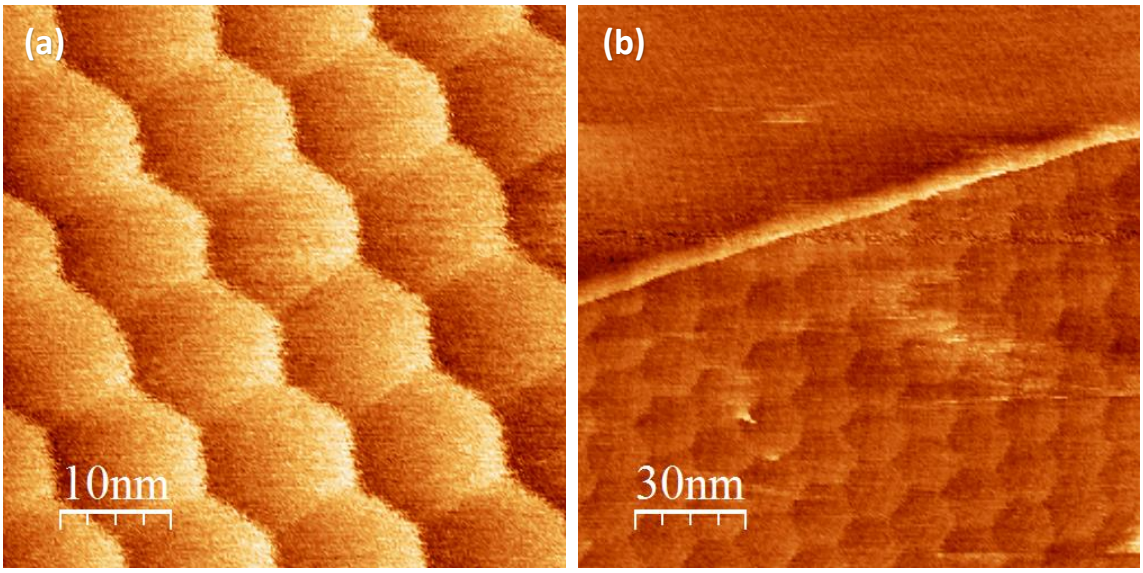

Fig. 5. 1 AFM images of moiré pattern from graphene/hBN heterostructure. (a) Height image of moiré pattern from aligned graphene on monolayer hBN with a period of 15 $\boldsymbol{nm}$. (b) Zoom out height image with graphene edge where moiré pattern ends.

Fig. 5.2 (a) shows the stretched aligned area where the period of the moiré pattern is 20 nm along the stretching direction (indicated with a white arrow). Fig. 5.2 (b) is the folded edge of the monolayer hBN beneath graphene, where alignment still occurs. One phenomenon that is worth discussing is shown in Fig. 5.2 (c), where the moiré pattern appears in the part B bubble but has vanished in the part A bubble. This is because the A bubble is located between the graphene and monolayer hBN, which prevents the alignment from occurring, while the B bubble is located between the monolayer hBN and bulk hBN, where the alignment of the graphene and monolayer hBN still exists.

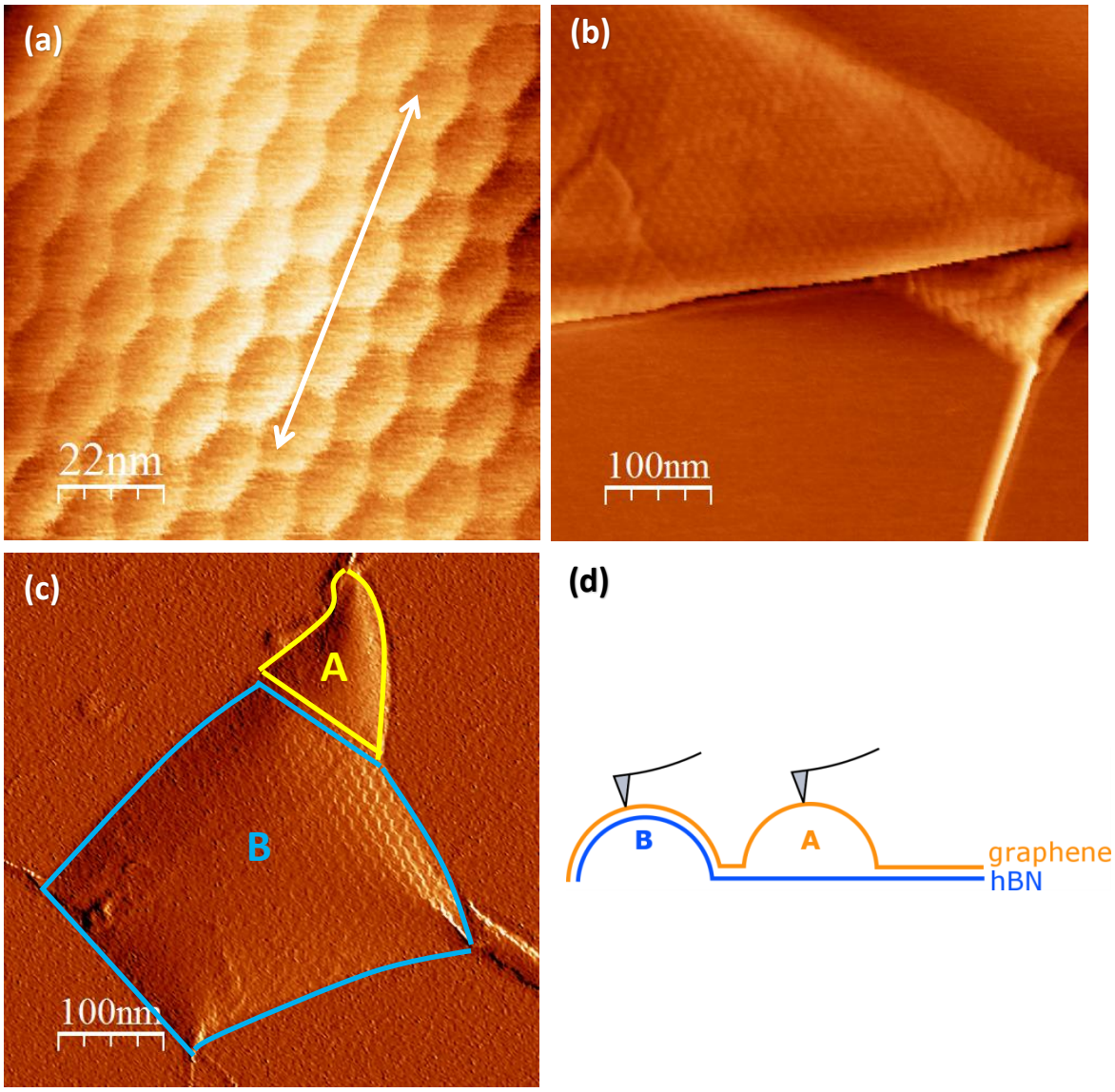

Fig. 5. 2 AFM images of different alignment situation. Height images of (a) stretched moiré pattern with 20 ***nm*** period, (b) folded edge of hBN beneath graphene and (c) bubble A between graphene and hBN and bubble B between hBN and bulk hBN substrate. (d) Schematic demonstration of AFM tip scanning two different bubbles, in accordance with (c).

5.2.2 Moiré superlattices of aligned TMDCs heterostructures

In the case of aligned TMDCs heterostructures, WSe_2, WS_2, $MoSe_2$ and MoS_2 are investigated. By knowing the lattice constant a for each material, the moiré wavelength as a function of relative rotation angle ϕ can be calculated.

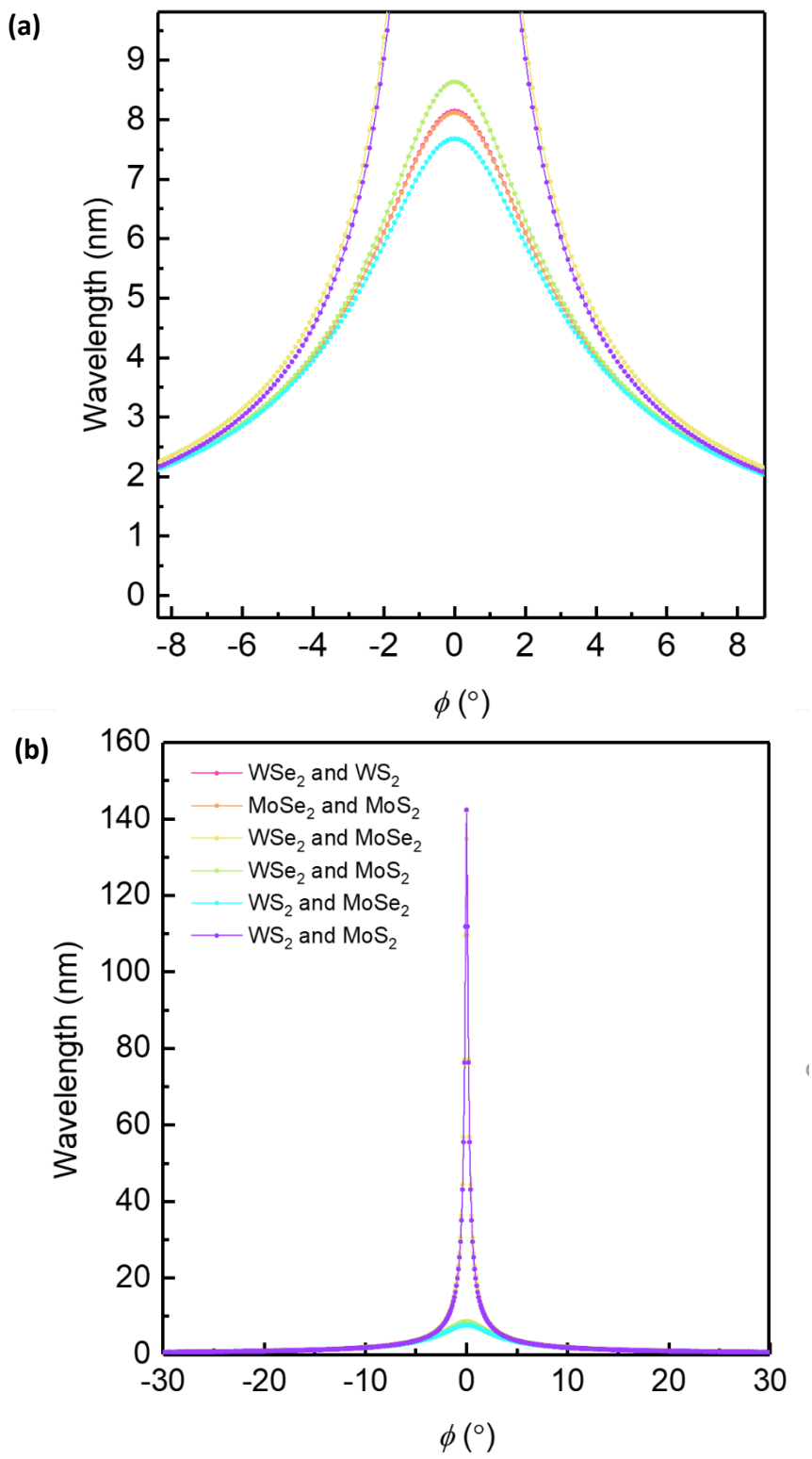

Fig. 5. 3 Six different combinations of selected TMDCs heterostructures' moiré wavelength λ as a function of relative rotation angle ϕ (between two different lattices). Small scale image (a) is zoomed in area of (b) the biggest possible moiré wavelength λ with the type of heterostructures WSe_2 and WS_2, $MoSe_2$ and MoS_2, WSe_2 and MoS_2, WS_2 and $MoSe_2$.

One interesting phenomenon shown in Fig. 5.3 is that the two types of heterostructure, WSe_2 and $MoSe_2$, and WS_2 and MoS_2, have the biggest moiré wavelength λ up to around 135 nm and 140 nm. The biggest moiré wavelength λ of other types of heterostructure does not reach 9 nm. This is because the two types of heterostructure have the same chalcogen atoms: Se or S. The small difference $\delta = a_{\mathrm{WSe2}}/a_{\mathrm{MoSe2}} - 1$ between the two crystals' lattice constants are relatively small, resulting in a bigger moiré wavelength.

Fig. 5.4 shows the AFM images of the aligned WS_2/ WSe_2 heterostructure. Fig. 5.5 shows the WS_2/ WSe_2 heterostructure's moiré wavelength λ as a function of relative rotation angle ϕ. Compared with the graphene/hBN heterostructure, the moiré pattern of the WS_2/ WSe_2 heterostructure is in a form without sharp edges, while it still has a periodical size around 6.6 nm.

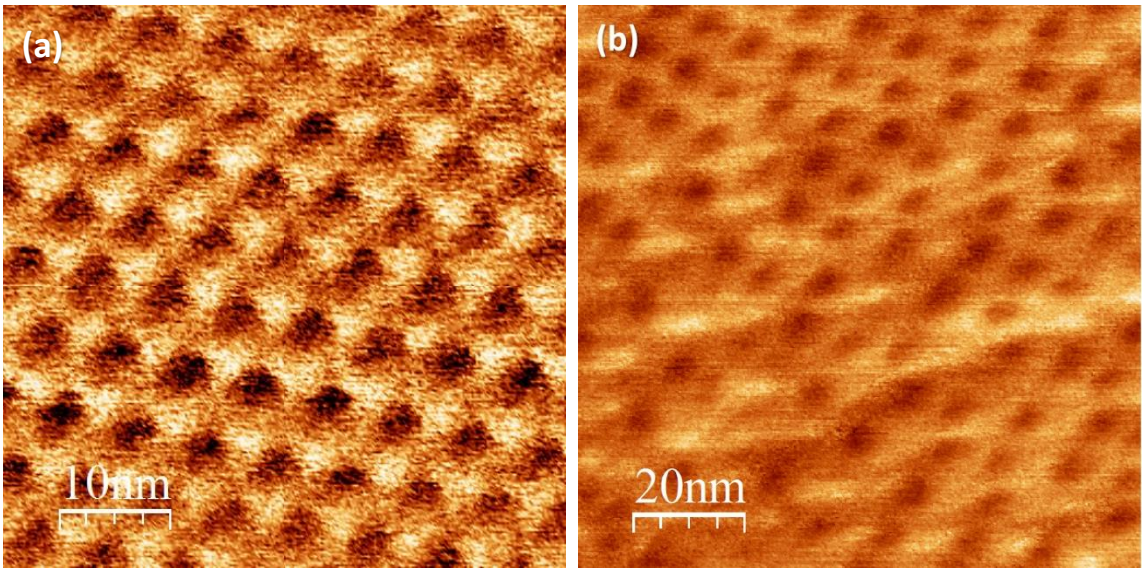

Fig. 5. 4 AFM images of moiré pattern from WS_2/WSe_2 heterostructure. (a) Deformation images of moiré pattern in WS_2/ WSe_2 heterostructure, moiré wavelength is around 6.6 $\boldsymbol{nm}$. (b) Height images of moiré pattern in monolayer WSe_2 / monolayer WS_2 heterostructure on suspended PMMA membrane.

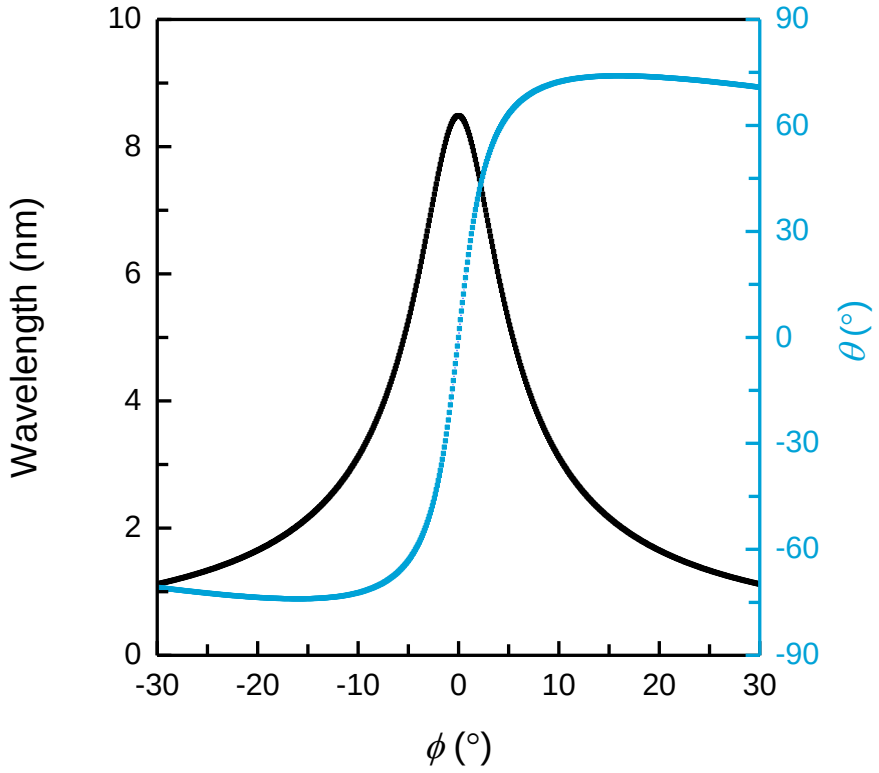

Fig. 5. 5 WS_2/WSe_2 heterostructure's moiré wavelength λ as a function of relative rotation angle ϕ.

5.2.3 Thin layer hBN/ graphene/ hBN double aligned heterostructures

The fabrication process for the double aligned thin-layer hBN/graphene/hBN heterostructure is slightly different than described in Chapter 4.5. Graphene is exfoliated from the PMMA/PMGI Test Si wafer, and is transferred to the pre-selected bulk hBN on SiO_2 290 nm. AFM characterisation and Raman spectroscopy techniques are used to investigate the alignment and moiré period (single alignment). A relatively large area of the moiré pattern is investigated and confirmed by AFM with period 8.75 nm. Thin-layer hBN is exfoliated from the PMMA/PMGI Test Si wafer, and is transferred on top of the aligned graphene/hBN stack, as shown in Fig. 5.6.

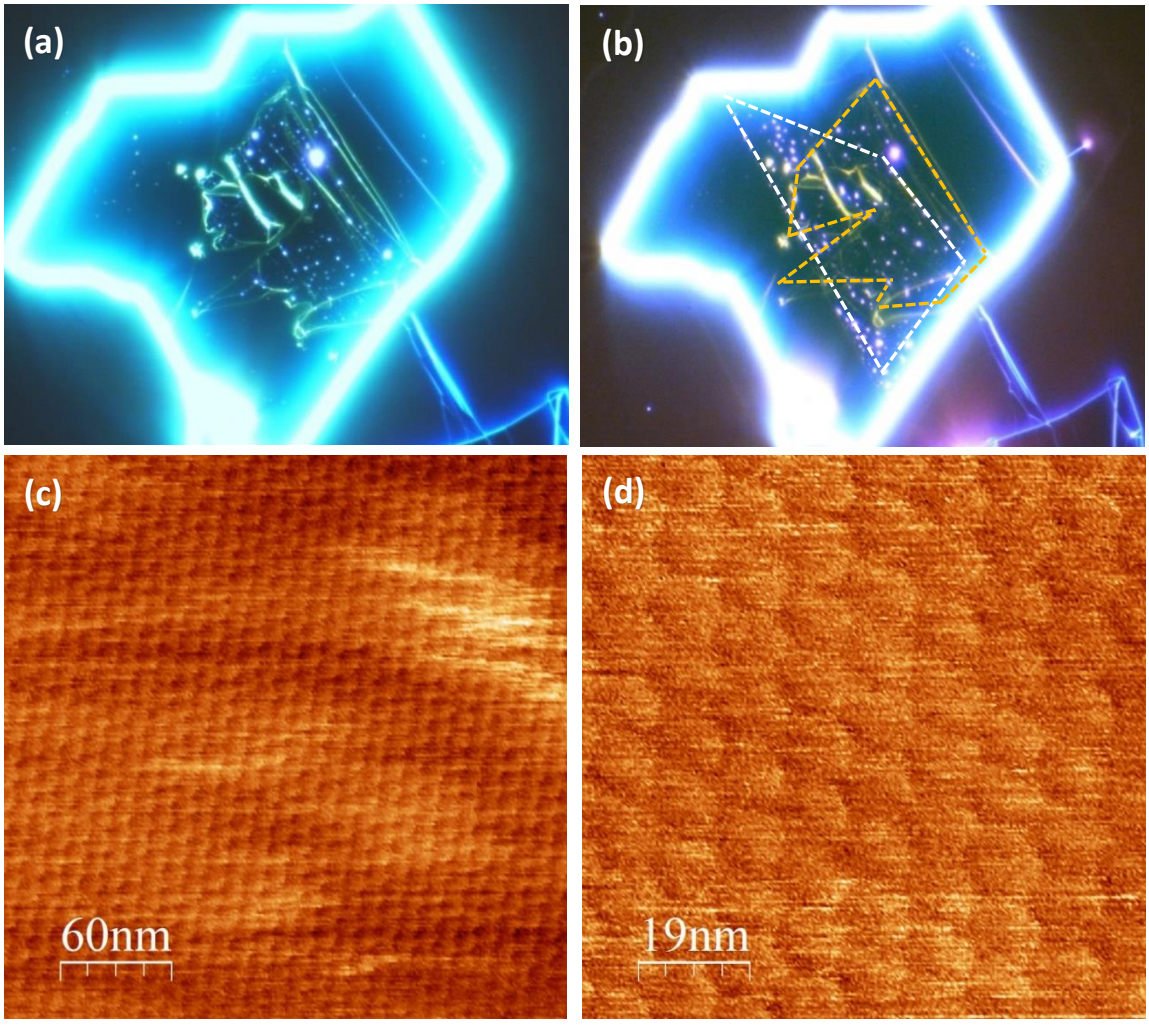

Fig. 5. 6 Optical images and AFM images of aligned hBN/graphene/hBN heterostructures. (a) single aligned graphene/hBN heterostructure. (b) double aligned hBN/graphene/hBN heterostructure. White dash line refers to bilayer hBN, yellow dash line refers to graphene. (c) Single alignment with average moiré period 8.75 $\boldsymbol{nm}$, (d) double alignment with average moiré period 12nm.

To further prove that the top bilayer hBN is aligned with the graphene, the moiré pattern on the bubbles is carefully characterised using AFM scanning. Fig. 5.5 shows the two separate bubbles, A and B. The A bubble is formed between the graphene and the bottom hBN; the B bubble is formed beneath the bottom hBN. This further indicates that the graphene is aligned with both top and bottom hBN simultaneously.

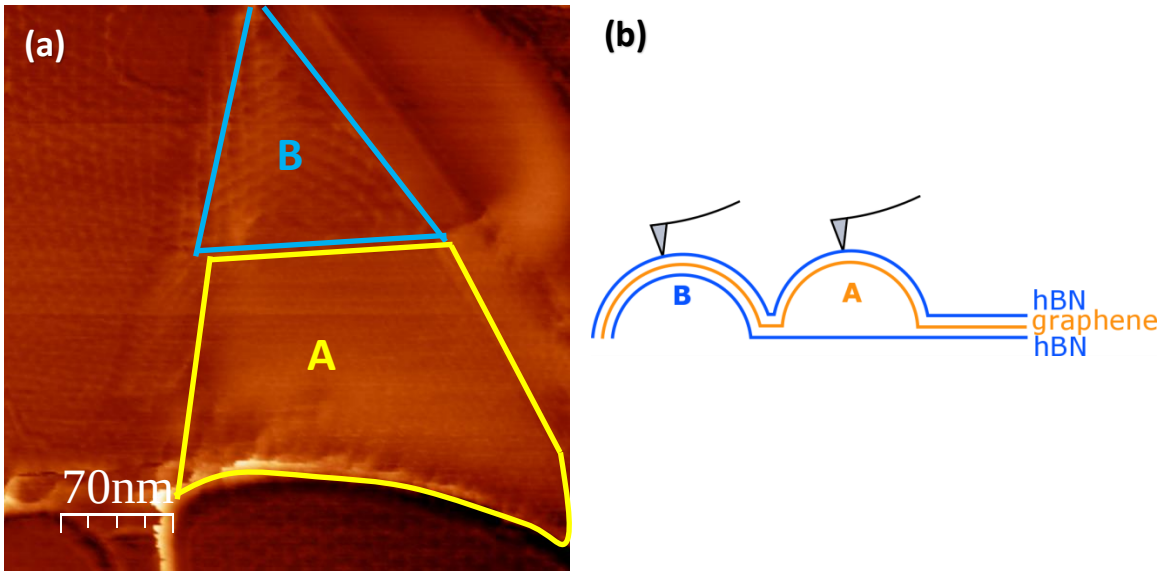

Fig. 5. 7 AFM images of moiré pattern on bubbles. (a) Deformation images of two contiguous bubbles further proved double alignment. (b) Schematic demonstration of AFM tip scanning two different bubbles, in accordance with (a).

5.2.4 Simulation of single alignment and double alignment hBN/ graphene/hBN heterostructures

Fig. 5.6 presents the single aligned graphene on hBN with a 2 degree aligned angle (a) and a 0 degree aligned angle (b). While the double aligned hBN/graphene/hBN has 2 degrees between the top hBN and the graphene, there are 3 degrees between the graphene and the bottom hBN (c). The wavelength moiré superlattices of the double-aligned hBN/graphene/hBN heterostructure increased compared to its counterparts. Further discussion is presented in Chapter 6.

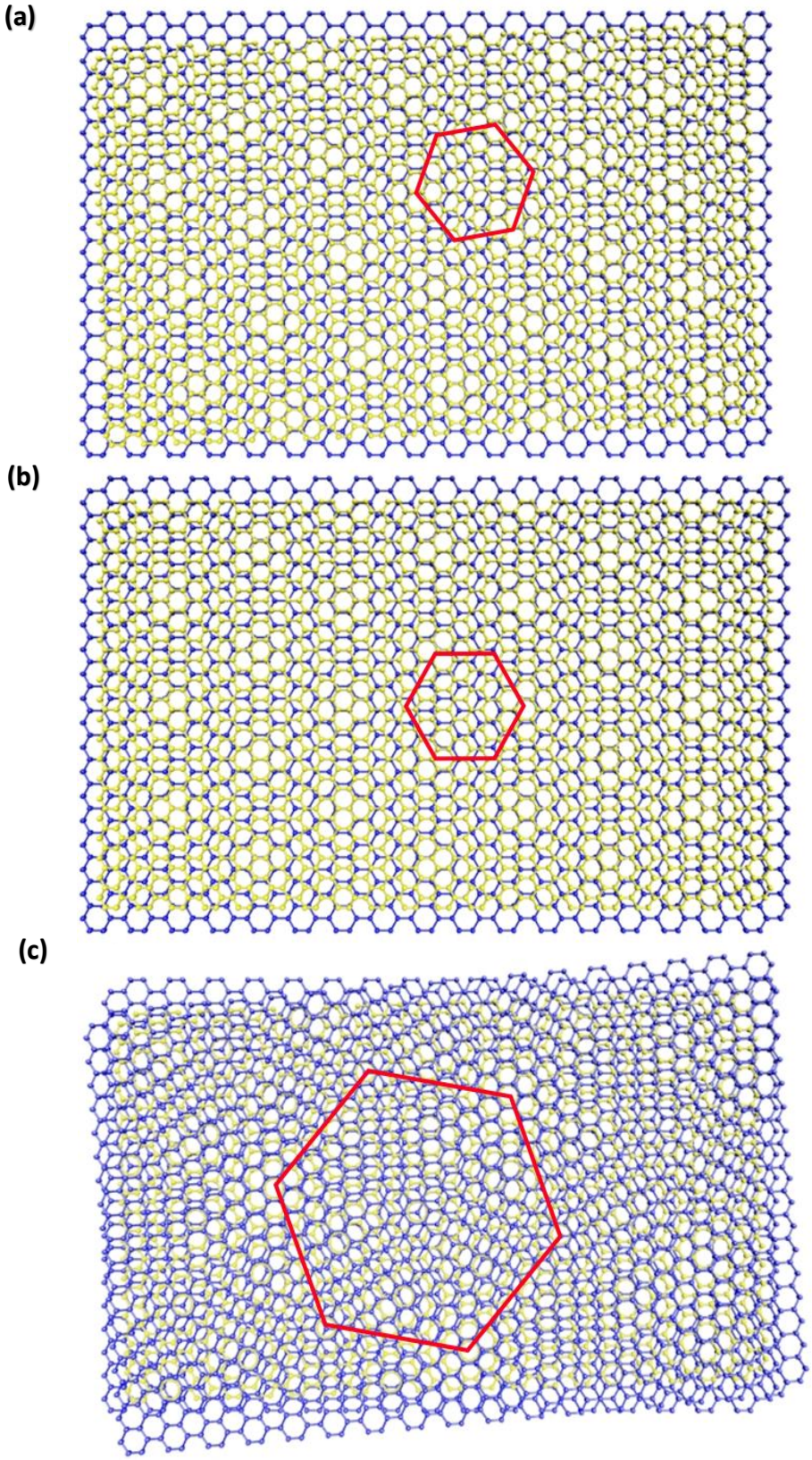

Fig. 5. 8 Schematic simulations of single aligned and double aligned hBN/graphene/hBN heterostructures.

Chapter 6

Results and discussions

Composite super-moiré lattices in double aligned graphene heterostructures

The results are from a manuscript submitted to Science Advances, 26th July 2019. No. aay8897.

As rotation-angle-dependent moiré lattices appear in graphene and hBN heterostructures, the electronic spectra result from the periodic potential and consequentially secondary Dirac points present. In this work, we present the model of an hBN/graphene/hBN heterostructure, in which the graphene is aligned with both the top and bottom hBN layers. It should be noted that the super-moiré lattices result in electronic spectra reconstruction and crystal reconstruction. And it provides more opportunity to tune the spectrum in the low energy regime.

PMMA/PMGI and PDMS transfer methods are used to fabricate the device. The Peak Force QNM AFM technique is used to investigate the moiré lattices' period and heterostructure layer thicknesses. To confirm that the device is double aligned, Fourier transformation of AFM images are analyzed; and two sets of hexagonal peaks indicating two moiré periods. Raman Spectroscopy is used to investigate the strain distribution in overlapped areas. Also, the 2D Raman peaks increase by a factor of 2 for double aligned heterostructures than those of their single aligned counterpart.

My contribution to the work includes: flake preparation, single and double aligned heterostructures fabrication, AFM studies of single and double aligned heterostructure moiré periods. Raman Spectroscopy studies of strain distribution. Lithography and gold evaporation for device contact growth.

Composite super-moiré lattices in double aligned graphene heterostructures

Zihao Wang[1♦], Yi Bo Wang[1♦], J. Yin[1], Y. Yang[2], L. Lin[2], M. Holwill[2], J. Birkbeck[2], D. J. Perello[2], S. Xu[2], J. Zultak[2], R. V. Gorbachev[1,2,3], A. V. Kretinin[2,4], T. Taniguchi[5], K. Watanabe[5], S. V. Morozov[6], M. Anđelković[7], S. Milovanović[7], L. Covaci[7], F.M. Peeters[7], A. Mishchenko[1,2], A. K. Geim[1,2], K. S. Novoselov[1,2], Vladimir Fal'ko[1,2,3], Angelika Knothe[2]*, C. R. Woods[1,2]*

♦ These authors contributed equally.

* Corresponding Author (CRW: colin.woods@manchester.ac.uk, AK: angelika.knothe@manchester.ac.uk)

[1]School of Physics and Astronomy, University of Manchester, Oxford Road, Manchester, M13 9PL, UK

[2]National Graphene Institute, University of Manchester, Oxford Road, Manchester, M13 9PL, UK

[3]Henry Royce Institute for Advanced Materials, Oxford Road, Manchester, M13 9PL, UK

[4]School of Materials, University of Manchester, Oxford Road, Manchester, M13 9PL, UK

[5]National Institute for Materials Science, 1-1 Namiki, Tsukuba, 305-0044, Japan

[6]Institute of Microelectronics Technology RAS, Chernogolovka 142432, Russia

[7]Department of Physics, University of Antwerp, Groenenborgerlaan 171, Antwerp, Belgium

When two-dimensional atomic crystals are brought into close proximity to form a van der Waals heterostructure, neighbouring crystals can start influencing each other's electronic properties. Of particular interest is the situation when the periodicity of the two crystals closely match and a moiré pattern forms, which results in specific electron scattering, reconstruction of electronic and excitonic spectra, crystal reconstruction, and many other effects. Thus, formation of moiré patterns is a viable tool of controlling the electronic properties of 2D materials. At the same time, the difference in the interatomic distances for the two crystals combined, determines the range in which the electronic spectrum is reconstructed, and thus is a barrier to the low energy regime. Here we

present a way which allows spectrum reconstruction at all energies. By using graphene which is aligned simultaneously to two hexagonal boron nitride layers, one can make electrons scatter in the differential moiré pattern, which can have arbitrarily small wavevector and, thus results in spectrum reconstruction at arbitrarily low energies. We demonstrate that the strength of such a potential relies crucially on the atomic reconstruction of graphene within the differential moiré super-cell. Such structures offer further opportunity in tuning the electronic spectra of two-dimensional materials.

Main Text:

Van der Waals heterostructures allow combining different two-dimensional (2D) materials into functional stacks[1,2], which has already produced a range of interesting electronic[3,4] and optoelectronic[5-8] devices and resulted in observation of exciting physical phenomena. The large variety of the heterostructures is mainly due to the large selection of 2D materials. However, the assembly of van der Waals heterostructures allow one extra degree of freedom: apart from the selection of the sequence of the 2D crystals – the individual crystals can be differently oriented with respect to each other. Previously such control over the rotational alignment between crystals resulted in the observation of the resonant tunnelling[9-11], renormalisation of exciton binding energy[12] insulating[13] and superconducting[4] states.

Probably one of the most spectacular results of the rotational alignment between different 2D crystals is the observation of the band-reconstruction due to electron scattering on the moiré pattern in graphene aligned with hexagonal boron nitride (hBN). Because the lattice constants of graphene and hBN are relatively close to each other, the alignment between the two crystals leads to the formation of a moiré pattern[14,15] with relatively small wavevector, which results in the appearance of the secondary Dirac points[16-18] in the electronic spectrum. Furthermore, the strong van der Waals interaction also leads to the atomic reconstruction of the graphene lattice[19-22]. Unfortunately the characteristic energies at which the electronic spectrum can be reconstructed are given by the difference between the lattice constants of graphene and hBN, which doesn't allow changes to be made to the low energy part of the spectrum.

Here, we demonstrate how we can gain further control over the band reconstruction of graphene by utilising the differential between two moiré patterns (super-moiré) created by top and bottom hBN in hBN/graphene/hBN heterostructures. Such super-moiré patterns are not related to the difference in the lattice constants between the two crystals and thus can be of any arbitrary wavenumber, which makes it possible to arrange the spectrum reconstruction at arbitrary low energies.

To this end we created encapsulated graphene devices where the graphene layer was aligned to both bottom and top hBN layers (alignment angles θ^{α} and θ^{β}). The fabrication and transfer procedures have been previously described in [23] with the exception that not only the bottom but also the top hBN is now crystallographically aligned to the graphene. In brief, we started by identifying the top-hBN layer on SiO_2. We then use a thin film of PPC on PDMS to lift the hBN from its substrate. This film then facilitates bringing the top-hBN into contact with a graphene crystal, Fig. 1a,b. We use very long and straight edges of the crystals to identify crystallographic axes and align them using a commercially available transfer rig[24]. The graphene can then be lifted away from its substrate, Fig. 1b. At this point, we perform atomic force microscopy[14,15,19] and Raman spectroscopy[25] experiments on the hBN/graphene bilayer to confirm the alignment. One such AFM image is presented in Fig. 1e, clearly showing the characteristic hexagonal pattern (the Fourier transformation is shown in Fig. 1h). The crystals are then aligned and brought into contact with a second thin hBN-layer (typically less than 1.5 nm or 5 atomic layers thick), Fig. 1b. This layer is also lifted away from its substrate leaving a triple layer on the thin polymer film, Fig. 1c. We then perform AFM and Raman characterisation again. Fig. 1f and Fig. 1i are an example of one of our double-aligned moiré AFM images and its Fourier transformation for the case of the second hBN layer being 1 atomic layer thick, which allows one to see both moiré patterns simultaneously. Although not immediately clear in the real-space image, the Fourier transformation clearly shows two sets of peaks corresponding to two hexagonal patterns (red and green dashed hexagons), as also schematically shown on Fig. 1d. The triple layer is then misaligned (~15°) and placed on top of a thick substrate-hBN (Fig. 1c). Finally, we use standard lithographic techniques to create the Hall-bar geometry.

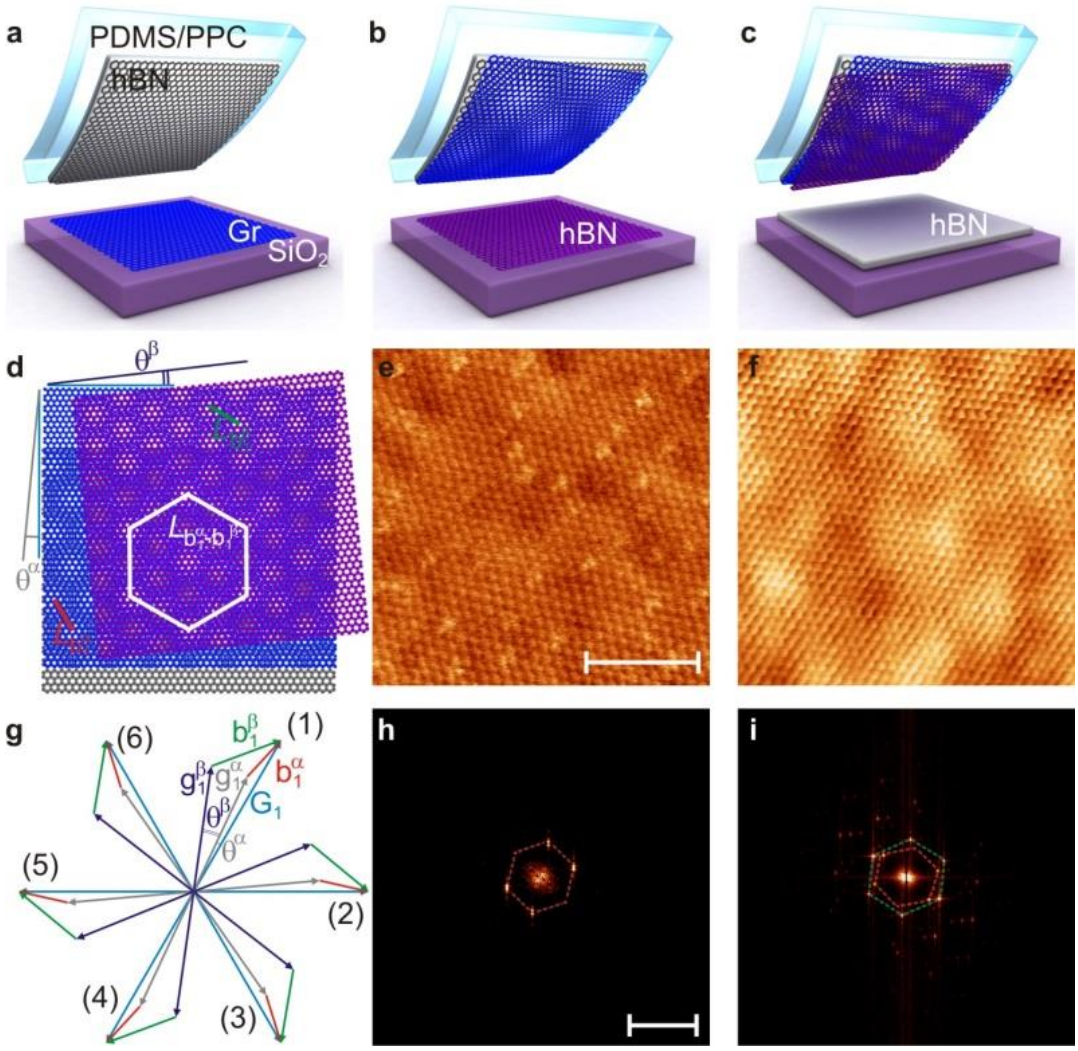

Fig. 1: Device fabrication and characterisation. ***a*** *Step (1) A thick hBN layer is aligned and used to pick up graphene.* ***b*** *Step (2) a thin-hBN layer is aligned and picked up forming a triple layer.* ***c*** *Step (3) The heterostructure is placed on top of a thick-hBN layer at 15° rotation angle (The substrate).* ***d*** *Illustration of the two individual moiré patterns and super-moiré pattern for three overlapping hexagonal lattices.* ***e*** *AFM image of the moiré pattern after the graphene is picked up. This shows only one moiré periodicity.* ***f*** *AFM image of the moiré patterns after the second thin-hBN is picked up. Here periodicities due to both hBN layers are visible.* ***g*** *Reciprocal space image of graphene's first Brillouin zone.* $\boldsymbol{G}_1$ *(blue),* $\boldsymbol{g}_1^{\alpha}$*(grey), and* $\boldsymbol{g}_1^{\beta}$ *(purple) are the reciprocal lattice vectors for graphene and the α and β hBN layers, respectively. α and β are at angles* θ^{α} *and* θ^{β} *relative to graphene.* $\boldsymbol{b}_1^{\beta}$ *(green) is the moiré between graphene and the β hBN.* $\boldsymbol{b}_1^{\alpha}$ *(red) is the moiré between graphene and the α hBN.* ***h*** *Fourier transformation of the image in* ***e****, displaying only one hexagonal periodic pattern (red dashed hexagon).* ***i*** *Fourier transformation of the image in* ***f****, showing two sets of distinct hexagonal patterns (red and green dashed hexagons). The scale bar in* ***e*** *is 100nm (****f*** *shares this scale). The scale bar in* ***h*** *is 0.2nm*$^{-1}$ *(****i*** *shares this scale).*

The longitudinal resistance (R_{xx}) as a function of carrier concentration is presented on Fig. 2a. Here, apart from the resistance peak associated with the main Dirac point[26], several additional peaks can be seen. Most of such peaks correspond to the change of sign of the transversal (Hall) resistance (R_{xy}) measured in non-quantised magnetic field, Fig. 2b. Typically, if graphene is aligned with only one hBN, a single moiré pattern is produced, and only one secondary Dirac point for electrons and one for holes can be seen at concentrations which correspond to the wavevector determined by the periodicity of the moiré pattern[14-18]. Aligning graphene to both the top and the bottom hBN will produce two moiré patterns (if $\theta^{\alpha}$and θ^{β} are not equivalent), which should result in two secondary Dirac points for electrons and two for holes. However, if electrons can feel potential from both moiré patterns simultaneously, then second order processes can be allowed, which would result in the reconstruction of the electronic spectrum at many other wavevectors.

In quantized magnetic fields, Landau fans can be seen to originate from these peaks, Fig. 2c. The Landau fans for most peaks exhibit both positive and negative indexes (positive and negative slopes in Fig. 2c), which suggests that those are indeed originating from the additional Dirac points and not from the higher order zone edges[27].

To interpret these additional peaks we recall that the perfectly aligned graphene on hBN should produce moiré pattern with approximately 14nm periodicity, which corresponds to carrier concentration $n \approx 2.3\times10^{12}$ cm^{-2}. Thus, for our double-aligned graphene we interpret the most pronounced peaks at $\pm1.98\times10^{12}$ cm^{-2} and $\pm2.34\times10^{12}$ cm^{-2} as coming from the moiré patterns from the top and bottom hBN layers.

The periodicity of a moiré pattern, L, can be related to the carrier concentration required to reach edge of its first Brillouin zone by, $n_{SDP} = \frac{8}{\sqrt{3}L^2}$. Utilising this, we get periodicities of 15.3nm and 14.0 nm respectively for the two most prominent features. The moiré periodicities are dependent upon both the lattice constant mismatch and the alignment angle, as given by $b^{\alpha,\beta} = \left|\boldsymbol{b}_n^{\alpha,\beta}\right| = \frac{4\pi}{\sqrt{3}a}\sqrt{\delta^2 + {\theta^{\alpha,\beta}}^2}$, where $\boldsymbol{b}_n^{\alpha,\beta} = \boldsymbol{G}_n - \boldsymbol{g}_n^{\alpha,\beta}$ (n = 0,..,5) are the moiré reciprocal lattice vector between the α or β hBN layer (with reciprocal lattice vectors $\boldsymbol{G}_n^{\alpha,\beta}$) and graphene (with reciprocal lattice vectors $\boldsymbol{G}_n$), δ is graphene-hBN lattice constant mismatch, $\theta^{\alpha,\beta}$ is the misalignment angle for α or β, and a is graphene's lattice constant. Interestingly, one of the observed periods is larger

than that could be expected for graphene aligned with hBN (~15.3nm, see[14-19]). We attribute this slightly larger moiré period to stretching of graphene as it interacts more strongly with the two aligned hBN layers. Since the angle is zero, or sufficiently close to zero ($\delta \gg \theta$), we may calculate a new δ. In this case, the lattice mismatch to achieve the periodicity of 15.3nm should be ~1.64%. This corresponds to ~ 0.15% strain in the graphene crystal.

Then we would like to notice the small peaks at $\pm 0.35\times10^{12}$ cm^{-2} which corresponds to the largest differential moiré pattern. From the carrier concentration we can infer a periodicity of 35 nm. Further still, there is a pronounced peak at approximately $\pm 0.90\times10^{12}$ cm^{-2}, which would yield a period of 22.7nm. These features represent previously impossible periodicities for the graphene/hBN moiré pattern.

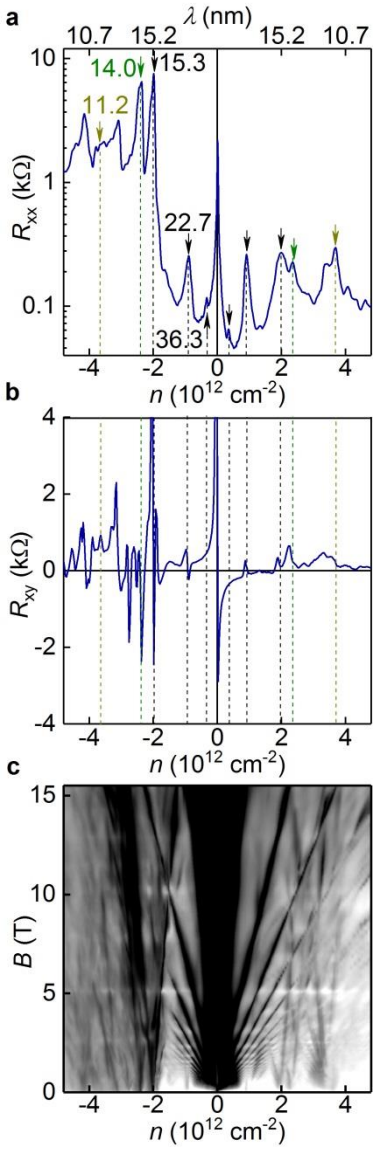

Fig. 2: Transport properties of doubly-aligned hBN/graphene/hBN device. a *R_{xx} as a function of n for one of our devices with b ≈ 15.3nm ($\varphi_1 = 0^\circ$), b' ≈ 14.0nm ($\varphi_2 = 0.4^\circ$). Lattice mismatch, δ, is taken as 1.64%. The moiré and super-moiré peaks are marked by arrows and also labelled with their periods on hole side in the unit of nanometres. The position of the peaks is symmetric w.r.t holes and electrons. The top axis mark is labelled in the size of the moiré pattern which corresponds to the particular carrier concentration. Dashed lines correspond to the arrows and can be traced to those in (b).* ***b****. R_{xy} for the same device measured at B = 0.2T. The dashed lines can be traced to the arrows in (a) and correspond to the particular peaks in R_{xx}.* ***c*** *Fan diagram $\sigma_{xx}(n, B)$ for the same device (Scale black to white 0.5 e^2/h to 70 e^2/h). All measurements are done at T = 1.7K.*

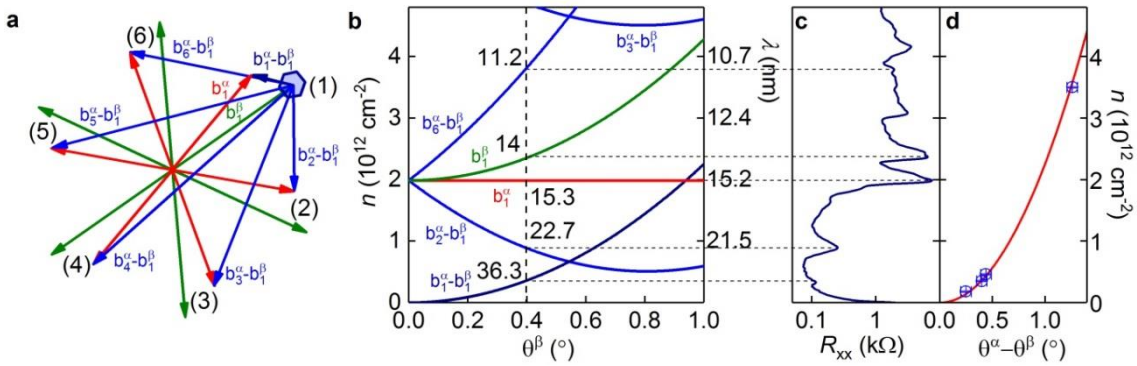

Fig. 3: Super-moiré geometry. ***a*** *Reciprocal-space image of the area around graphene's K-point.* b_m^α *(green) and* b_m^β *(red) for m = 1,2..6 are the graphene-hBN moiré reciprocal lattice vectors.* $b_1^\alpha - b_m^\beta$ *(blue) are the six super-moiré reciprocal lattice vectors. The blue hexagonal area indicates the* $b_1^\alpha - b_1^\beta$ *first Brillouin zone.* ***b*** *Carrier concentration of the first Brillouin zone edge for the two moiré and four lowest-energy super-moiré features as a function of* $\theta^\beta (\delta = 1.64\%, \theta^\alpha = 0°)$. ***c*** R_{xx} *peak positions in carrier concentration. Dashed lines connect values of carrier concentration for* θ^β*=0.4 in* ***b*** *to the position in* ***c****. Each line matches a peak.* ***d*** *carrier concentration of the* $b_1^\alpha - b_1^\beta$ *super-moiré feature vs* $|\theta^\alpha - \theta^\beta|$ *for four of ours samples (blue circles) and by calculation (red line).*

In Fig. 3a, we schematically describe the geometric origin of the super-moiré features. $\boldsymbol{b}_m^\alpha$ and $\boldsymbol{b}_k^\beta$ (red and green vectors, m = 1,2,..6, k = 1,2,..6) are the α and β moiré patterns. Their combination produces six new super-moiré patterns by the combinations of the vectors. In Fig. 3a we highlight the $\boldsymbol{b}_1^\alpha - \boldsymbol{b}_k^\beta$ vectors (blue). In Fig. 3b we present the position of the moiré and super-moiré zone edges in carrier concentration as a function of the angle between the second hBN layer (θ^β) and graphene for the case when the first hBN layer is held at zero angle mismatch ($\theta^\alpha = 0$), and $\delta = 1.64\%$, as calculated. For θ^β = 0.4°, the features correspond exactly to the observed peaks in R_{xx} (as shown by the dotted lines connecting Fig. 3b and Fig. 3c), and sign reversal of R_{xy}, thus revealing the presence of new secondary Dirac points in the low energy electronic spectrum. Such low energy peaks originate from the differential super-moirés, $b_1^\alpha - b_1^\beta$, $b_1^\alpha - b_6^\beta$, and $b_1^\alpha - b_2^\beta$. Further, in Fig. 3d, we show the position of the R_{xx} peak in carrier concentration for the $b_1^\alpha - b_1^\beta$ super-moiré, against the calculated angle between the two hBNs ($|\theta^\alpha - \theta^\beta|$). This peak is unique because its period is independent of the graphene sheet as it is geometrically identical to moiré pattern between the two hBN layers. As expected,

Fig. 3d shows the peak position for four of our samples (blue circles) follows exactly expectation (red line).

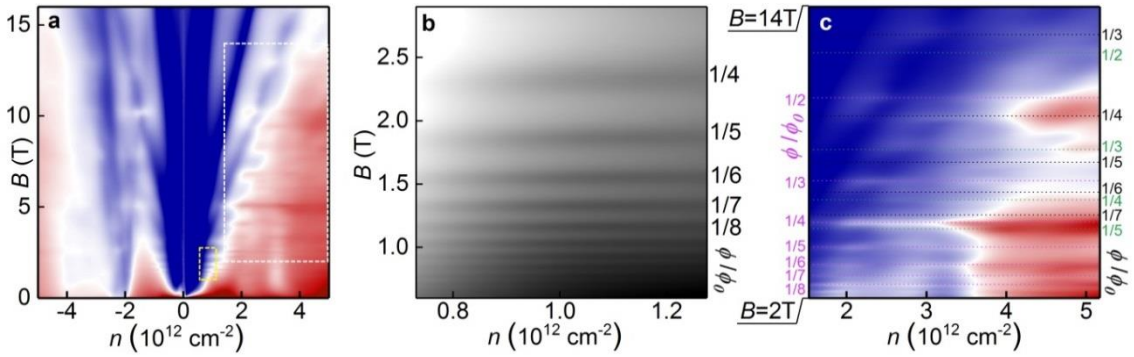

Fig. 4: Brown-Zak oscillations in one of our doubly-aligned hBN/graphene/hBN devices. a *Map of* $\sigma_{xx}(n, B)$*, scale of blue to red is* $0.5e^2/h$ *to* $70e^2/h$*.* ***b*** *Zoom in into the low field part of the map, marked by yellow rectangle in (a), scale of black to white is* $7e^2/h$ *to* $37e^2/h$*. The Brown-Zak oscillations correspond to a moiré structure with periodicity of 22.7nm and the fundamental field is 9.3T.* ***c*** *Zoom in into the high field part of the map, marked by white rectangle in (a), scale of blue to red is* $7e^2/h$ *to* $37e^2/h$*. The Brown-Zak oscillations correspond to a moiré structures of different periodicities are marked by dashed lines of different colours. Black - 15.3nm (*B_F*=20.5T), green 14.0nm (*B_F*=24.2T) and brown – 11.2nm (*B_F*=38T). All measurements are done at T = 70K.*

To check that all these peaks indeed originate from the spectrum reconstruction because of scattering on the additional periodic potential we measured the Brown-Zak oscillations at elevated temperatures (T) where cyclotron oscillations are suppressed, Fig. 4. At T > 70K oscillations independent of the carrier concentration can be clearly seen. At low fields B < 2.5T (Fig. 4b) the oscillations are clearly periodic in $1/B$ with the fundamental field B_f = 9.3T. Assuming a hexagonal unit cell, such fundamental field can be calculated to correspond to moiré periodicity of 22.7nm, which corresponds to the peak in R_{xx} at $n = \pm 0.90\times10^{12}$ cm^{-2}, Fig. 2a.

The behaviour at high fields is more complex, as several Brown-Zak oscillations which originate from different periodicities overlap. However, by taking the periodicities which correspond to the most prominent peaks in R_{xx} at B = 0 (15.3nm, 14nm and 11.2nm, see Fig. 2a) we could identify most oscillations in terms of fractions of the flux quantum per the corresponding plaquette, labelled in Fig. 4c. Thus, the graphene-hBN moiré periods

(14.0 and 15.3 nm) and super-moiré periods (11.2 nm, 22.7 nm, and 36.3 nm) each give features attributable to secondary Dirac points at well understood values of carrier concentration. Also they produce clear Brown-Zak oscillations for unitary flux through moiré unit cells for the 11.2 nm, 14.0 nm, 15.3 nm, and 22.7 nm periods.

Further to our previous observations, we would like to note that there are several unexplained features in R_{xx} (Fig. 2a) and R_{xy} (Fig. 2b), most pronounced at $n_e \approx \pm 3.2\times10^{12}\text{cm}^{-2}$ and $n_e \approx \pm 4.1\times10^{12}\text{cm}^{-2}$. One possible explanation for these features is higher order moiré periodicities, that is, moiré patterns between super-moiré periods. However, the probability of such multiple scattering events diminishes strongly. Likewise, there could exist features due to super-moiré patterns between further zone edges (2nd, 3rd,… Brillouin zone edges of the graphene/hBN moirés) or a more exotic superlattice phenomenon.

Theoretically[28], moiré effects on graphene can be described in terms of a periodic superlattice (SL) potential applied to Dirac electrons produced by incommensurable lattices of two (top and bottom) hBN flakes,

$$\hat{\mathrm{H}} = v\boldsymbol{p}\bullet\boldsymbol{\sigma} + \sum_{j=\pm}\sum_{n=0\ldots5}\left[U_0^j + (-1)^n\left(iU_3^j\sigma_3 + U_1^j\frac{\boldsymbol{a_n}\bullet\boldsymbol{\sigma}}{a}\right)\right]e^{i\boldsymbol{b_n^j}\bullet(\boldsymbol{r}+j\frac{\boldsymbol{R}}{2})}\,e^{i\boldsymbol{G_n}\bullet\boldsymbol{u}(r,\boldsymbol{R})}. \quad (1)$$

Here, σ_3 and $\boldsymbol{\sigma} = (\sigma_1, \sigma_2)$ are Pauli matrices acting in the sublattice space of graphene's Bloch states; j=± identifies layers α (+) and β (-); U_0^j, U_1^j, and U_3^j parameterise a smoothly varying moiré potential, the asymmetric sublattice on-site energies, and hopping between A and B sublattices, respectively (based on the earlier studies[29-31], $U_0^j \approx 8.5$ meV, $U_1^j \approx -17$ meV, $U_3^j \approx -15$ meV for $\theta^j \ll \delta$). Vector $\boldsymbol{R}$ describes the phase shift between moiré produced by hBN flakes α and β.

From this, the super-moiré periods for the individual moiré SLs (α, β) in graphene originate in two ways. One is due to the quantum mechanical interference, which appears in the second order perturbation theory. In this case, Eq. (1) allows for the electron scattering from the combined j=± superlattices with the Bragg vectors $\boldsymbol{b}_m^\alpha - \boldsymbol{b}_k^\beta$. These comprise of different moiré SL reciprocal vectors, leading effectively to the SLs with Fourier components described in Fig. 1g and 3a. The second possibility is the reconstruction of graphene, which leads to a displacement field, $\boldsymbol{u}(r, \boldsymbol{R})$, generating mixing of the moiré SL's reciprocal vectors. When this is considered, the longest period

super-moiré SL ($m = 1, k = 1$) that determines the low-energy part of graphene spectrum can be described by following SL potential,

$$\hat{\mathrm{H}}_{1,1}^{P} \approx -12U_3\omega_{as}\sigma_3 - \sum_m \left[2U_3\omega_{as}\sigma_3 + \frac{4U_3U_1}{vb} + i\frac{2U_1^2}{vb}\frac{\boldsymbol{b_n}\bullet\boldsymbol{\sigma}}{b}\right] e^{i\boldsymbol{b}_m^{\alpha}\bullet\boldsymbol{R}} e^{i(\boldsymbol{b}_m^{\alpha}-\boldsymbol{b}_m^{\beta})\bullet\boldsymbol{r}}$$

$$\hat{\mathrm{H}}_{1,1}^{AP} \approx \sum_m \left[i(-1)^m 2U_0\omega_{as} - \frac{4U_3U_1}{vb} + i\frac{2U_1^2}{vb}\frac{\boldsymbol{b_n}\bullet\boldsymbol{\sigma}}{b}\right] e^{i\boldsymbol{b}_m^{\alpha}\bullet\boldsymbol{R}} e^{i(\boldsymbol{b}_m^{\alpha}-\boldsymbol{b}_m^{\beta})\bullet\boldsymbol{r}} \quad (2)$$

This expression was derived for $\theta^{\beta} \ll \delta$ for both parallel (P) and antiparallel (AP) mutual orientations of the two hBN crystals (hence, approximately, $\boldsymbol{b}_m^{\alpha} - \boldsymbol{b}_m^{\beta} \perp \boldsymbol{b}_m^{\alpha,\beta}$), and, here, ω_{as} parameterises the amplitude of inversion asymmetric component of strain.

Vital to this description is the understanding that the displacement field $\boldsymbol{u}(r, \boldsymbol{R})$ develops due to the competition between stacking-dependent van der Waals adhesion, of graphene and hBN, and elasticity of graphene. Previous work[19,20] has identified that the crystals form a 2D fixed-density commensurate state when graphene and hBN are close to perfect alignment. The effect relies upon strain, and thus $\boldsymbol{u}(r, \boldsymbol{R})$, modulating with a period matching that of the moiré pattern to minimise adhesive and elastic energy. The commensurate state is characterised by hexagonal domains with increasingly sharp domain walls near θ=0, observed in PeakForce atomic force microscopy[32], and broadening of the 2D-peak in the Raman spectrum[19,25].

To evaluate the degree of strain within our super-moiré samples we have employed Raman spectroscopy. In Fig.5a we show the 2D-peak and its full-width half-maximum (FWHM) for a typical unaligned sample (black circles), a sample aligned to one hBN (blue triangles), and one of our doubly aligned samples (red squares). In the case that the two hBN layers may be treated entirely independently, the signature in the Raman spectrum would remain unchanged from the singly-aligned case (FWHM (2D) ~ 36 cm^{-1}). However, it is clear that when a second aligned hBN layer is added, the width of the 2D-peak increases by a factor of ~ 2, Fig 5a. We attribute this to restructuring of strain within the super-moiré unit cells. This observation supports the proposed model of the two moiré patterns mixing through strain fields. Therefore, $\boldsymbol{u}(r, \boldsymbol{R})$ should have periodicities described by b_m^{α} (α-moiré), b_k^{β} (β-moiré), and $b_m^{\alpha} - b_k^{\beta}$ (super-moirés). This is also supported by molecular dynamics simulations of the relaxation in the doubly aligned systems, as shown in Fig. 5b, where the Raman spectra of simulated relaxed configurations is presented (see Supplementary Materials).

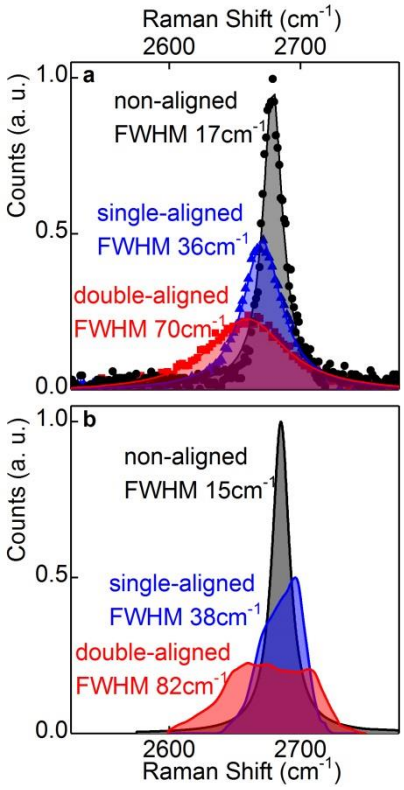

Fig. 5: Strain distribution in the aligned graphene-hBN heterostructures. *Raman spectra (2D-peak region) for an unaligned sample (grey), single-aligned sample (blue), and double-aligned sample (red). (**a**) Experimental results. (**b**) Molecular dynamics relaxation simulations.*

To conclude, graphene's electronic spectrum is significantly altered by scattering from super-moiré structures described by the pre-existing moiré between graphene and its substrate and encapsulating hBN layers. These alterations may be considered in two ways; as double scattering events from both graphene-hBN moiré patterns, or as single scattering events from a reconstructed graphene layer. Such super-moiré potential can be of arbitrarily small wavevector (unlike moiré potential from single hBN aligned with graphene), which allows modification of the graphene band structure at arbitrarily low energies.

Reference

1 Geim, A. K. & Grigorieva, I. V. Van der Waals heterostructures. *Nature* **499**, 419-425, doi:10.1038/nature12385 (2013).

2 Novoselov, K. S., Mishchenko, A., Carvalho, A. & Castro Neto, A. H. 2D materials and van der Waals heterostructures. *Science* **353**, aac9439-aac9439, doi:10.1126/science.aac9439 (2016).

3 Britnell, L. *et al.* Field-effect tunneling transistor based on vertical graphene heterostructures. *Science* **335**, 947-950, doi:10.1126/science.1218461 (2012).

4 Cao, Y. *et al.* Unconventional superconductivity in magic-angle graphene superlattices. *Nature* **556**, 43, doi:10.1038/nature26160 (2018).

5 Britnell, L. *et al.* Strong light-matter interactions in heterostructures of atomically thin films. *Science* **340**, 1311-1314, doi:10.1126/science.1235547 (2013).

6 Withers, F. *et al.* Light-emitting diodes by band-structure engineering in van der Waals heterostructures. *Nat. Mater.* **14**, 301-306, doi:10.1038/nmat4205 (2015).

7 Withers, F. *et al.* WSe2 light-emitting tunneling transistors with enhanced brightness at room temperature. *Nano Lett.* **15**, 8223-8228, doi:10.1021/acs.nanolett.5b03740 (2015).

8 Low, T. *et al.* Polaritons in layered two-dimensional materials. *Nature Materials* **16**, 182, doi:10.1038/nmat4792 (2016).

9 Lane, T. L. M., Wallbank, J. R. & Fal'ko, V. I. Twist-controlled resonant tunnelling between monolayer and bilayer graphene. *Appl. Phys. Lett.* **107**, 203506, doi:10.1063/1.4935988 (2015).

10 Wallbank, J. R. *et al.* Tuning the valley and chiral quantum state of Dirac electrons in van der Waals heterostructures. *Science* **353**, 575-579, doi:10.1126/science.aaf4621 (2016).

11 Mishchenko, A. *et al.* Twist-controlled resonant tunnelling in graphene/boron nitride/graphene heterostructures. *Nature Nanotechnology* **9**, 808, doi:10.1038/nnano.2014.187 (2014).

12 Alexeev, E. M. *et al.* Resonantly hybridized excitons in moire superlattices in van der Waals heterostructures. *Nature* **567**, 81-86, doi:10.1038/s41586-019-0986-9 (2019).

13 Cao, Y. *et al.* Correlated insulator behaviour at half-filling in magic-angle graphene superlattices. *Nature* **556**, 80-84, doi:10.1038/nature26154 (2018).

14 Xue, J. M. *et al.* Scanning tunnelling microscopy and spectroscopy of ultra-flat graphene on hexagonal boron nitride. *Nat. Mater.* **10**, 282-285, doi:10.1038/nmat2968 (2011).

15 Yankowitz, M. *et al.* Emergence of superlattice Dirac points in graphene on hexagonal boron nitride. *Nat. Phys.* **8**, 382-386, doi:10.1038/nphys2272 (2012).

16 Ponomarenko, L. A. *et al.* Cloning of Dirac fermions in graphene superlattices. *Nature* **497**, 594-597, doi:10.1038/nature12187 (2013).

17 Dean, C. R. *et al.* Hofstadter's butterfly and the fractal quantum Hall effect in moire superlattices. *Nature* **497**, 598-602, doi:10.1038/nature12186 (2013).

18 Hunt, B. *et al.* Massive Dirac fermions and Hofstadter butterfly in a van der Waals heterostructure. *Science* **340**, 1427-1430, doi:10.1126/science.1237240 (2013).

19 Woods, C. R. *et al.* Commensurate-incommensurate transition in graphene on hexagonal boron nitride. *Nat. Phys.* **10**, 451-456, doi:10.1038/nphys2954 (2014).

20 Woods, C. R. *et al.* Macroscopic self-reorientation of interacting two-dimensional crystals. *Nat. Commun.* **7**, 10800, doi:10.1038/ncomms10800 (2016).

21 Yankowitz, M., Watanabe, K., Taniguchi, T., San-Jose, P. & LeRoy, B. J. Pressure-induced commensurate stacking of graphene on boron nitride. *Nature Communications* **7**, 13168, doi:10.1038/ncomms13168 (2016).

22 Yankowitz, M. *et al.* Dynamic band-structure tuning of graphene moiré superlattices with pressure. *Nature* **557**, 404-408, doi:10.1038/s41586-018-0107-1 (2018).

23 Uwanno, T., Hattori, Y., Taniguchi, T., Watanabe, K. & Nagashio, K. Fully dry PMMA transfer of graphene onh-BN using a heating/cooling system. *2D Materials* **2**, 041002, doi:10.1088/2053-1583/2/4/041002 (2015).

24 Cao, Y. *et al.* Quality heterostructures from two-dimensional crystals unstable in air by their assembly in inert atmosphere. *Nano Lett.* **15**, 4914-4921, doi:10.1021/acs.nanolett.5b00648 (2015).

25 Eckmann, A. *et al.* Raman fingerprint of aligned graphene/h-BN superlattices. *Nano Lett.* **13**, 5242–5246, doi:10.1021/nl402679b (2013).

26 Novoselov, K. S. *et al.* Electric field effect in atomically thin carbon films. *Science* **306**, 666-669, doi:10.1126/science.1102896 (2004).

27 Kumar, R. K. *et al.* High-temperature quantum oscillations caused by recurring Bloch states in graphene superlattices. *Science* **357**, 181-184, doi:10.1126/science.aal3357 (2017).

28 Wallbank, J. R., Patel, A. A., Mucha-Kruczynski, M., Geim, A. K. & Falko, V. I. Generic miniband structure of graphene on a hexagonal substrate. *Phys. Rev. B* **87**, 245408, doi:10.1103/PhysRevB.87.245408 (2013).

29 Lee, M. *et al.* Ballistic miniband conduction in a graphene superlattice. *Science* **353**, 1526-1529, doi:10.1126/science.aaf1095 (2016).

30 Kumar, R. K. *et al.* High-order fractal states in graphene superlattices. *Proc. Natl. Acad. Sci. U. S. A.* **115**, 5135-5139, doi:10.1073/pnas.1804572115 (2018).

31 Wallbank, J. R. *et al.* Excess resistivity in graphene superlattices caused by umklapp electron-electron scattering. *Nat. Phys.* **15**, 32-36, doi:10.1038/s41567-018-0278-6 (2019).

32 Pittenger, B. B., Erina, N. & Su, C. *Quantitative mechanical property mapping at the nanoscale with PeakForce QNM*, <http://www.bruker.com/fileadmin/user_upload/8-PDF-Docs/SurfaceAnalysis/AFM/ApplicationNotes/AN128-RevB0-Quantitative_Mechanical_Property_Mapping_at_the_Nanoscale_with_PeakForceQNM-AppNote.pdf> (2012).

Acknowledgements The authors acknowledge support from EU Graphene Flagship Project (contract CNECTICT-604391), European Research Council Synergy Grant Hetero2D, the Royal Society, EPSRC grants EP/S019367/1, EP/P026850/1 and EP/N010345/1, US Army Research Office (W911NF-16-1-0279), FLAG-ERA project TRANS2DTMD. S.V.M. was supported by RFBR (17-02-01129a). J.Y. and A.M. acknowledge the support of EPSRC Early Career Fellowship EP/N007131/1.

Author contributions To be Added.

Competing interests none.

Data and material Availability: All presented data can be made available on request.

Supplementary

More examples of double alignment

Following from our analysis in the main text, we can extend the comparison between the calculated periodicities to the electronic transport characteristics of three more devices. Fig. S1 shows longitudinal resistance R_{xx}, hall resistance R_{xy} and their corresponding theoretical fittings of four samples; the device of the main text (Fig. S1a), and three others (Fig. S1b-d). All of these samples are encapsulated graphene heterostructures with perfect alignment in one side graphene-hBN contact surface. From the perfectly aligned moiré period, we can fit δ. The fitted parameters are shown in Supp. Table 1.

We compare R_{xx} and R_{xy} data to confirm the presence of secondary Dirac points, whose signature has both a peak in the R_{xx} data and a reversal of sign in R_{xy}. The coexistence of these features rules out other features in the moiré minibands (*5*).

	Figure label	Lattice mismatch	Second twist angle
Sample 1	**a**	1.64%	0.4^0
Sample 2	**b**	1.66%	0.44^0
Sample 3	**c**	1.69%	1.25^0
Sample 4	**d**	1.71%	0.25^0

Supplementary Table 1: δ and θ^{β} for each device. *Lattice mismatch, δ, and angle of the second hBN, θ^{β}, for each device in Fig. S1.*

Many R_{xx} peaks are observable with good agreement with the calculated periods. The amplitudes of the R_{xx} peaks for super-moiré are typically smaller than those of the moiré Dirac points. This is particularly pronounced on the hole side where the amplitude ratios, shown in Fig S4, result in a big difference between peaks of moiré and super-moiré. The R_{xx} features match with features in R_{xy}, indicating the presence of a new Dirac point. Many of the super-moiré features in R_{xy} do not reverse the sign entirely – however this may be explained as a result of the weakened amplitude of the super-moiré scattering process.

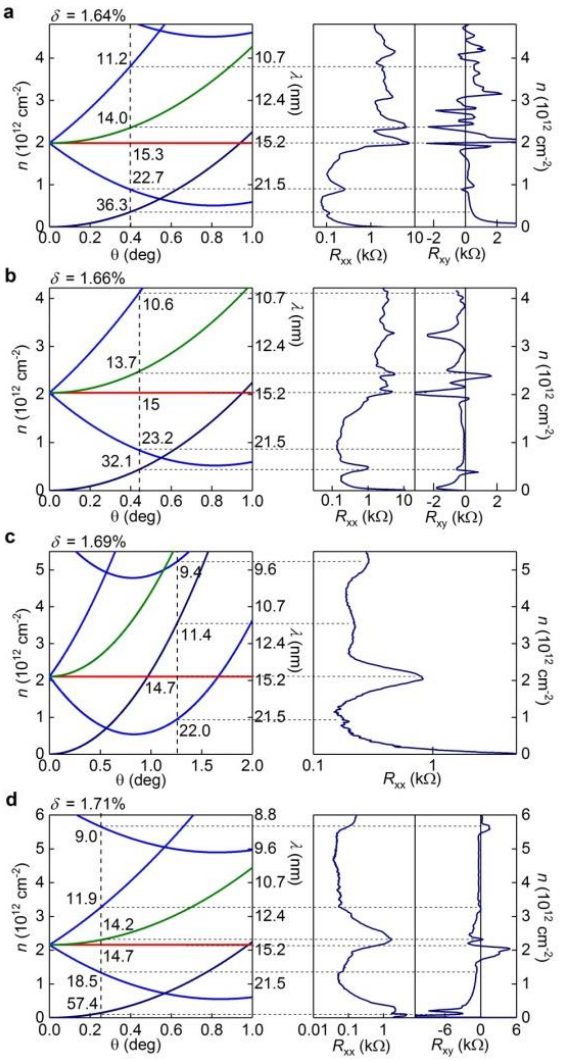

Supplementary Figure 1: Transport properties of doubly-aligned encapsulated graphene devices. a *shows the calculated dependence on* θ^{β} *of the moiré and super-moiré periodicities. Dashed lines are a guide for the eye linking intersections with* $\theta^{\beta} =$ 0.4 *to the* R_{xx} *and* R_{xy} *data. This is a reproduction of Fig. 3b and 3c from the main text.* ***b*** *Same as* ***a*** *for device two,* $\theta^{\beta} = 0.44$ *.* ***c*** *same as* ***a*** *for device three,* $\theta^{\beta} = 1.25$ *.* ***d*** *same as* ***a*** *for device 4,* $\theta^{\beta} = 0.25$*.*

Different fundamental frequencies of Brown-Zak oscillations

Previous literature reported the Brown-Zak oscillations (BZO) as a robust method to study the periodic potential applied on the graphene, for which maxima in σ_{xx} occurs following $\frac{B}{B_F} = \frac{p}{q}$ where fundamental frequency $B_F = \frac{\phi_0}{S}, p, q$ are integers, S is the area of unit cell (*6*, *7*). Here we employ BZO to probe the unit cell resulting from moiré and super-moiré periodicities. The key point is to extract the different frequencies corresponding to different unit cells, and then calculate the periodicity by assuming it corresponds to a hexagonal area.

As reported in (*7*), with p, q increasing, the amplitude of BZO decays exponentially due to the smaller group velocity and larger super unit cell. Usually p = 1 is much more prominent than p = 2, 3... It is experimentally difficult to realise observations

of the p=1, q=1, oscillations in singly-aligned graphene on hBN since the fundamental frequency is ~24T. Further, the BZO would be more visible at high carrier densities, high T (up to 150K), and in an electron doped graphene. The increased observation of the BZO at high temperature is due to the smearing of the electronic energy distribution which removes the influence of quantum phenomenon (Landau quantization). The BZO survive because they are transport oscillations, rather than a quantum oscillation.

In our BZO maps (Fig.S2, FigS3), the oscillation corresponding to an aligned graphene-hBN moiré is clearest. It is unobservable at carrier densities around Main Dirac points (MDP). However, other frequencies start to appear around the carrier densities of their corresponding R_{xx} peaks. Also, many BZO may be distinguished more clearly at high densities on electron-doped side of the main Dirac point (n>4.5e12 cm^{-2}) where the landau fan from the various Dirac point is unobservable. In Fig. S2b, the oscillations of the second largest super-moiré start to appear around its R_{XX} peak 0.9e12cm^{-2} (Fig.S1.**a**). In this range, only one frequency occurs at small magnetic fields, so it can be easily extracted. Then, around n = 2.0e12 cm^{-2}, shown in Fig.S2.**c**, the frequency of perfectly aligned graphene-hBN moiré pattern becomes dominant. To distinguish other frequencies, higher n and higher B are both required. In Fig.S2.d, we neglect the two frequencies that have already been extracted in the small n. Another two frequencies are observed. In total four distinct periodicities are observable; 2 moirés, and 2 super-moirés.

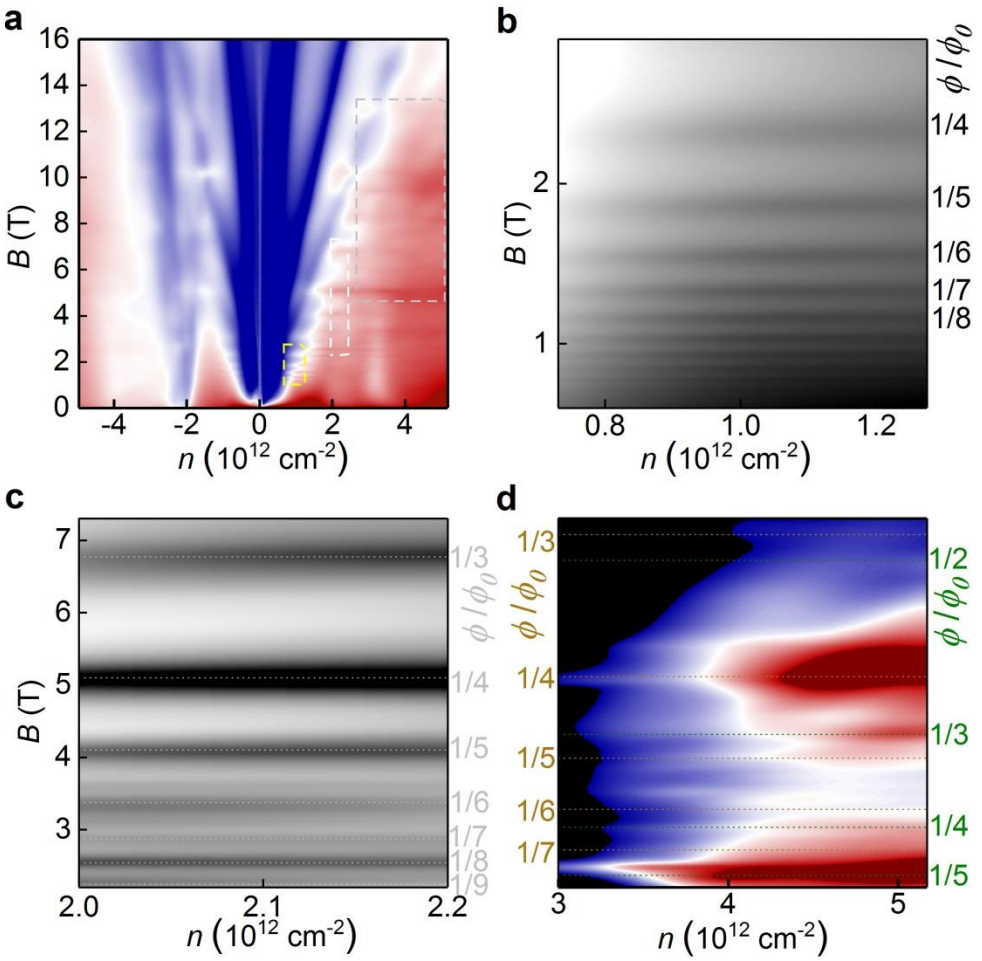

Fig.S2 Brown-Zak Oscillations in sample 1. *This sample is the same the main text.* ***a*** *σ_{xx} as a function of carrier concentration and magnetic field (Scale: blue to red 0.5 e^2/h to 70 e^2/h).* ***b***, ***c*** *and* ***d*** *are zoom-in of the region marked by the yellow, white, and grey dashed lines, respectively (scales: blue to red, 7 e^2/h to 37 e^2/h.).*

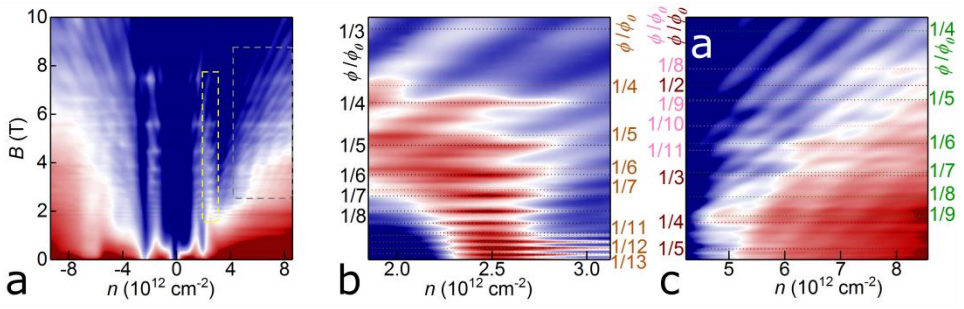

Fig.S3 Brown-Zak oscillations for sample 4. ***a*** *σ_{xx} map of carrier concentration and B-field of sample (scale: blue to red, 4 e^2/h to 150 e^2/h).* ***b*** *and* ***c*** *are zoom-in of the* ***a****, marked by the yellow and grey rectangles, respectively. (****b*** *scale: blue to red, 2.4 e^2/h to 30 e^2/h) (****c*** *scale: blue to red, 3.5 e^2/h to 50 e^2/h).* ***d*** *shows two magnetic field sweepings at carrier densities 6.0e12cm^{-2} and 8.5e12cm^{-2} with the same scale as* ***c****, dotted lines connecting the peaks of*

two sweepings to the maxima in the map. The Brown-Zak oscillations correspond to a moiré structures of different periodicities are marked by dotted lines of different colours. Black – 14.6nm (B_F=22.5T), violet – 14.2nm (B_F=23.8T), light pink – 8.9nm (B_F =60.5T), green – 11.9nm (B_F=33.5T), red – 18.4nm (B_F=14.1T). The periods are similar with those derived by R_{xx} and R_{xy}. All measurements are done at 35K.

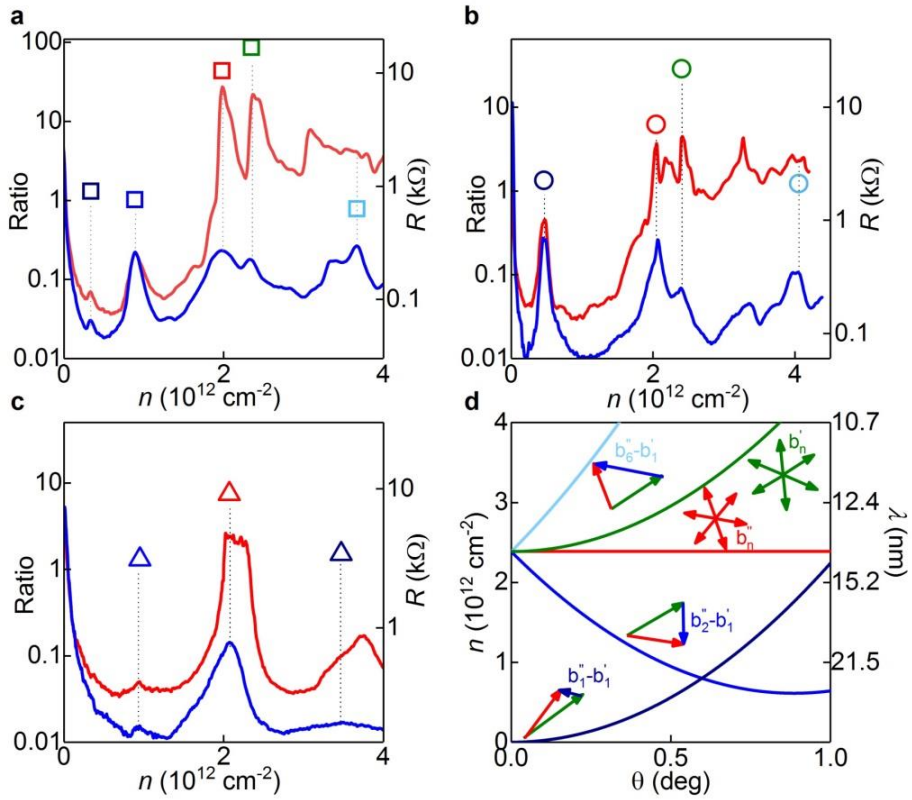

Fig.S4 electron-hole symmetry in super-moiré features. a, b *and* ***c,*** *scatter plots represent the ratios between hole-side peak amplitudes and their electron-side counterparts with dashed lines connecting their corresponding peaks (red – hole-side, blue – electron-side). Different shapes point to different samples,* ***a*** *(square) – sample 1,* ***b*** *(circle) – sample 2 and* ***c*** *(triangle) – sample 3, same as Main text Fig.4. Different colours point to different moiré vectors and super-moiré vectors, shown clearly in* ***d****.*

Gap Opening at the main Dirac point

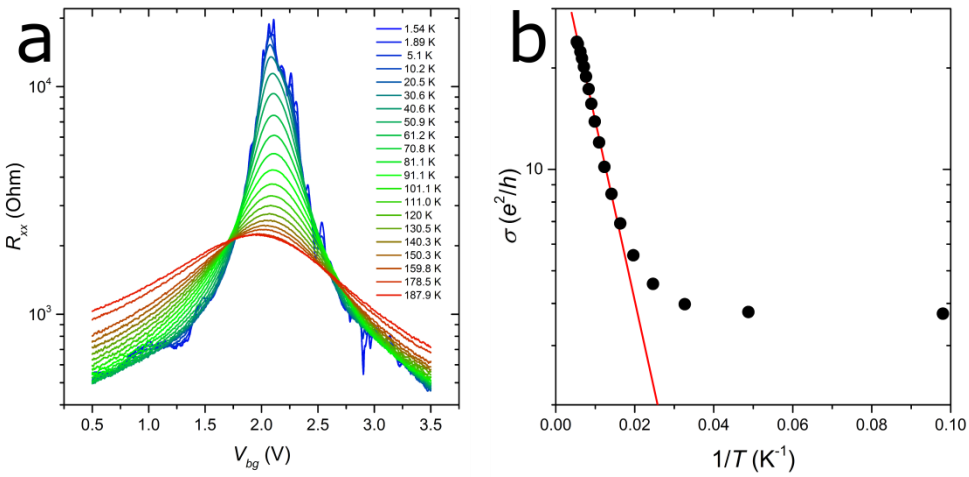

Fig.S5 Gap opening in one of our double aligned samples. a *R_{xx} vs back-gate voltage through the main Dirac point for various temperatures (1.54K-blue to 187.9K-red).* ***b*** *Temperature dependent conductivity at the main Dirac point. Experimental data (black dots) and exponential fit (red line). Fit gives a pseudo-gap of 21meV for data range of T>50K.*

Previously, a gap has been observed in the singly-aligned graphene-hBN superlattices of approximately 25 meV(*8, 9*). The origin of the gap is in the proximity induced sublattice symmetry breaking in graphene due to the hBN layer. Hunt el Al(*8*), showed that the gaps size is correlated with the periodicity of the moiré pattern. With that context, we have observed similar behaviour in our doubly-aligned samples.

With each sample we have measured the temperature dependent behaviour of the conductivity at the main Dirac point. In Fig.S5a we present the characteristic plot of R_{xx} against gate voltage through the main Dirac point, for many temperatures (1.54K – 187.9K). In Fig.S5b, the σ_{xx} at the Dirac point is plotted against temperature. The gap may then be extracted by fitting the data with to the Arrhenius law. In this case, we observed a 21meV gap. Which is consistent with singly-aligned graphene on hBN.

Atomic force microscopy of other double aligned samples

We have made and measured many doubly-aligned samples. Each sample shows a double moiré pattern in the AFM images (Fig. S6 a-d), principally confirmed by the presence of two sets of independent spots in the Fourier transformation (Fig. S6 e-h). In each case the encapsulation hBN layer is thin (<5 layers). We do not observe the moiré pattern when the hBN is thick (10s of nm). The double alignment is further confirmed by electronic transport data – yielding several moiré and super-moiré features.

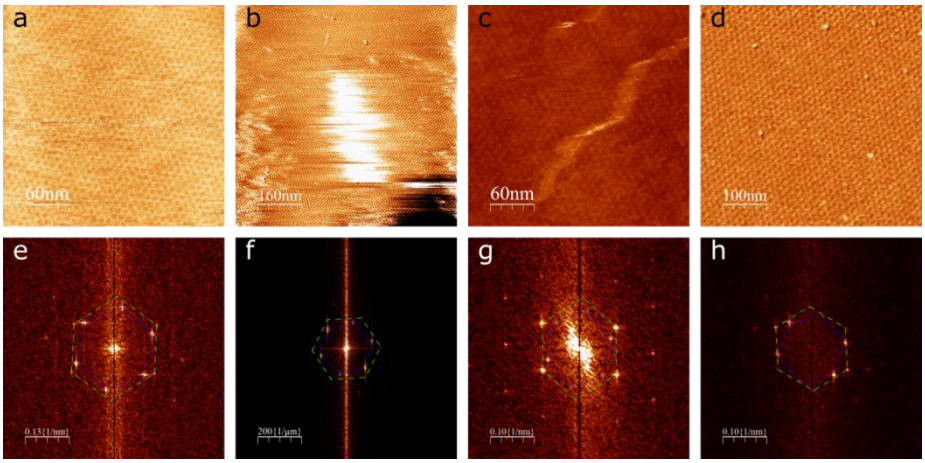

Fig.S6. Examples of double aligned samples. a, b, c, and d *AFM Young's Modulus images of super-moiré samples. In some cases, contamination is visible in the image.* ***e, f, g, and h*** *Fourier transformations of the images in* ***a, b, c, and d****, respectively. Each image shows two sets of hexagonal spots corresponding to distinct moiré periods.*

Uniformity in Heterostructures

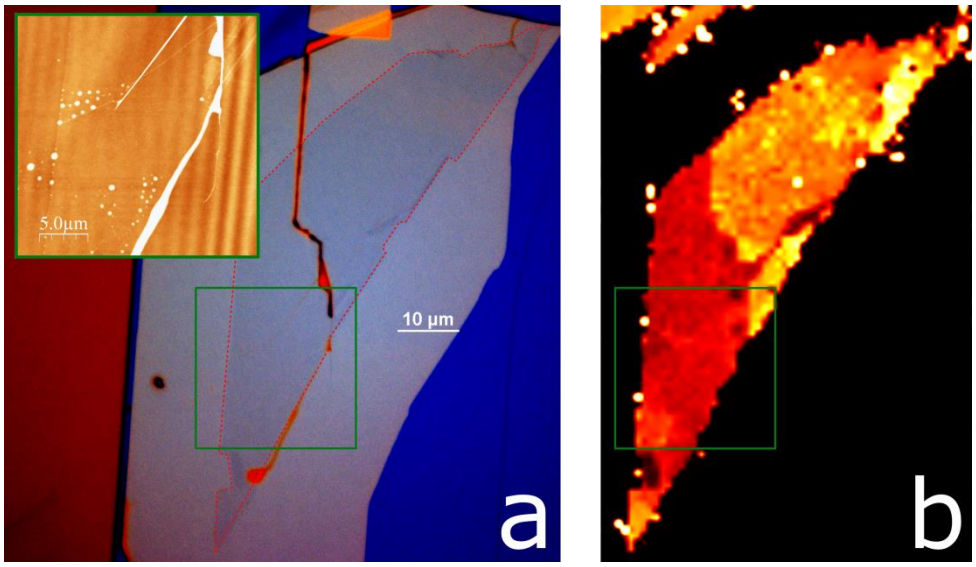

Fig.S7. Uniformity in doubly aligned heterostructures. a *Optical image (colour enhanced) of one of our hBN-graphene-hBN doubly aligned heterostructures before lithography. Dark blue highlights the bottom hBN layer, grey highlights overlap of the top hBN layer on the bottom hBN, and darker grey (outlined with dashed red) highlights the graphene region.* ***a-inset*** *AFM topography image of the area outlined by green in* ***a*** *and* ***b****. The vertical lines are an AFM artefact due to stray laser interference. Scale black to white is 2nm.* ***b*** *Map of the FWHM(2D) in the Raman spectrum. scale black to white is 15cm^{-1} to 100cm^{-1}. Each of these characterisation tools builds up an image of where there are distortions and deformations in the heterostructure. The lithography steps are then designed specifically to avoid these imperfections.*

Typical heterostructures produced from mechanically exfoliated flakes (method described in the next section) contain imperfections (creases, folds, contamination blisters, tears, etc.). However, to confirm the uniformity of our doubly-aligned samples we utilise optical images, AFM, and Raman spectroscopy mapping, to characterise the nature of our fully assembled heterostructures (Fig.S7) and design the devices to avoid such inhomogeneities. Fig.S7a shows the optical images of one of our doubly aligned samples. Clearly evident is a crack in the top-hBN layer induced during the fabrication process. Likewise, the crack is visible in the FWHM(2D) map (Fig.S7b). Further, in Fig.S7a-inset we can see examples of blisters and folds, which are most likely in the graphene layer. However, by only using the area of the heterostructures which is removed from these distortions we can guarantee uniform and homogenous devices.

Sample Fabrication

Further to the sample preparation described in the main text, in Fig S8, the general process is shown step-by-step. We use PPC (sometimes PMMA) spun on a thick PDMS membrane to facilitate moving and orientating the flake. This membrane is used to pick up the first hBN layer. The crystal may then be positioned and aligned to graphene (Fig. S8a) before the two are brought into contact (Fig. S8b). Removing the membrane in a precise way then lifts the graphene off from its substrate (Fig. S8c). Further, we can invert the membrane and perform various characterisation techniques on the half-assembled heterostructure (Fig S8d). The previous steps (Fig S8a-d) may be repeated multiple times to produce increasingly complex heterostructures. Finally, the stack of crystals is positioned (Fig S8e) and brought into contact with a final 'substrate' hBN (Fig S8f). The membrane is removed (Fig S8g) and all the crystals are left on a SiO_2 wafer (Fig S8h).

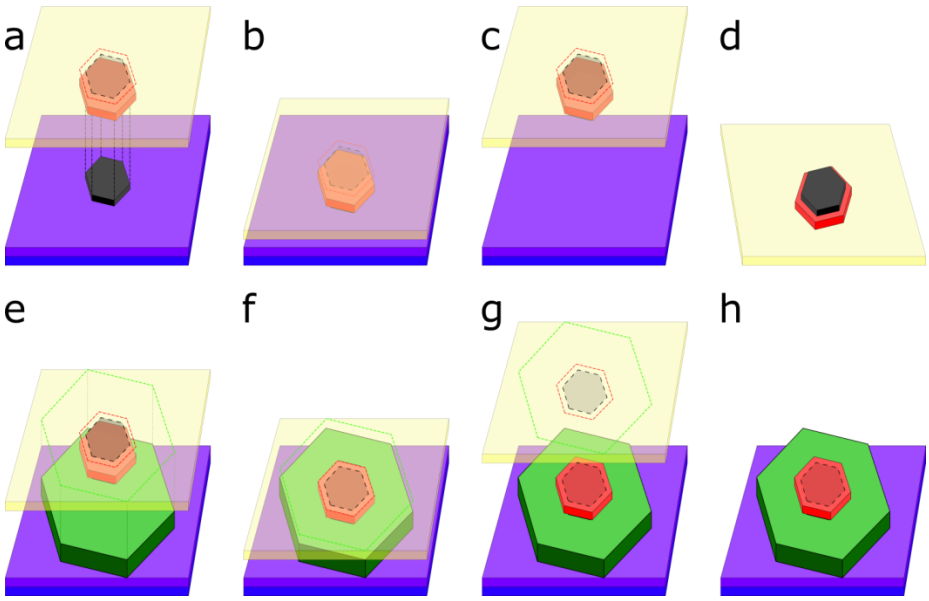

Fig.S8: illustration of a typical heterostructure fabrication process. a *A thin top-hBN (red) is aligned over a graphene flake (black).* ***b*** *The crystals are brought into contact.* ***c*** *The graphene and hBN are lifted away from the substrate.* ***d*** *The membrane is inverted and may be characterised by AFM and Raman spectroscopy.* ***e*** *once all the crystals are assembled on the membrane, the stack is aligned over a final substrate hBN layer (green).* ***f*** *The crystal are brought into contact.* ***g*** *The membrane is removed slowly.* ***h*** *All the crystals are left on*

the SiO_2/hBN substrate. The PPC/PDMS membrane is yellow, the Silicon is blue, and Silicon dioxide is purple.

Reference

1. D. A. Cosma, J. R. Wallbank, V. Cheianov, V. I. Fal'ko, Moiré pattern as a magnifying glass for strain and dislocations in van der Waals heterostructures. *Faraday Discussions* **173**, 137-143 (2014).
2. J. R. Wallbank, A. A. Patel, M. Mucha-Kruczynski, A. K. Geim, V. I. Falko, Generic miniband structure of graphene on a hexagonal substrate. *Physical Review B* **87**, 245408 (2013).
3. M. Mucha-Kruczyński, J. R. Wallbank, V. I. Fal'ko, Heterostructures of bilayer graphene and h-BN: Interplay between misalignment, interlayer asymmetry, and trigonal warping. *Physical Review B* **88**, 205418 (2013).
4. X. Chen *et al.*, Dirac edges of fractal magnetic minibands in graphene with hexagonal moir\'e superlattices. *Physical Review B* **89**, 075401 (2014).
5. L. A. Ponomarenko *et al.*, Cloning of Dirac fermions in graphene superlattices. *Nature* **497**, 594-597 (2013).
6. R. Krishna Kumar *et al.*, High-temperature quantum oscillations caused by recurring Bloch states in graphene superlattices. *Science* **357**, 181 (2017).
7. R. Krishna Kumar *et al.*, High-order fractal states in graphene superlattices. *Proceedings of the National Academy of Sciences* **115**, 5135 (2018).
8. B. Hunt *et al.*, Massive Dirac fermions and Hofstadter butterfly in a van der Waals heterostructure. *Science* **340**, 1427-1430 (2013).
9. C. R. Woods *et al.*, Commensurate-incommensurate transition in graphene on hexagonal boron nitride. *Nature Physics* **10**, 451-456 (2014).
10. P. Zeller, S. Günther, What are the possible moiré patterns of graphene on hexagonally packed surfaces? Universal solution for hexagonal coincidence lattices, derived by a geometric construction. *New Journal of Physics* **16**, 083028 (2014).
11. G. Argentero *et al.*, Unraveling the 3D Atomic Structure of a Suspended Graphene/hBN van der Waals Heterostructure. *Nano Letters* **17**, 1409-1416 (2017).

12. S. Plimpton, Fast Parallel Algorithms for Short-Range Molecular Dynamics. *Journal of Computational Physics* **117**, 1-19 (1995).
13. S. J. Plimpton, A. P. Thompson, Computational aspects of many-body potentials. *MRS Bulletin* **37**, 513-521 (2012).
14. S. Reich, J. Maultzsch, C. Thomsen, P. Ordejón, Tight-binding description of graphene. *Physical Review B* **66**, 035412 (2002).
15. T. M. G. Mohiuddin *et al.*, Uniaxial strain in graphene by Raman spectroscopy: G peak splitting, Gr\"uneisen parameters, and sample orientation. *Physical Review B* **79**, 205433 (2009).
16. T. Vincent *et al.*, Probing the nanoscale origin of strain and doping in graphene-hBN heterostructures. *2D Materials* **6**, 015022 (2018).

Chapter 7

Piezoelectricity in monolayer hexagonal boron nitride

The results are from a manuscript submitted to Nano Letters, 29th April 2019. NL-2019-017137.

Although monolayer hBN is theoretically considered to have piezoelectric properties, it has not been proved by experiment until this work. A local electric field is detected around bubbles and creases formed in hBN/graphene heterostructures, in accordance with the theoretical analysis. This effect appears in single layer hBN but vanishes in bilayer and bulk hBN forms. Electrostatic force microscopy (EFM) and AFM technique are used to investigate strain-induced electric field and the change of direction of creases between bubbles.

My contribution to the work includes: AFM studies of topography contrast of monolayer hBN on graphene and crease direction between bubbles. Also an additional experiment (supplementary 6), coating hBN/graphene heterostructures with polyelectrolyte nanoparticles to observe the alignment along the electric field.

Piezoelectricity in Monolayer Hexagonal Boron Nitride

Pablo Ares,[†,⊥] Tommaso Cea,[§] Matthew Holwill,[†,⊥] Yi Bo Wang,[†,⊥] Rafael Roldán,[‡] Francisco Guinea,*[,†,§] Daria V. Andreeva,[∥] Laura Fumagalli,*[,†,⊥] Konstantin S. Novoselov,*[,†,⊥] and Colin R. Woods[†,⊥]

[†]School of Physics & Astronomy, University of Manchester, Manchester M13 9PL, UK

[⊥]National Graphene Institute, University of Manchester, Manchester M13 9PL, UK

[§]Imdea Nanociencia, Faraday 9, 28049 Madrid, Spain

[‡]Instituto de Ciencia de Materiales de Madrid, Sor Juana Inés de la Cruz 3, 28049 Madrid, Spain

[∥]Department of Materials Science and Engineering, National University of Singapore, Singapore, 117575, Singapore

KEYWORDS: hexagonal boron nitride, 2D materials, piezoelectricity, electrostatic force microscopy.

Two-dimensional (2D) hexagonal boron nitride (hBN) is a wide-bandgap van der Waals crystal with remarkable properties, including exceptional strength, large oxidation resistance at high temperatures and single-photon emission. Furthermore, in recent years hBN crystals have become the material of choice for encapsulating other 2D crystals in a variety of technological applications, from optoelectronic and tunnelling devices to composites. Monolayer hBN, which has no centre of symmetry, has been predicted to exhibit piezoelectric properties, yet experimental evidence is lacking. Here, by using electrostatic force microscopy, we observed this effect as a strain-induced change in the local electric field around bubbles and creases, in agreement with our theoretical analysis. No piezoelectricity was found in bilayer and bulk hBN, where the centre of symmetry is restored. These results add piezoelectricity to the known properties of monolayer hBN, which makes it a desirable candidate for novel electromechanical and stretchable optoelectronic devices, and pave a way to control the local electric field and carrier concentration in van der Waals heterostructures via strain.

Main Text:

Piezoelectricity is an important property of non-centrosymmetric crystals that allows conversion of mechanical strain into electric field, and vice versa.[1] Recently, two-dimensional (2D) crystals have shown to be a unique platform to investigate and exploit such property for many reasons. First, they have the ability to sustain large strain (up to 10%) before rupture or plastic deformation,[2,3] while this is challenging to achieve in 3D crystals. Second, many crystals are found to be piezoelectric only when reduced to two-dimensionality. This is the case of semiconducting transition metal dichalcogenide crystals, in which inversion symmetry is broken only in their 2D forms, as recently observed in single-layer MoS_2.[4,5] Furthermore, 2D crystals are likely to show areas of non-uniform strain near corrugations or bubbles that naturally form on substrates.[6] In such areas, strained-induced local charge densities, ρ, are expected to appear owing to the local variation in polarization, $\boldsymbol{P}$, since $\rho(\boldsymbol{r}) = -\boldsymbol{\nabla} \cdot \boldsymbol{P}(\boldsymbol{r})$.[7]

2D hexagonal boron nitride (hBN) is a van der Waals crystal with remarkable properties[2,8-11] and is an essential component of many new 2D technologies.[12] Recently, monolayer hBN has also been theoretically predicted to be piezoelectric.[7,13] This is because it has a honeycomb lattice structure similarly as graphene, but the presence of different elements in the two sublattices of its unit cell makes it non-centrosymmetric. On the other hand, its bilayer and bulk counterparts present inversion symmetry and, therefore, no piezoelectricity is expected.[7,13] Here we report experimental evidence of piezoelectricity in monolayer hBN by directly visualizing the strained-induced electric field in hBN/graphene heterostructures using electrostatic force microscopy (EFM)[14,15] (Figure 1a). EFM images of monolayer hBN on graphene show enhanced electric contrast in correspondence of non-homogeneous strain areas. Such contrast vanishes on bilayer hBN. We support our experimental findings with theoretical calculations, solving the elasticity equations in a honeycomb lattice for deformations that mimic the observed bubbles and creases (Figure 1b).

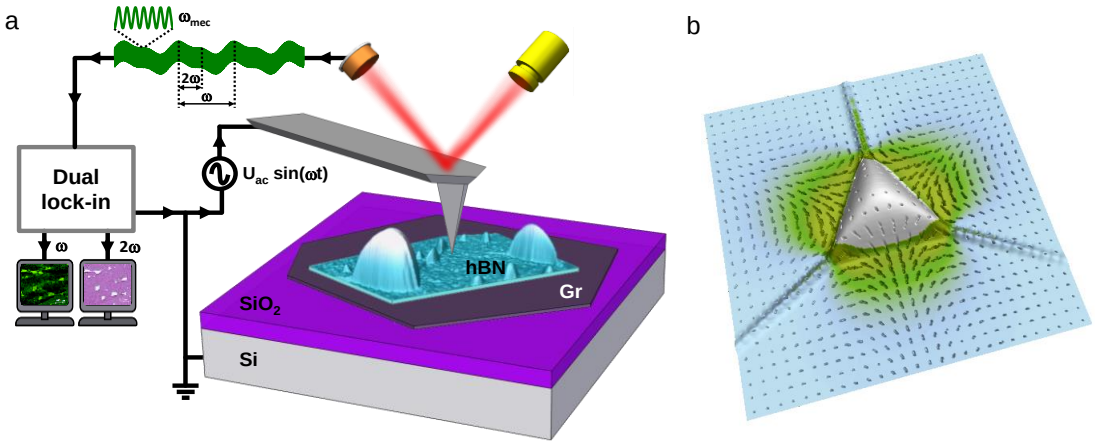

Figure 1. Schematic illustration of the experimental setup and the piezoelectric field in monolayer hBN around bubbles. (a) EFM on hBN/graphene heterostructures on SiO_2/Si substrates. An ac voltage bias of frequency ω is applied between the AFM tip and the Si substrate. Simultaneous electric and dielectric images are measured at the first (ω) and second (2ω) harmonic, respectively, of the cantilever frequency shift, $\Delta\omega_{mec}$. (b) Example of calculated strain-induced polarization and electric field distribution for a triangular bubble in monolayer hBN.

EFM is a non-contact scanning probe technique that maps the local electrostatic interaction between the tip and the sample.[14,15] We acquired EFM images by applying an ac voltage bias at frequency ω between the tip and the sample. We measured the frequency shift, $\Delta\omega_{mec}$, of the cantilever at its mechanical resonance, detecting the electric response at the first and second harmonics, ω and 2ω, respectively[16-18] (Figure 1a) (see Methods). We thus obtained two simultaneous EFM images: the electric image at ω, which is proportional to the electric field on the surface,[16,18,19] and the dielectric image at 2ω, which depends only on the tip-sample capacitive interaction and the dielectric properties of the sample[16,17] (see Methods and Supporting Note 1 in the Supporting Information, SI). The latter was required here to investigate the impact of local capacitive/dielectric variations on the electric image. Unlike conventional EFM that uses a double-pass approach, we recorded simultaneous topography and EFM images on a single pass to minimize the tip-surface distance and, therefore, increase the resolution of the EFM images.

We applied EFM to monolayer, bilayer and multilayer hBN on graphene on SiO_2/Si substrates, as shown in Figure 1a. We fabricated the samples using the standard dry transfer technique,[20] which is ubiquitous to the production of high-quality van der Waals heterostructures (see Methods). We studied hBN on graphene instead of hBN directly on SiO_2 substrates because graphene promotes the formation of non-uniform strain areas. Such areas are observed around creases and bubbles filled with hydrocarbons that spontaneously appear in hBN/graphene heterostructures.[6] Furthermore, it is beneficial here to use graphene as bottom layer because it acts as a charge-sink for localized charges trapped at the substrate interface, facilitating the visualization of strained-induced electric fields in the overlying hBN layer.

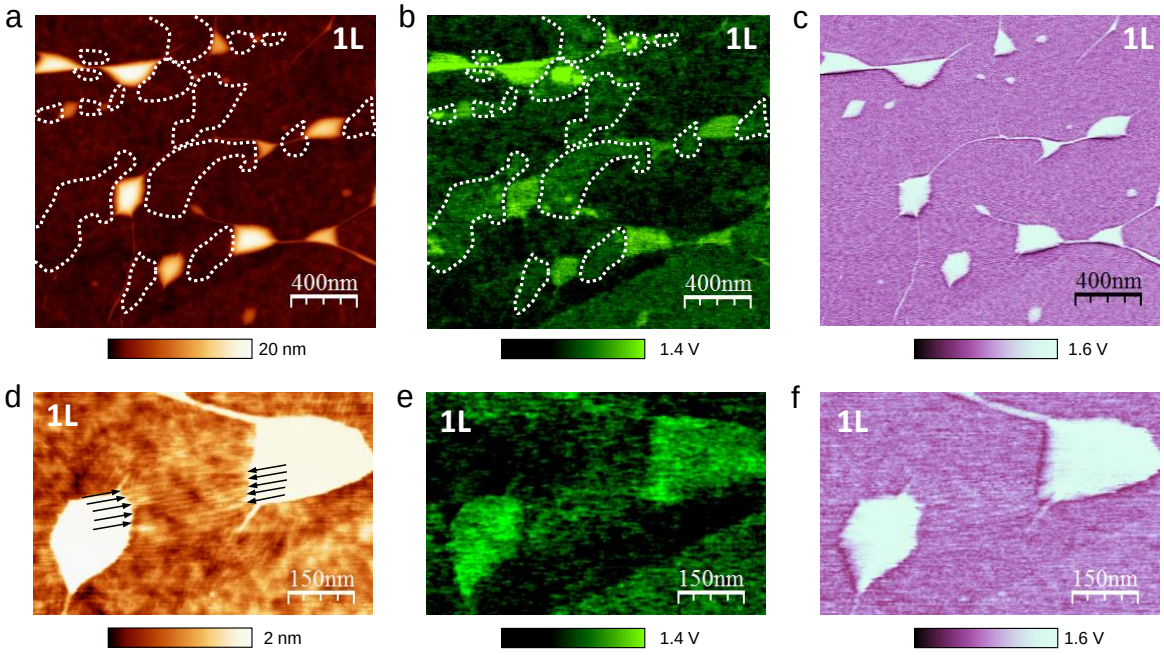

Figure 2. AFM topography and EFM images of monolayer hBN on graphene. (a) Topography of monolayer hBN on graphene. (b) Corresponding EFM electric image, showing enhanced contrast around and between bubbles. Dotted lines are a guide to the eye. (c) Corresponding EFM dielectric image, showing no contrast around or between bubbles. (d) Zoom in the topography (a), showing atomically thin creases between two bubbles, and corresponding (e) electric and (f) dielectric images. Colour scale in (d) was adjusted to show the atomically thin creases, which are marked by black arrows.

Figure 2a shows a representative topography image of our monolayer hBN on graphene, where several bubbles and creases can be seen. The corresponding EFM electric image

in Figure 2b shows high contrast over the bubbles due to the presence of molecules inside. However, it also shows high intensity in many areas around the bubbles and creases, spanning hundreds of nanometres and connecting various bubbles (marked by white dashed contours in Figure 2b). A different behaviour can be seen in the corresponding dielectric image at 2ω in Figure 2c. This shows again the characteristic enhanced contrast over the bubbles caused by the material trapped inside, but no contrast around or between them. Images obtained in other locations confirm these observations (see Figure S1 in the SI). The dielectric image allows us to rule out that the bright regions around and between the bubbles in Figure 2b reflect a local change in the surface dielectric properties or in the capacitive interaction. Furthermore, we did not observe any bright feature in the electric image in the absence of bubbles and creases (Figure S2). This implies that the electric field variations detected around them do not originate from molecules that might be trapped at the hBN/graphene or graphene/SiO_2 interface. We therefore conclude that such electric field variations are the consequence of the hBN being strongly strained in these areas. Close-up images confirmed this conclusion. Figure 2e shows a bright area between two bubbles. The corresponding topography image (Figure 2d) reveals the presence of atomically thin creases (height < 3 Å) connecting the bubbles, which are associated with strain concentration and release around the bubbles.[6,21] The electric contrast that we obtained in these areas is comparable to the output voltage generated in monolayer MoS_2 when subjected to similar strains,[4] in agreement with the expected piezoelectric response of monolayer hBN, as monolayer hBN and MoS_2 have similar piezoelectric constants.[7] We thus conclude that the bright areas detected in the electric images around the bubbles and creases are consequences of the piezoelectric properties of the monolayer hBN.

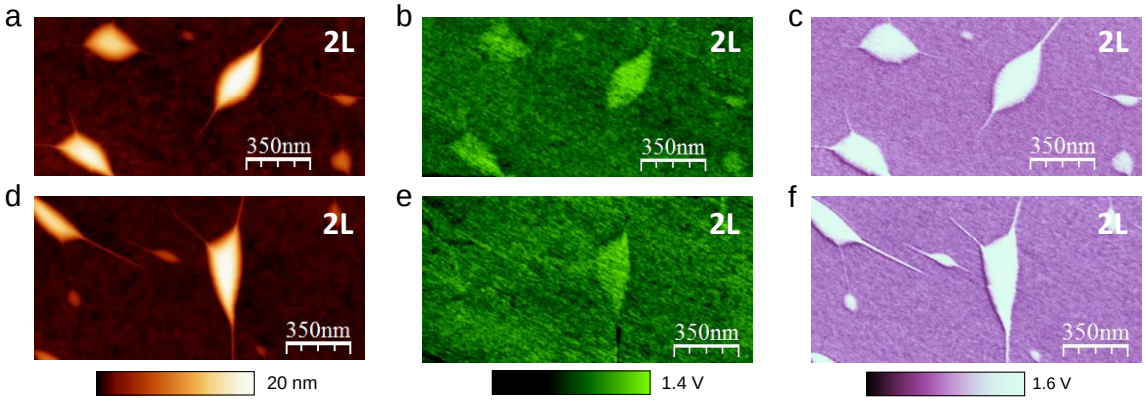

Figure 3. AFM topography and EFM images of bilayer hBN on graphene. (a,d) Topography and corresponding (b,e) electric and (c,f) dielectric images of bilayer hBN. Contrary to the case of the monolayer (Figure 2), no bright areas were detected around or between bubbles in the electric image.

We then investigated the case of the bilayer hBN, in which no piezoelectricity is expected. Figure 3 shows representative topography and EFM images of bilayer hBN on graphene on a SiO_2/Si substrate, taken under the same experimental conditions as Figure 2. The bilayer form bubbles of similar size and shape as those that we found in the monolayer (Figure 3a,d). The electric images (Figure 3b,e) show again high contrast over the bubbles, as expected. However, we found no noticeable features around or between them, in contrast with our observations on the monolayer. We consistently found this behaviour for all the bubbles on the bilayer and multilayers (Figure S3). These observations agree with the predicted absence of piezoelectricity in bilayer hBN.

To support our experimental data, we theoretically calculated the piezoelectric behaviour of monolayer hBN in the presence of bubbles and creases that mimic those observed experimentally. Given the height profile of the bubbles, we solved the discretized elasticity equations for the membrane with a honeycomb lattice (see Methods and Supporting Notes 2 and 3), thus providing the strain tensor u_{jk} and hence the piezoelectric induced polarization $P_i(\boldsymbol{r}) = \sum_{jk} \gamma_{ijk} u_{jk}(\boldsymbol{r})$, being γ_{ijk} the 3-rd rank piezoelectric tensor. For 2D crystals with D_{3h} symmetry lying in the xy-plane (we choose x-direction parallel to the zigzag edge, and y-direction parallel to the armchair edge), the only non-zero independent coefficient is[7] $\gamma \equiv \gamma_{yyy} = -\gamma_{yxx} = -\gamma_{xyx} = -\gamma_{xxy}$. For the case of hBN and related 2D crystals with hexagonal symmetry, the polarization can be written as[7,22] $\boldsymbol{P}(\boldsymbol{r}) = \gamma \boldsymbol{\mathcal{A}}(\boldsymbol{r}) \times \hat{\boldsymbol{z}}$, where $\boldsymbol{\mathcal{A}}(\boldsymbol{r}) = \big(u_{xx}(\boldsymbol{r}) - u_{yy}(\boldsymbol{r})\big)\hat{\boldsymbol{x}} - 2u_{xy}(\boldsymbol{r})\hat{\boldsymbol{y}}$ has the form of the gauge field that appears in strained graphene.[23] We used the modern theory of polarization that exploits the geometrical properties of the Bloch wave-functions to obtain the electronic polarization,[24] a method that has been applied to non-centrosymmetric hexagonal nanotubes[25] and 2D crystals.[7,22] In particular, it has been shown that it is possible to express the piezoelectric coefficient in terms of the valley Chern number.[7] For the case of interest here, the piezoelectric coefficient of hBN takes the simple form $\gamma = \eta \frac{e}{4\pi a_0} \mathcal{C}_{\text{valley}} \approx 2.91 \times 10^{-10}$ Cm^{-1}, where

$\eta \approx 3.3$ is the electron-phonon coupling in hBN,[22] $a_0 = 1.44$ Å is the interatomic distance, e is the elementary charge, and $\mathcal{C}_{\text{valley}} = \sum_\tau \tau \mathcal{C}_\tau = \text{sign}(\Delta)$ is the valley Chern number, where τ is the valley index, $\Delta \approx 5.97$ eV is the hBN bandgap, and $\mathcal{C}_\tau = \tau\, \text{sign}(\Delta)/2$. We refer to Methods for details in the numerical simulations steps. From these calculations we obtain the spatial distribution of electronic polarization $\boldsymbol{P}(\boldsymbol{r})$, the piezoelectric charge density $\rho(\boldsymbol{r})$ and the energy density generated by the piezoelectric effect.

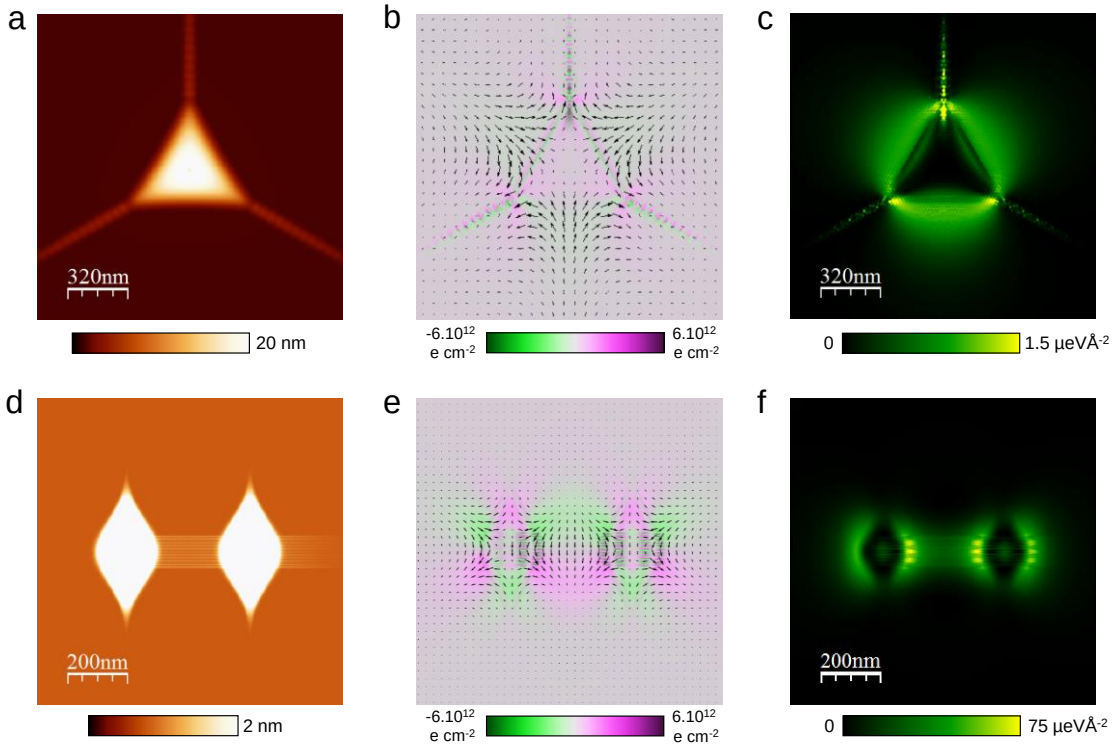

Figure 4. Simulated piezoelectric-induced polarization in bubbles on monolayer hBN. (a) Simulated topography image of a triangular bubble and corresponding calculated (b) polarization (vector field) and charge distribution (colormap) and (c) electric field energy density. (d) Simulated topography of two elliptical bubbles with atomically thin creases in between and corresponding (e) polarization (vector field) and charge distribution (colormap) and (f) electric field energy density . Colour scale in (d) was adjusted to show the creases.

Figure 4a-c shows calculated images for a triangular bubble with one-dimensional creases at the vertices (Figure 4a) similar to the ones experimentally observed. Simulations for bubbles with different shapes are reported in Figures S6 and S8. The shape of the bubble (Figure 4a) is given by the equilibrium configuration of a material

trapped between a flat substrate and a 2D crystal attracted by van der Waals forces, as described in ref.[6]. Figures 4b,c show the corresponding calculated polarization charge and electric field energy density images. Our simulations predict high contrast in energy density in the strained areas around the bubbles in correspondence of piezoelectric charge densities, in qualitative agreement with our observations. This can be understood as the EFM signal detects the electric field variations that arise from local charge densities.[16,18] We analysed the triangular bubble at different orientations with respect to the crystallographic axes (Figure S7). We found that the energy density distribution does not depend on the bubble orientation, which is also consistent with our experimental observations. However, the bright areas that we experimentally observed tend to extend over larger regions that connect different bubbles. This can be explained by the presence of atomically thin creases in these regions, which generate additional strain. To support this conclusion, we analysed the case of bubbles connected by such ultrathin creases. Figure 4d-f shows simulations for two elliptical bubbles with atomically thin creases in between, which mimic the ones observed in Figure 2d (see also Figure S9). The calculated electric field energy density image (Figure 4f) clearly exhibits enhanced contrast that extends between the two bubbles and matches the bright contrast observed in the EFM image (Figure 2e) (see also Figure S10).

To further confirm the piezoelectricity of the monolayer, we made an additional experiment using a decoration technique. We deposited polyelectrolyte nanoparticles in solution onto our hBN/graphene samples. These nanoparticles tend to align with the electric field, similarly as iron filings around a magnet (see Supporting Note 6). Figure S11 shows representative topography images that we obtained. We found that the nanoparticles align with the field in monolayer hBN, while this alignment is absent in bulk hBN. The nanoparticles distribution in monolayer hBN, detected at distances up to a few hundreds of nanometres from the bubble, agrees with the calculated electric field distribution that originates from the strain around the bubbles.

It is useful to estimate the induced polarisation and the electric field energy density due to the anisotropic strain gradient in our hBN membranes. Although they vary strongly, they can reach relatively high levels in some regions, ~ 10^{12} cm^{-2} and ~ 10^{-6} $eVÅ^{-2}$, respectively, comparable to the carrier concentration in doped graphene[26] and to the energy density in capacitors used in microelectronic circuits[27] if scaled to two-

dimensionality. Such strain-induced electric fields can provide a significant scattering mechanism if monolayer hBN is used as encapsulation layer on top of graphene. At the same time, one can envisage that special distribution of the carrier density in graphene can be altered via strain in such monolayer encapsulation layer.

In summary, the experimental images and theoretical simulations that we have presented here confirm the generation of piezoelectric fields in highly strained monolayer hBN. We visualized the electric fields generated by strained regions around bubbles and creases in the monolayer, while they are absent in the bilayer and bulk hBN, in agreement with the theory. The piezoelectricity of single-layer hBN opens the door to its combination with other 2D materials for the development of devices with novel functionalities and self-powering potential. These results are also important as they show a way to detect piezoelectricity in other 2D crystals on the nanoscale.

Methods:

Samples preparation. Samples were fabricated using the standard dry transfer technique. Briefly, monolayer hBN was mechanically exfoliated and identified on a double-polymer layer of Polymethylglutarimide (PMGI) and Poly(methyl methacrylate) (PMMA). The PMGI layer was developed from beneath the PMMA layer to create a free-standing and easily-manipulated membrane with the crystal on top. The membrane was then inverted and positioned above graphene using a set of micromanipulation stages – with accuracy better than 5 μm. The crystals were then brought into contact. The PMMA was removed by simply peeling back the membrane, meaning no solvent come into contact with either crystal to preserve the cleanliness of the top surface.

AFM and EFM imaging. We acquired simultaneous AFM and EFM images using a Nanotec Electronica AFM (see Supporting Note 1 for details). We measured the EFM force gradient at the first and second harmonic by using a phase-lock loop and a multi-frequency lock-in amplifier (Zurich Instruments). We used n-doped silicon probes (Nanosensors PPP-XYNCSTR, mechanical resonance frequency ~ 137 kHz and spring constant ~ 5.3 Nm^{-1}), calibrated using the Sader's method.[28] Doped silicon tips have the advantage of a tip radius of only a few nanometres, one order of magnitude smaller than the typical radius of metal-coated probes, thus increasing the lateral resolution of both

topography and EFM images. Furthermore, unlike metal-coated probes, n-doped silicon probes suffer no substantial tip modifications during imaging and, therefore, ensure stable measurement conditions.[29] We oscillated the cantilever in resonance with free amplitudes below 20 nm and setpoints imposing minimum amplitude reduction. We carried out EFM imaging in the so-called frequency modulation mode,[30-32] electrically exciting the cantilever with an ac voltage of amplitude 4 V and frequency 1.8 kHz. We acquired and processed the data using WSxM software.[33,34]

Theoretical calculations. For a given strain profile, the induced charge density is obtained from the local variation of the polarization as $\rho(\boldsymbol{r}) = e\, n(\boldsymbol{r}) = -\boldsymbol{\nabla} \cdot \boldsymbol{P}(\boldsymbol{r}) = -\gamma \hat{\boldsymbol{z}} \cdot [\boldsymbol{\nabla} \times \boldsymbol{\mathcal{A}}(\boldsymbol{r})]$. The numerical calculation involves the following steps (see Supporting Notes 2 - 4 for details): (i) The equilibrium configuration of a deformed single-layer hBN membrane (61200 or 242000 atoms, depending on the cases, clamped boundary conditions) is obtained from the numerical solution of the discretized elasticity equations for a given shape (*e.g.* circular, triangular or elliptical bubbles). (ii) The solution gives the strain fields $u_{ij}(\boldsymbol{r})$ generated in the crystal that minimize the energy, which enters in the vector potential $\boldsymbol{\mathcal{A}}(\boldsymbol{r})$ and which is used to calculate the spatial distribution of electronic polarization $\boldsymbol{P}(\boldsymbol{r})$, piezoelectric charge density $\rho(\boldsymbol{r})$, the energy density generated by the piezoelectric effect $u_E(\boldsymbol{r}) = |\boldsymbol{P}(\boldsymbol{r})|^2/(2\varepsilon_{2d})$, where ε_{2d} is the dielectric constant of the hBN film. (iii) The first derivative of the energy density with respect to the out of plane direction gives the electrostatic force distribution acting normal to the surface.[35,36]

ASSOCIATED CONTENT

Supporting Information. The following files are available free of charge.
Additional AFM and EFM images, theoretical calculations, numerical results, comparison between simulated and experimental images, polyelectrolyte nanoparticles deposition (PDF).

AUTHOR INFORMATION

Corresponding Author

* E-mail: francisco.guinea@manchester.ac.uk, laura.fumagalli@manchester.ac.uk, Konstantin.Novoselov@manchester.ac.uk

Author Contributions

The manuscript was written through contributions of all authors. All authors have given approval to the final version of the manuscript.

Funding Sources

EU Graphene Flagship Program, European Research Council, Royal Society, Engineering and Physical Research Council, US Army Research Office, EU Research and Innovation Program.

Notes

The authors declare no competing financial interest.

ACKNOWLEDGMENT

The authors acknowledge support from EU Graphene Flagship Program (contract CNECTICT-604391), European Research Council Synergy Grant Hetero2D, the Royal Society, Engineering and Physical Research Council (UK, grant number EP/N010345/1), US Army Research Office (W911NF-16-1-0279). P. A. and L. F. received funding from the EU Research and Innovation Program under the Marie Sklodowska-Curie grant agreement No 793394.

Reference

1. Brown, C.; Kell, R.; Taylor, R.; Thomas, L. Piezoelectric materials, a review of progress. *IRE Trans. Compon. Parts* **1962**, *9*, 193–211.

2. Falin, A.; Cai, Q. R.; Santos, E. J. G.; Scullion, D.; Qian, D.; Zhang, R.; Yang, Z.; Huang, S. M.; Watanabe, K.; Taniguchi, T.; Barnett, M. R.; Chen, Y.; Ruoff, R. S.; Li, L. H. Mechanical properties of atomically thin boron nitride and the role of interlayer interactions. *Nat. Commun.* **2017**, *8*, 15815.

3. Lee, C.; Wei, X. D.; Kysar, J. W.; Hone, J. Measurement of the elastic properties and intrinsic strength of monolayer graphene. *Science* **2008**, *321*, 385-388.
4. Wu, W. Z.; Wang, L.; Li, Y. L.; Zhang, F.; Lin, L.; Niu, S. M.; Chenet, D.; Zhang, X.; Hao, Y. F.; Heinz, T. F.; Hone, J.; Wang, Z. L. Piezoelectricity of single-atomic-layer MoS2 for energy conversion and piezotronics. *Nature* **2014**, *514*, 470-474.
5. Zhu, H. Y.; Wang, Y.; Xiao, J.; Liu, M.; Xiong, S. M.; Wong, Z. J.; Ye, Z. L.; Ye, Y.; Yin, X. B.; Zhang, X. Observation of piezoelectricity in free-standing monolayer MoS2. *Nat. Nanotechnol.* **2015**, *10*, 151-155.
6. Khestanova, E.; Guinea, F.; Fumagalli, L.; Geim, A. K.; Grigorieva, I. V. Universal shape and pressure inside bubbles appearing in van der Waals heterostructures. *Nat. Commun.* **2016**, *7*, 12587.
7. Rostami, H.; Guinea, F.; Polini, M.; Roldán, R. Piezoelectricity and valley chern number in inhomogeneous hexagonal 2D crystals. *NPJ 2D Mater. Appl.* **2018**, *2*, 15.
8. Li, L. H.; Cervenka, J.; Watanabe, K.; Taniguchi, T.; Chen, Y. Strong Oxidation Resistance of Atomically Thin Boron Nitride Nanosheets. *ACS Nano* **2014**, *8*, 1457-1462.
9. Li, L. H.; Chen, Y. Atomically Thin Boron Nitride: Unique Properties and Applications. *Adv. Funct. Mater.* **2016**, *26*, 2594-2608.
10. Li, L. H.; Chen, Y.; Cheng, B. M.; Lin, M. Y.; Chou, S. L.; Peng, Y. C. Photoluminescence of boron nitride nanosheets exfoliated by ball milling. *Appl. Phys. Lett.* **2012**, *100*, 261108.
11. Tran, T. T.; Bray, K.; Ford, M. J.; Toth, M.; Aharonovich, I. Quantum emission from hexagonal boron nitride monolayers. *Nat. Nanotechnol.* **2016**, *11*, 37-41.
12. Dean, C. R.; Young, A. F.; Meric, I.; Lee, C.; Wang, L.; Sorgenfrei, S.; Watanabe, K.; Taniguchi, T.; Kim, P.; Shepard, K. L.; Hone, J. Boron nitride substrates for high-quality graphene electronics. *Nat. Nanotechnol.* **2010**, *5*, 722-726.
13. Duerloo, K. A. N.; Ong, M. T.; Reed, E. J. Intrinsic Piezoelectricity in Two-Dimensional Materials. *J. Phys. Chem. Lett.* **2012**, *3*, 2871-2876.
14. Martin, Y.; Abraham, D. W.; Wickramasinghe, H. K. High-Resolution Capacitance Measurement and Potentiometry by Force Microscopy. *Appl. Phys. Lett.* **1988**, *52*, 1103-1105.
15. Stern, J. E.; Terris, B. D.; Mamin, H. J.; Rugar, D. Deposition and Imaging of Localized Charge on Insulator Surfaces Using a Force Microscope. *Appl. Phys. Lett.* **1988**, *53*, 2717-2719.

16. Cherniavskaya, O.; Chen, L. W.; Weng, V.; Yuditsky, L.; Brus, L. E. Quantitative noncontact electrostatic force Imaging of nanocrystal polarizability. *J. Phys. Chem. B* **2003**, *107*, 1525-1531.

17. Fumagalli, L.; Esteban-Ferrer, D.; Cuervo, A.; Carrascosa, J. L.; Gomila, G. Label-free identification of single dielectric nanoparticles and viruses with ultraweak polarization forces. *Nat. Mater.* **2012**, *11*, 808-816.

18. Terris, B. D.; Stern, J. E.; Rugar, D.; Mamin, H. J. Contact Electrification Using Force Microscopy. *Phys. Rev. Lett.* **1989**, *63*, 2669-2672.

19. Collins, L.; Kilpatrick, J. I.; Weber, S. A. L.; Tselev, A.; Vlassiouk, I. V.; Ivanov, I. N.; Jesse, S.; Kalinin, S. V.; Rodriguez, B. J. Open loop Kelvin probe force microscopy with single and multi-frequency excitation. *Nanotechnology* **2013**, *24*, 475702.

20. Kretinin, A. V.; Cao, Y.; Tu, J. S.; Yu, G. L.; Jalil, R.; Novoselov, K. S.; Haigh, S. J.; Gholinia, A.; Mishchenko, A.; Lozada, M.; Georgiou, T.; Woods, C. R.; Withers, F.; Blake, P.; Eda, G.; Wirsig, A.; Hucho, C.; Watanabe, K.; Taniguchi, T.; Geim, A. K.; Gorbachev, R. V. Electronic Properties of Graphene Encapsulated with Different Two-Dimensional Atomic Crystals. *Nano Lett.* **2014**, *14*, 3270-3276.

21. Bowden, N.; Brittain, S.; Evans, A. G.; Hutchinson, J. W.; Whitesides, G. M. Spontaneous formation of ordered structures in thin films of metals supported on an elastomeric polymer. *Nature* **1998**, *393*, 146-149.

22. Droth, M.; Burkard, G.; Pereira, V. M. Piezoelectricity in planar boron nitride via a geometric phase. *Phys. Rev. B* **2016**, *94*, 075404.

23. Guinea, F.; Katsnelson, M. I.; Geim, A. K. Energy gaps and a zero-field quantum Hall effect in graphene by strain engineering. *Nat. Phys.* **2010**, *6*, 30-33.

24. Resta, R. Macroscopic polarization in crystalline dielectrics: the geometric phase approach. *Rev. Mod. Phys.* **1994**, *66*, 899-915.

25. Mele, E. J.; Kral, P. Electric polarization of heteropolar nanotubes as a geometric phase. *Phys. Rev. Lett.* **2002**, *88*, 056803

26. Pisana, S.; Lazzeri, M.; Casiraghi, C.; Novoselov, K. S.; Geim, A. K.; Ferrari, A. C.; Mauri, F. Breakdown of the adiabatic Born-Oppenheimer approximation in graphene. *Nat. Mater.* **2007**, *6*, 198-201.

27. Choi, D. H.; Randall, C.; Furman, E.; Ma, B. H.; Balachandran, U. B.; Zhang, S. H.; Lanagan, M.; Ieee In *Energy and Power Densities of Capacitors and Dielectrics*, IEEE International Workshop on Integrated Power Packaging, 2015; pp 52-55.

28. Sader, J. E.; Chon, J. W. M.; Mulvaney, P. Calibration of rectangular atomic force microscope cantilevers. *Rev. Sci. Instrum.* **1999**, *70*, 3967-3969.
29. Jacobs, H. O.; Knapp, H. F.; Stemmer, A. Practical aspects of Kelvin probe force microscopy. *Rev. Sci. Instrum.* **1999**, *70*, 1756-1760.
30. Gil, A.; Colchero, J.; Gómez-Herrero, J.; Baró, A. M. Electrostatic force gradient signal: resolution enhancement in electrostatic force microscopy and improved Kelvin probe microscopy. *Nanotechnology* **2003**, *14*, 332-340.
31. Glatzel, T.; Sadewasser, S.; Lux-Steiner, M. C. Amplitude or frequency modulation-detection in Kelvin probe force microscopy. *Appl. Surf. Sci.* **2003**, *210*, 84-89.
32. Kitamura, S.; Iwatsuki, M. High-resolution imaging of contact potential difference with ultrahigh vacuum noncontact atomic force microscope. *Appl. Phys. Lett.* **1998**, *72*, 3154-3156.
33. Gimeno, A.; Ares, P.; Horcas, I.; Gil, A.; Gomez-Rodriguez, J. M.; Colchero, J.; Gomez-Herrero, J. 'Flatten plus': a recent implementation in WSxM for biological research. *Bioinformatics* **2015**, *31*, 2918-2920.
34. Horcas, I.; Fernandez, R.; Gomez-Rodriguez, J. M.; Colchero, J.; Gomez-Herrero, J.; Baro, A. M. WSXM: A software for scanning probe microscopy and a tool for nanotechnology. *Rev. Sci. Instrum.* **2007**, *78*, 013705.
35. Glatzel, T.; Sadewasser, S., *Kelvin Probe Force Microscopy, Measuring & Compensating Electrostatic Forces*. Springer Series in Surface Sciences, 2012.
36. Zerweck, U.; Loppacher, C.; Otto, T.; Grafstrom, S.; Eng, L. M. Accuracy and resolution limits of Kelvin probe force microscopy. *Phys. Rev. B* **2005**, *71*, 125424.

Supplementary

S1. Electrostatic force microscopy (EFM)

EFM measures the electrostatic force acting between a conductive tip and the sample with an applied electric bias. This force is the sum of the capacitive interaction between the tip and the sample, which depends on its surface potential and dielectric properties of the sample, and the Coulombic interaction between the tip and the static charges/multipoles on the surface, as described in refs.[1,2] The total force can then be written as follows:[2]

$$F = \frac{1}{2}\frac{\partial C}{\partial z}V^2 + E_z Q_t \quad (1)$$

where V is the electric potential difference and C is the capacitance between the tip and the sample, Q_t is the total charge on the tip, and E_z is the z-component of the electric field arising from the charges on the surface. The capacitive term depends on the first derivative of the tip-sample capacitance, $\partial C/\partial z$, respect to the tip-sample distance, z. This in turn is a complicated function of geometrical and dielectric properties of the probe-sample system.[3]

In this work, we carried out ac-EFM imaging by applying an ac bias voltage $V = V_{ac}A\ sin(\omega t)$ between tip and the bottom conductive substrate (doped silicon). In this case, it can be shown that the electrostatic force is the sum of three components at 0, ω and 2ω frequencies

$$F = F_{dc} + F_{\omega}V_{ac}\ sin(\omega t) + F_{2\omega}V_{ac}^2 sin\ (2\omega t) \quad (2)$$

where

$$F_{\omega} = f_{\omega}\left(C, \frac{\partial C}{\partial z}, V_{CPD}, \varepsilon\right) + E_{z,dc}C \quad \text{and} \quad F_{2\omega} = f_{2\omega}\left(C, \frac{\partial C}{\partial z}, \varepsilon\right) \quad (3)$$

as described in ref.[2]. The amplitude of the first harmonic, F_{ω}, can be written as the sum of a capacitive term and a term proportional to the electric field generated by static charges on the surface. The capacitive term is a complicated function of various parameters, namely, the tip-substrate capacitance and its first derivative, the dielectric properties of the sample, ε, and the tip-substrate contact potential difference, V_{CPD}. On the other hand, the amplitude of the second harmonic, $F_{2\omega}$, is not dependent on the static charge distribution on the surface. It is a purely capacitive term that depends only on the tip-substrate capacitance and the dielectric properties of the sample.

In this study, we measured both the first harmonic ω and the second harmonic 2ω using a multifrequency lock-in amplifier. This allowed us to detect the electric field generated by strain-induced charge densities in the ω-image, which we referred to as the electric image. The 2ω-image, which we referred to as the dielectric image, is a control image that allowed us to detect any variation in the tip-sample capacitive interaction. We thus verified that the observed variations in the electric image are indeed associated to the

presence of static charges and do not reflect variations in the tip-sample capacitive interaction.

Following Glatzel *et al*. nomenclature,[4] EFM images can be obtained either in amplitude modulation (AM)[5] or in frequency modulation (FM)[6] mode. In AM mode, the electrostatic force is directly detected, while in FM mode it is the force gradient. Here we used the FM mode in single-pass mode, detecting the first and second harmonic of the force gradient while taking topography images. This approach proves advantageous because it enhances the sensitivity and lateral resolution of the measurement by minimizing the tip-surface distance and stray capacitance contributions. To avoid topographic cross talks, the tip was electrically oscillated at low frequencies, at 1.8 kHz with amplitude 4 V, two orders of magnitude far from the mechanical vibration of the cantilever (at 137 kHz).

Figures S1, S2 and S3 below are additional topographic and electric images taken on monolayer, bilayer and multilayer hBN.

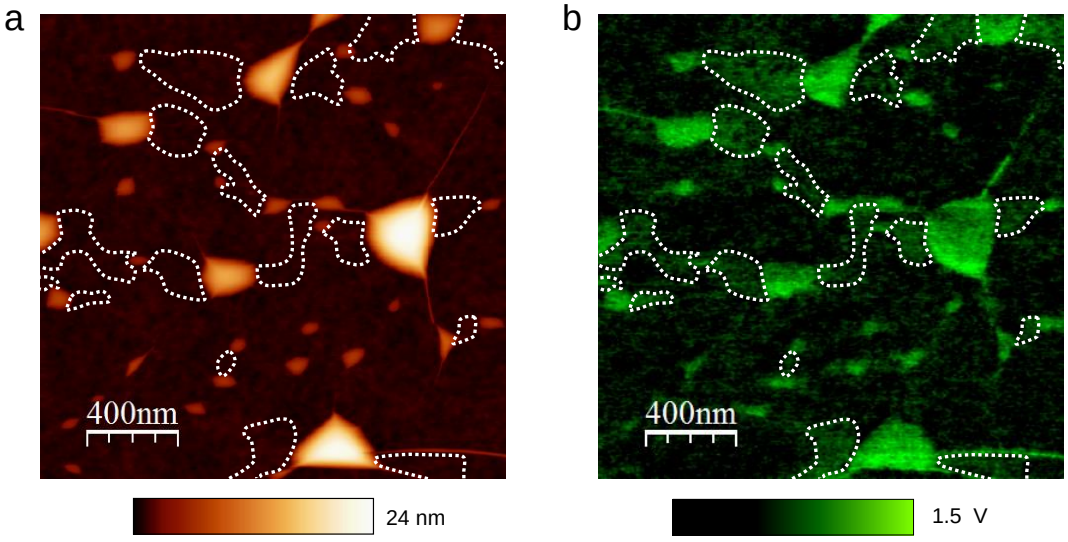

Figure S1. Additional AFM and EFM images of the monolayer hBN areas with bubbles. (a) Topography and (b) electric images of hBN/graphene on a SiO_2/Si substrate, showing enhanced contrast around and between the bubbles.

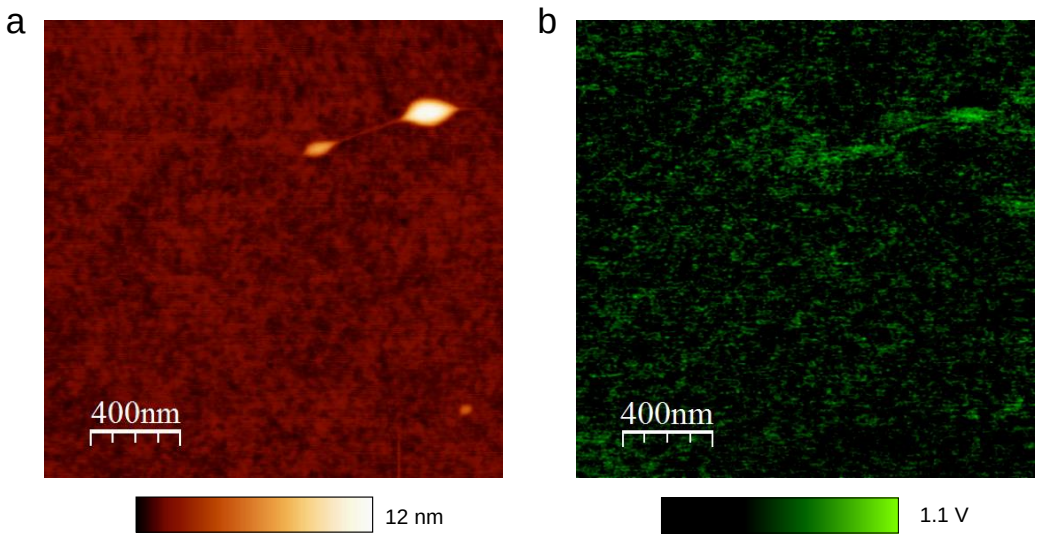

Figure S2. AFM and EFM of a monolayer hBN area without bubbles. (a) Topography image and (b) corresponding electric image, showing no areas with enhanced contrast.

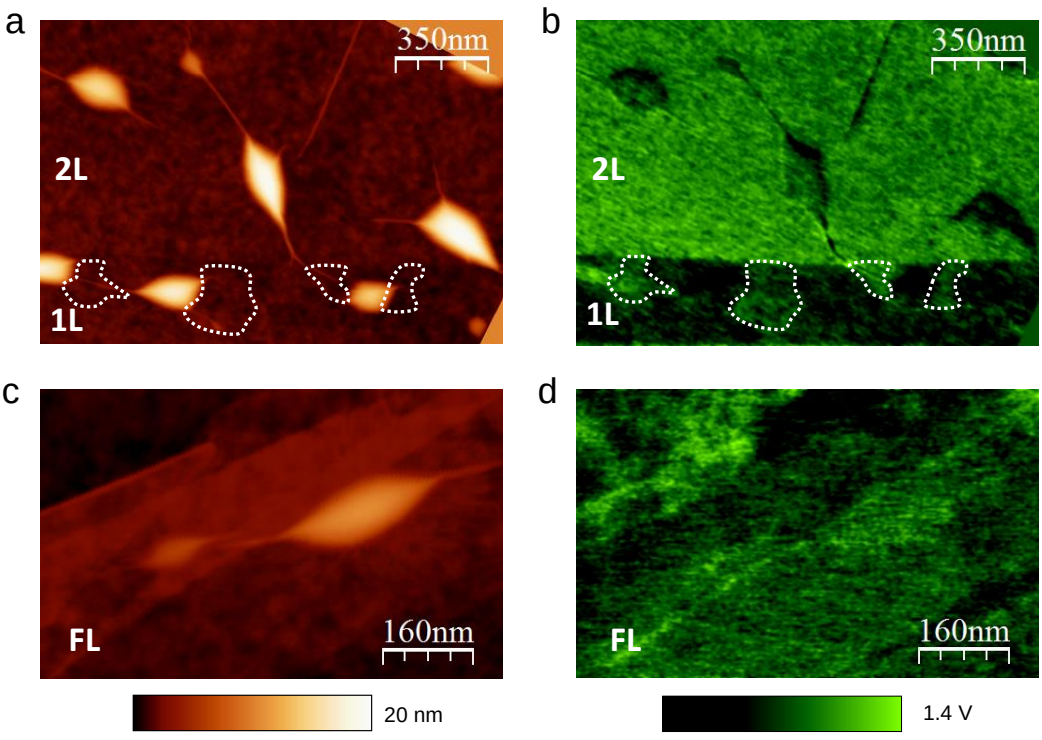

Figure S3. AFM and EFM of monolayer (1L), bilayer (2L) and few-layer (FL) hBN areas with bubbles. (a,c) Topography and (b,d) corresponding electric images, showing no contrast variations around or between bubbles in the bilayer and a multilayer. Conversely, they can be observed on the monolayer region.

S2. The elasticity problem in the deformed honeycomb lattice

Here we describe the method used to compute the piezoelectric induced polarization and charge density generated by bubbles in monolayer hBN. Our technical analysis consists in solving the elasticity equations for the membrane in the honeycomb lattice by means of a discretization procedure. The strain fields obtained for different profiles of bubbles are used to calculate the piezoelectric induced charge density and the electric fields.

We start by considering a single sheet of hBN in the continuum limit, in which the free energy of the membrane is given by the classical theory of elasticity:[7,8]

$$F_{el}[\boldsymbol{u}, w] = \frac{1}{2}\int d^2x\left[\kappa(\nabla^2 w)^2 + \left(\lambda u_{ii}^2 + 2\mu u_{ij}^2\right)\right] \quad (4)$$

where u_{ij} is the strain tensor

$$u_{ij} = \frac{1}{2}\left(\partial_i u_j + \partial_j u_i + \partial_i w \partial_j w\right) \quad (5)$$

with u_i the field associated to the in plane displacements in the $i-th$ direction ($i = x, y$), w that associated to the out of plane displacements, $\kappa = 0.82$ eV is the bending rigidity, $\lambda = 23.39$ eV$/l^2$ and $\mu = 49.55$ eV$/l^2$ are the Lamé coefficients of hBN,[9] l being the lattice constant. The value of l in the atomic limit is $l_0 = \sqrt{3}a_0 = 2.52$ Å, which gives: $\lambda_0 = 3.68$ eVÅ^{-2} and $\mu_0 = 7.80$ eVÅ^{-2}.

We consider the case in which the configuration of the out of plane displacements is defined as to reproduce the different shapes of bubbles observed in the experiments, $w(x, y) \equiv w_0(x, y)$. Therefore the free energy F_{el} is a functional of the in plane fields u_i only, and the bending energy represented by the first term of equation (4) can be safely neglected, since it is just an additive constant to the total energy.

At equilibrium, the configuration of the u_i fields that minimizes F_{el} is given by the solution of the following elasticity equations:

$$\lambda\partial_x\left(\partial_x u_x + \partial_y u_y + \frac{|\nabla w|^2}{2}\right) + \mu\partial_x[2\partial_x u_x + (\partial_x w)^2] + \mu\partial_y\left(\partial_y u_x + \partial_x u_y + \partial_x w \partial_y w\right) = 0 \quad (6a)$$

$$\lambda\partial_y\left(\partial_x u_x + \partial_y u_y + \frac{|\nabla w|^2}{2}\right) + \mu\partial_y\left[2\partial_y u_y + \left(\partial_y w\right)^2\right] + \mu\partial_x\left(\partial_y u_x + \partial_x u_y + \partial_x w\partial_y w\right) = 0 \qquad (6b)$$

that are nothing but the static Euler-Lagrange equations.

We next generalize equations (6) to the discrete case by replacing the partial derivatives with their corresponding finite differences on the honeycomb lattice. For this we follow the approach of refs [10,11]. The honeycomb lattice consists of two sub-lattices, that here we label *A* and *B* (Figure S4). In the particular case of hBN, the two species correspond to Nitrogen and Boron atoms, respectively. Each atom of type *A* has three first nearest neighbors of type *B*, that we labeled with the indices 1,2,3, and six second nearest neighbors of type *A*, labeled by the indices 4,…9.

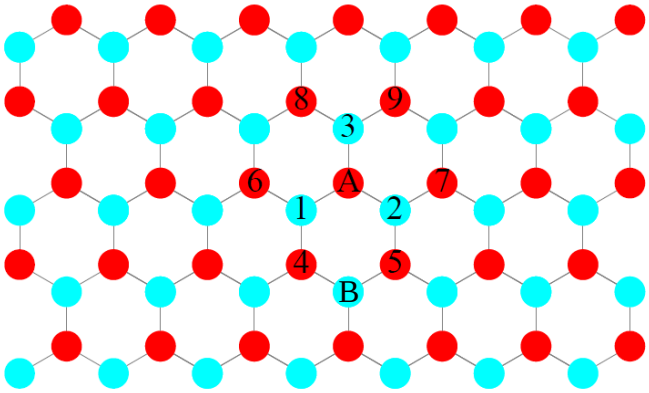

Figure S4. The honeycomb lattice of hBN. For a given site of type *A* (red), there are three first nearest neighbors 1,2,3 of type *B* (cyan) and six second nearest neighbors 4,…9 of type *A*.

According to Figure S4, if the point *A* has coordinates (x, y), the coordinates of its nine nearest neighbors are then:

$$n_1 = \left(x - \frac{l}{2}, y - \frac{l}{2\sqrt{3}}\right), \quad n_2 = \left(x + \frac{l}{2}, y - \frac{l}{2\sqrt{3}}\right), \quad n_3 = \left(x, y + \frac{l}{\sqrt{3}}\right)$$

$$n_4 = \left(x - \frac{l}{2}, y - \frac{l\sqrt{3}}{2}\right), \quad n_5 = \left(x + \frac{l}{2}, y - \frac{l\sqrt{3}}{2}\right), \quad n_6 = (x - l, y)$$

$$n_7 = (x + l, y), \quad n_8 = \left(x - \frac{l}{2}, y + \frac{l\sqrt{3}}{2}\right), \quad n_9 = \left(x + \frac{l}{2}, y + \frac{l\sqrt{3}}{2}\right)$$

(7)

An analogous scheme holds for each atom of type *B*, with an equivalent definition of the nearest neighbors. The partial derivatives of first and second order that appear in the continuum equations (6) can be replaced by their corresponding finite differences on the lattice, by introducing the following operators:[10,11]

$$Tf(A) = f(n_1) - f(A) + f(n_2) - f(A) + f(n_3) - f(A) \sim \frac{l^2}{4}\nabla^2 f$$

(8a)

$$Hf(A) = f(n_6) - f(A) + f(n_7) - f(A) \sim l^2 \partial_x^2 f$$

(8b)

$$Df(A) = f(n_4) - f(n_5) + f(n_9) - f(n_8) \sim l^2\sqrt{3}\partial_x \partial_y f$$

(8c)

$$\Delta_x f(A) = \frac{f(n_7) - f(n_6)}{2} \sim l\partial_x f$$

(8d)

$$\Delta_y f(A) = \frac{f(n_3) - f(A) - [f(n_1) - f(A) + f(n_2) - f(A)]}{2} \sim \frac{l}{\sqrt{3}}\partial_y f$$

(8e)

where f is a generic function of the lattice positions. Thus, the elasticity equations on the honeycomb lattice can be written as:

$$4\mu T u_x + (\lambda + \mu) H u_x + \frac{\lambda+\mu}{\sqrt{3}} D u_y + \frac{\lambda+\mu}{l}\left[\Delta_x w H w + \Delta_y w D w\right] + \frac{4\mu}{l}\Delta_x w T w = 0$$

(9a)

$$4(\lambda + 2\mu) T u_y - (\lambda + \mu) H u_y + \frac{\lambda+\mu}{\sqrt{3}} D u_x + \frac{4\sqrt{3}}{l}(\lambda + 2\mu)\Delta_y w T w + \frac{\lambda+\mu}{l\sqrt{3}}\left[\Delta_x w D w - 3\Delta_y w H w\right] = 0$$

(9b)

Notice that in equations (8d) and (8e) we used a symmetric definition of the first order differences, which differs from the one adopted in previous works.[10,11] Although this choice is completely irrelevant when dealing with periodic boundary conditions, it

becomes necessary in the case of clamped boundary conditions (zero displacements at the edges of the lattice), in order to prevent the appearance of any preferential direction.

As an illustrative example, Figure S5 shows the equilibrium configuration of the membrane as obtained from the numerical solution of equations (9) in the presence of clamped boundary conditions and of a circular bubble given by: $w(x,y) = w_{max}\left[1-\left(\frac{r}{R}\right)^2\right]\Theta\left[1-\left(\frac{r}{R}\right)^2\right]$, with $r^2 = x^2 + y^2$, $R = 4l$, and $w_{max} = 4.33l$. As it is evident from the stretching (and eventually shrinking) of the B-N bonds in proximity of the bubble, the system is forced to develop a finite strain u_{ij}, that would be absent in the flat case $w = 0$.

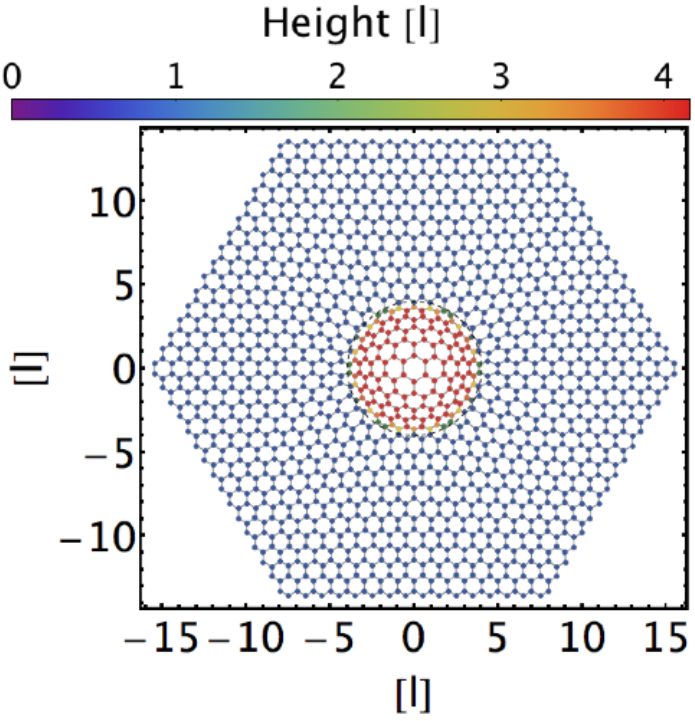

Figure S5. Example of circular bubble. Numerical solution of the elasticity equations (13) in the presence of clamped boundary conditions and of a circular bubble. The out of plane displacement *w* is represented as a color map displaying the heights of the lattice points in units of l.

S3. Evaluation of the charge density and electric field generated by the piezoelectric effect in the presence of bubbles

In the presence of a finite strain field u_{ij}, piezoelectric crystals acquire a polarization $\boldsymbol{P}$ given by: $P_i = \sum_{jk} \gamma_{ijk} u_{jk}$, where γ_{ijk} is the third-rank piezoelectric tensor. The local variations of this polarization field can generate charge *self-doping*, with charge density given by:[12]

$$\rho = -\nabla \cdot \boldsymbol{P} \tag{10}$$

Equation (10) implies that $\boldsymbol{P}$ is proportional to the electric field $\boldsymbol{E}$, according to the Maxwell law: $\boldsymbol{E} = -\boldsymbol{P}/\varepsilon_{2d}$, where $\varepsilon_{2d} \equiv \varepsilon_r \varepsilon_0 l_\perp$ is the dielectric constant of the bi-dimensional film, with ε_r the relative permittivity along the c axis, ε_0 the permittivity of the vacuum, and $l_\perp$ the interlayer spacing. The characterizations of hBN given by the refs. [13,14] provide the following values: $\varepsilon_r = 6.85$ and $l_\perp = 3.33$ Å.

For the case of monolayer hBN and related 2D crystals, one can exploit the symmetries of the piezoelectric tensor to write the piezoelectric induced polarization as:[15]

$$\boldsymbol{P} = \gamma \mathcal{A} \times \hat{\boldsymbol{z}} \tag{11}$$

with

$$\mathcal{A} = (u_{xx} - u_{yy})\hat{\boldsymbol{x}} - 2u_{xy}\hat{\boldsymbol{y}} \tag{12}$$

and γ the piezoelectric constant of the material. Here we use the value $\gamma = 2.91 \times 10^{-10}$ C/m, as given by the analytic estimate based on the $\boldsymbol{k} \cdot \boldsymbol{p}$ method.[15]

Using equations (10)-(12) along with the definition (5) of the strain field u_{ij}, the charge density can be written as:

$$\rho = \gamma[(\partial_x^2 - \partial_y^2)u_y + (\partial_y w)(\partial_x^2 - \partial_y^2)w + 2(\partial_x \partial_y u_x + \partial_x w \partial_x \partial_y w)] \tag{13}$$

In the case of the honeycomb lattice that we are considering here, the partial derivatives appearing in the previous expression must be replaced by their corresponding finite differences defined in the equations (8), which gives:

$$\rho = \frac{\gamma}{l^2}\left[2(H-2T)u_y + \frac{2\sqrt{3}}{l}\Delta_y w(H-2T)w + \frac{2}{\sqrt{3}}\left(Du_x + \frac{1}{l}\Delta_x wDw\right)\right] \quad (14)$$

S4. Numerical results

Here we report on the numerical results obtained by solving the discrete elasticity equations (9) in the presence of different bubble shapes. In particular, given the polarization field $\boldsymbol{P}$, we compute the charge density ρ according to equation (14) and the energy density of the electric field generated by the piezoelectric effect: $u_E = \frac{\varepsilon_{2d}}{2}|\boldsymbol{E}|^2 = \frac{1}{2\varepsilon_{2d}}|\boldsymbol{P}|^2$. The results refer to lattices of size $N_s = 61200$ atoms (or bigger, when specified) with clamped boundary conditions. From the energy density of the electric field generated by the piezoelectric effect we can obtain the electrostatic force distribution acting normal to the surface by computing the first derivative with respect to the out of plane direction.[16,17]

Figure S6 shows the numerical results obtained in the case of a perfectly circular bubble, as given by the following height profile:

$$w(x,y) = w_0 e^{-\left(\frac{x^2+y^2}{R^2}\right)} \quad (15)$$

which displays a gaussian decay moving from the center of the bubble. Here $w_0 = 28$ nm is the maximum height of the bubble and $R = 380$ nm its radius.

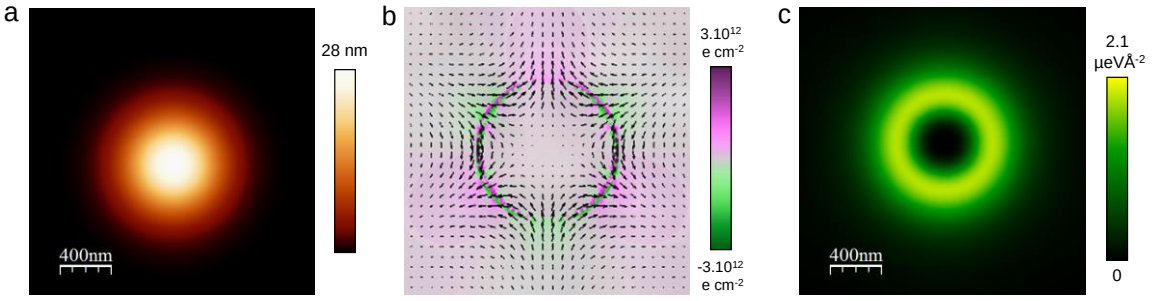

Figure S6. Perfectly circular bubble with height profile given by equation (15). (a) Topography. (b) Charge density. The superimposed arrows represent the polarization field. (c) Energy density of the electric field.

Figure S7 displays a triangular bubble having the same shape of that of Figure 4a in the main text, but different orientations θ with respect to the crystallographic axes. We considered the cases $\theta = 0°$ (first column), $\theta = 20°$ (second column), $\theta = 40°$ (third column), and $\theta = 60°$ (fourth column). These cases show that the distribution of energy and electric fields is not strikingly affected by the particular orientation of the bubble, but rather by its geometry, as the energy results to be concentrated mainly along the sides of the bubble and the creases.

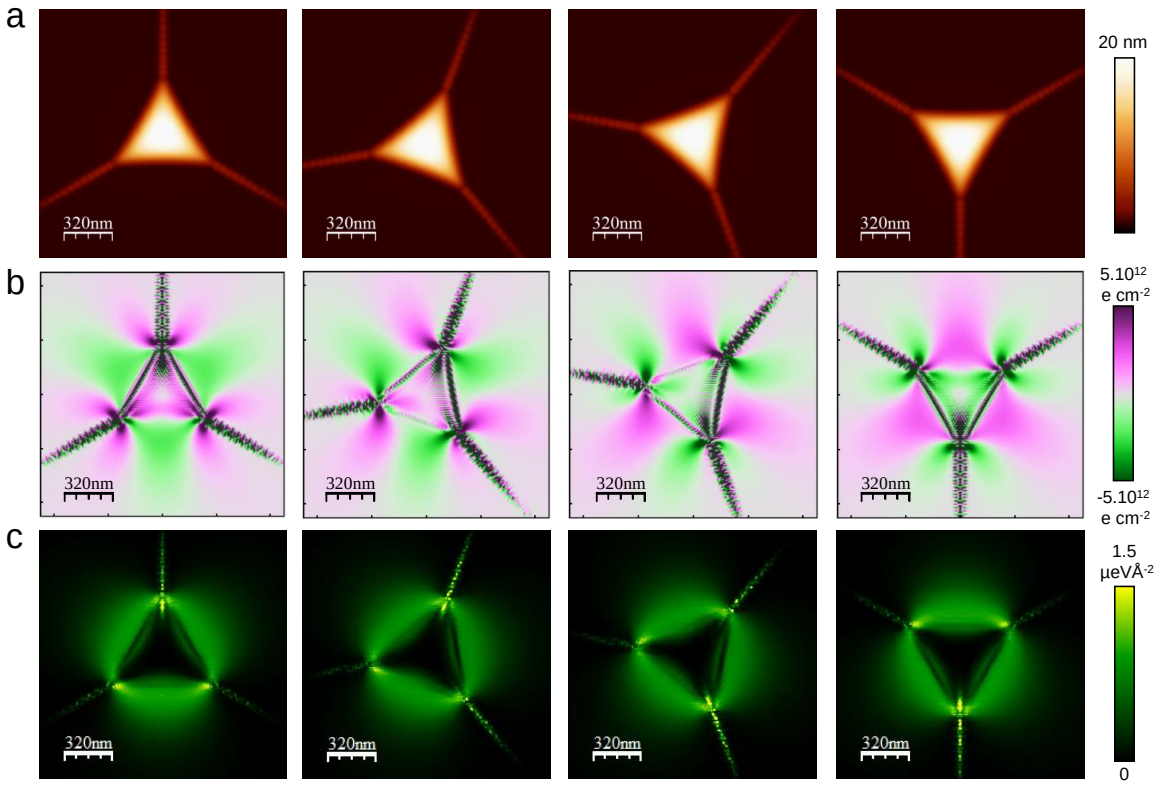

Figure S7. Triangular bubble at different orientations with respect to the crystallographic axes. (a) Topography. (b) Charge distribution. (c) Energy density. Columns from left to right correspond to rotations of $\theta = 0°, 20°, 40°$ and $60°$ with respect to the crystallographic axes, respectively.

Figure S8 refers to the geometrical configuration of an elliptical bubble with one-dimensional creases at the vertical corners. This bubble shape has been obtained by means of the following analytical expression for the height field:

$$w(x,y) = w_0 exp\left[-\left(\frac{x}{b}e^{y^2/c^2}\right)^4\right]e^{-2y^2/c^2} + w_c e^{-x^2/\xi^2}\left[e^{-\left(\frac{y-2c}{c}\right)^2} + e^{-\left(\frac{y+2c}{c}\right)^2}\right] \quad (16)$$

where $w_0 = 10$ nm is the maximum height of the bubble, $b = 57$ nm, $c = 210$ nm, $w_c = 1$ nm is the maximum height of each crease and $\xi = 10$ nm sets the width of the creases.

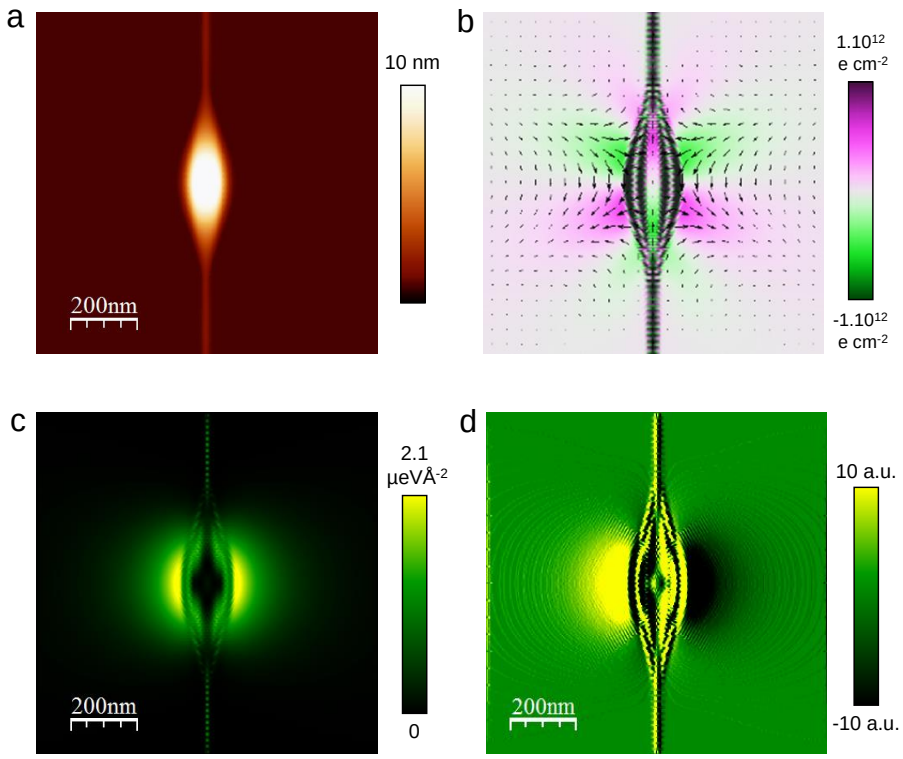

Figure S8. Elliptical bubble with one-dimensional creases as obtained from the height profile given by equation (16). (a) Topography. (b) Charge density. The superimposed arrows represent the polarization field. (c) Energy density of the electric field. (d) Electrostatic force distribution.

Finally, we report the analytical expression used to modulate the height field in the configuration in which two bubbles are connected by many ultrathin creases, corresponding to Figure 4d-f of the main text and to Figure S9 of the next section:

$$w(x,y) = w_0 e^{-2y^2/c^2}\left\{exp\left[-\left(\frac{x-D/2}{b}e^{y^2/c^2}\right)^4\right] + exp\left[-\left(\frac{x+D/2}{b}e^{y^2/c^2}\right)^4\right]\right\} +$$

$$+\sum_{n=-N}^{N} w_c e^{-[(y-nd)/\xi]^2}\left\{e^{-(1-2x/D)^2} + \theta(x+D/2)e^{-(1+2x/D)^2} + [1-\theta(x+D/2)]e^{-[(x+D/2)2/b]^2}\right\} \quad (17)$$

where $w_0 = 20$ nm is the maximum height of each bubble, $D = 400$ nm is the distance between their centers, $b = 75$ nm, $c = 150$ nm, $2N + 1 = 11$ is the number of creases, $d = 10$ nm is the distance between the creases, $w_c = 0.45$ nm sets the height of the creases in $x = 0$ at approximatively 0.3-0.4 nm, and $\xi = 2.5$ nm sets the width of each crease. The numerical results concerning this configuration have been obtained by solving the elasticity equations in a lattice of $N_s = 242400$ atoms, which is much larger than that corresponding to the other results shown in the present work. Such a large size has been indeed necessary to reproduce the narrow feature of the creases. The geometry of the creases can be better visualized in the Figure S9b below.

S5. Comparison between simulated and experimental images

As described in the main text, we found atomically thin creases around many bubbles, which generate large strains. Such creases can extend over distances up to hundreds of nanometers from the bubbles and connect different bubbles. To better compare our experimental images with the simulations, we included such ultrathin creases in the theoretical model. Figure S9a shows a topographical simulation with atomically thin creases that connect two elliptical bubbles. The simulation reproduced the spacing (~ 10 nm) and the height (3 Å) of the creases that we experimentally observed, as shown in AFM topography image given in Figure S9c and in the main text (Figure 2d). Figure S10a,b shows the corresponding calculated electric field energy density and its profile, which predicts that the piezoelectric field extends along the ultrathin creases in the region between the bubbles, in qualitative agreement with our observations in the EFM image (Figure S10c).

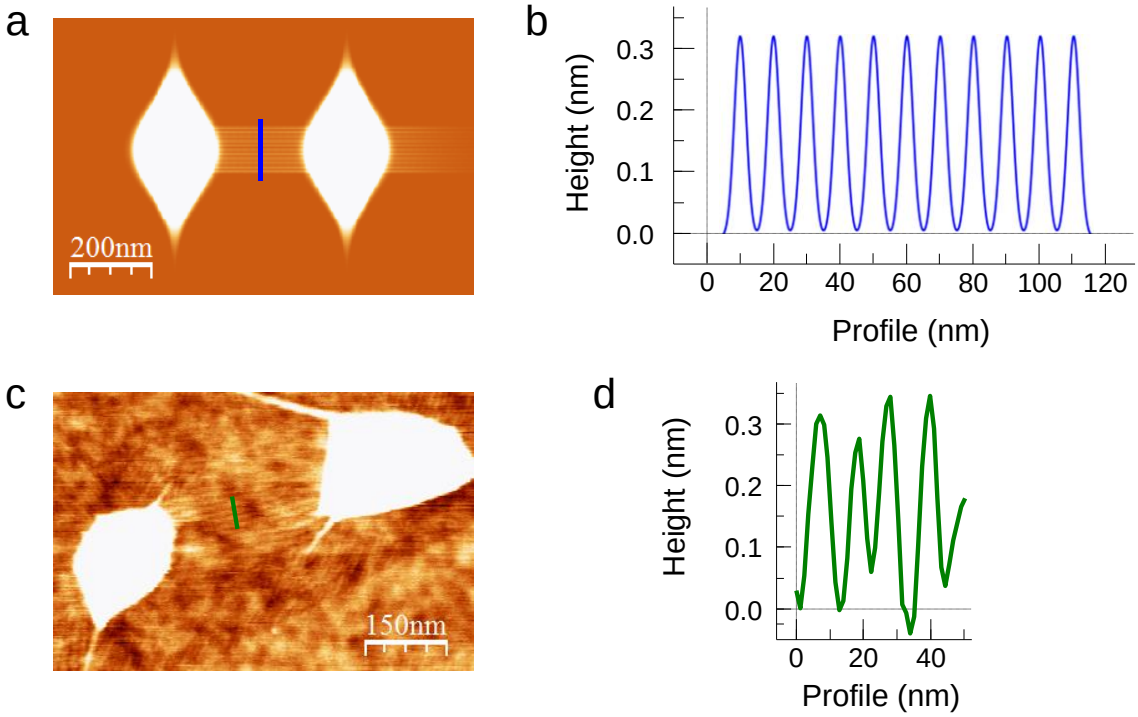

Figure S9. Analytical simulation of the thin creases mimicking the experimental observations. (a) Simulated topography image, same image as Figure 4d in the main text, with height profile given by equation (17). (b) Profile along the line in (a). (c) Experimental topography, same image as Figure 2d in the main text. (d) Profile along the line in (c).

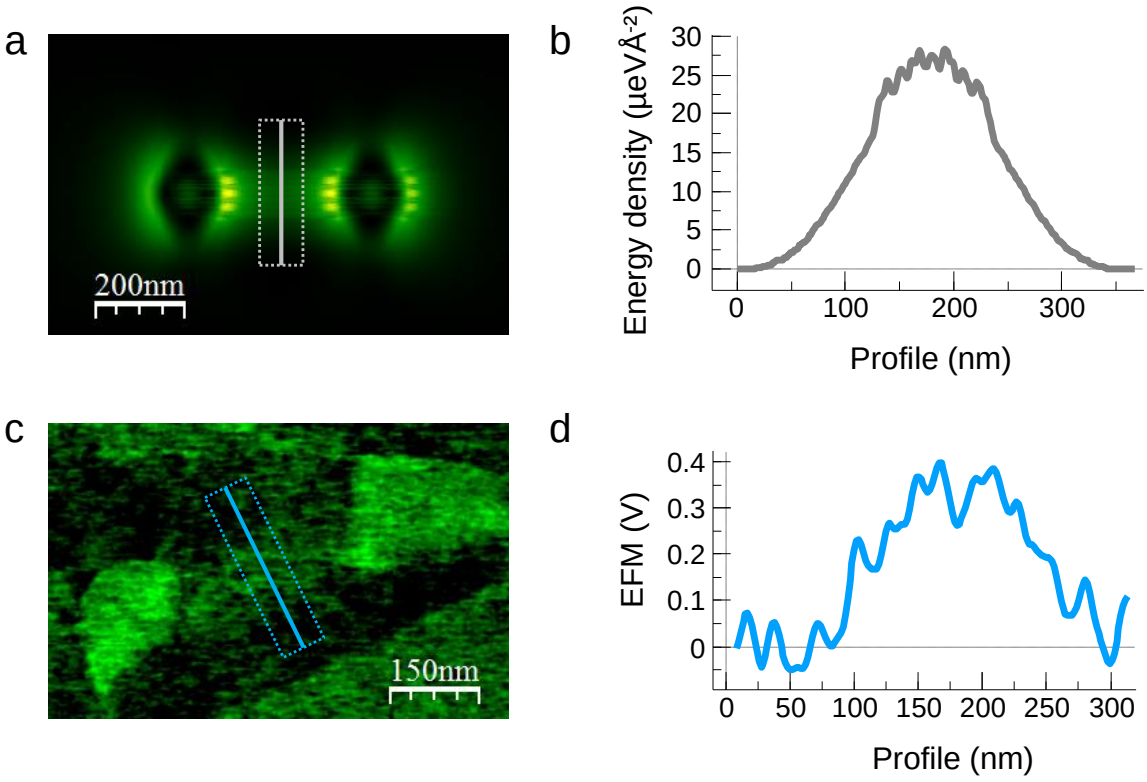

Figure S10. Comparison between simulated electric field energy density and EFM data. (a) Electric field energy density simulation, same image as Figure 4f in the main text. (b) Average smoothed profile along the vertical line and in a corresponding to the area enclosed by the dotted rectangle. (c) Experimental EFM data, same image as Figure 2e in the main text. (d) Average profile along the line in (c) corresponding to the area enclosed by the dotted rectangle.

S6. Polyelectrolyte nanoparticles deposition

We further verified the piezoelectricity of the hBN monolayer by using an indirect approach. We utilized the electrophoretic properties of a polyelectrolyte solution, Poly(ethyleneimine) (PEI), in salinated water. We deposited the PEI nanoparticles in solution onto the surface of our samples, allowed the solution to dry, and then washed off the majority of the polymer/salt. The resultant samples consisted of the original heterostructure and only the most strongly adhered PEI molecules. The distribution of remaining polyelectrolytes was measured with PeakForce-AFM (description to follow). These polymer chains have a characteristic length of 50 nm to 1700 nm depending upon the PH of the saline suspension they are deposited in. At PH10 the nanoparticles closed in a spherical shape, and, as the PH is lowered, the characteristic length increases. In our experiments we used PH6, which yields slightly elongated particles (up to 150 nm). At lower PHs, the distribution of PEI on the sample becomes dominated by the interaction between polyelectrolytes, rather than the adhesion to the sample.

The elongated polyelectrolytes experience a Debye force in the presence of a polarizing field which drives and orients the molecules, 'electrophoretic motion'. Since the majority of polymers and salt are washed off in the processing steps, only the most strongly adhered PEI molecules remain; their orientation dominated by the piezoelectric response to monolayer hBN's strain field. Figure S11a,d show simulations of the electrostatic force distribution on monolayer hBN based on the bubble geometries observed in topographical AFM images (Figure S11b,e). In these cases, we can observe a characteristic PEI distribution around the bubbles: PEI molecules clearly tend to orient in the direction of the electrostatic force lines and a direct correlation can be established between the alignment of the nanoparticles and the electrostatic force simulation (Figure S11c,f). However, this contrasts to the case of bulk hBN (Figure S11g,h), where the PEI nanoparticles have no clear order. These results are in good agreement with the presence of an electric field generated by the piezoelectric effect around strained areas such as bubbles and creases in the monolayer.

PeakForce-AFM was used here. PeakForce-AFM is a scanning probe technique used to establish real-time control of the exact maximal-force between probe and the sample (the peak-force). Further, force/time profiles can be extracted for each pixel, which allows us to understand different aspects of the tip/sample interaction. The details are explained in

detail in ref.[18]. Here we minimized the peak-force to reduce the influence of the tip on the sample, and used only the topography signal (height) in our analysis.

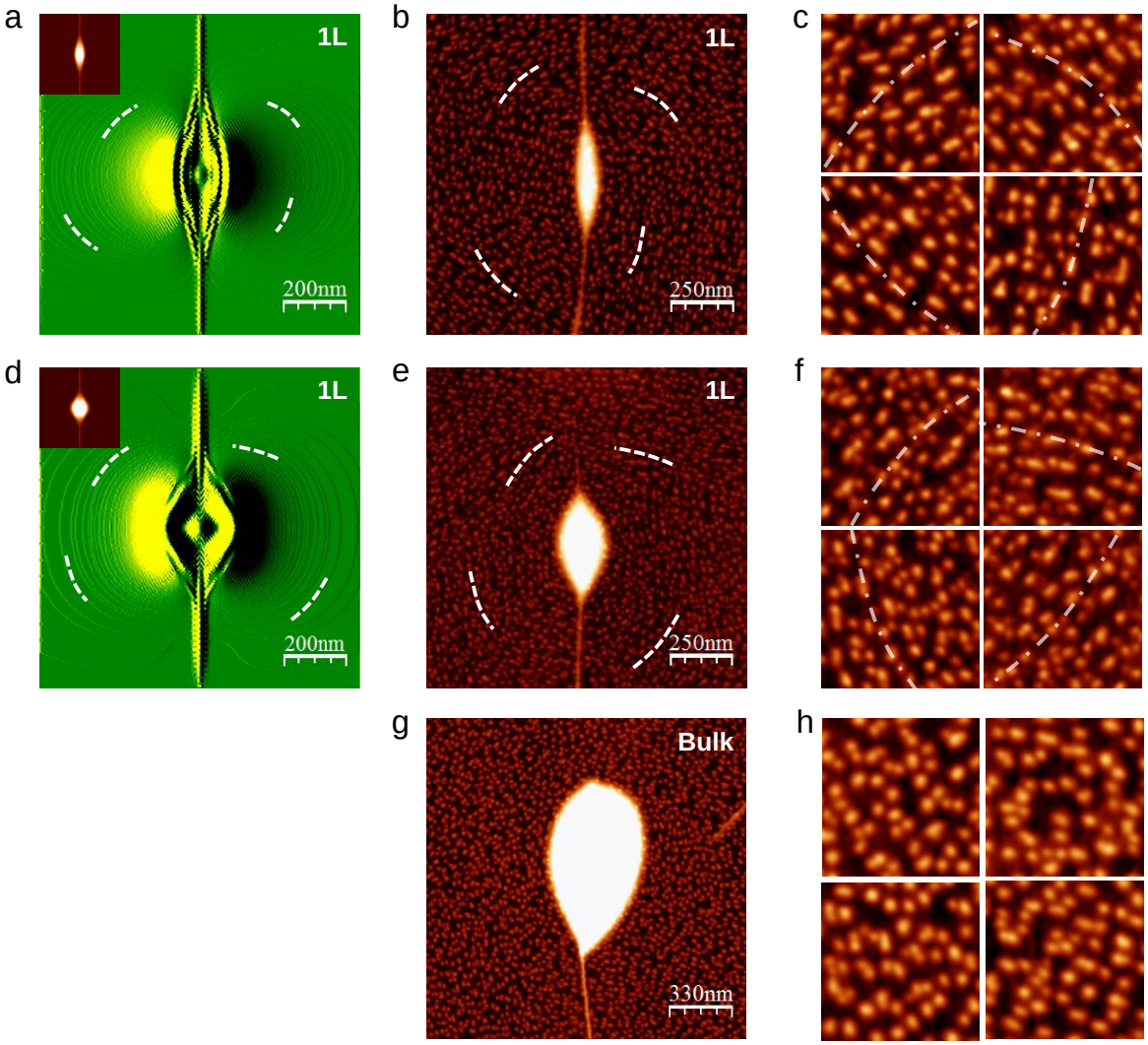

Figure S11. Indirect evidence of the piezoelectric field generated around bubbles. (a,d) Electrostatic force distributions of bubbles in monolayer hBN mimicking the ones observed experimentally in (b,e). The insets show the topographical simulations. The dashed lines were drawn to guide the eye along the electric field lines. (c,f) 250x250 nm^2 zooms in the areas around the dashed lines in (b,e) respectively. The dash-dotted lines are a guide to the eye and correspond to the dashed lines in (b,e). (g) Bubble in bulk hBN and (h) zooms from areas where alignment of the PEI nanoparticles should be expected in case of being a monolayer. In the monolayer (c,f) a clear alignment of the

nanoparticles to the electric field lines is detected, while this is absent in the bulk hBN (h) where the nanoparticles are located at random positions.

References

1 Terris, B. D., Stern, J. E., Rugar, D. & Mamin, H. J. Contact Electrification Using Force Microscopy. *Phys. Rev. Lett.* **63**, 2669-2672, (1989).

2 Cherniavskaya, O., Chen, L. W., Weng, V., Yuditsky, L. & Brus, L. E. Quantitative noncontact electrostatic force Imaging of nanocrystal polarizability. *J. Phys. Chem. B* **107**, 1525-1531, (2003).

3 Fumagalli, L., Esteban-Ferrer, D., Cuervo, A., Carrascosa, J. L. & Gomila, G. Label-free identification of single dielectric nanoparticles and viruses with ultraweak polarization forces. *Nat. Mater* **11**, 808–816, (2012)

4 Glatzel, T., Sadewasser, S. & Lux-Steiner, M. C. Amplitude or frequency modulation-detection in Kelvin probe force microscopy. *Appl. Surf. Sci.* **210**, 84-89, (2003).

5 Kikukawa, A., Hosaka, S. & Imura, R. Silicon PN Junction Imaging and Characterizations Using Sensitivity Enhanced Kelvin Probe Force Microscopy *Appl. Phys. Lett.* **66**, 3510-3512, (1995).

6 Kitamura, S. & Iwatsuki, M. High-resolution imaging of contact potential difference with ultrahigh vacuum noncontact atomic force microscope. *Appl. Phys. Lett.* **72**, 3154-3156, (1998).

7 Landau, L. & Lifshitz, E. *Theory of Elasticity*. Vol. 7 (Pergamon Press, 1970).

8 Nelson, D. R. & Peliti, L. Fluctuations in membranes with crystalline and hexatic order. *J. Phys. France* **48**, 1085-1092, (1987).

9 Sachs, B., Wehling, T. O., Katsnelson, M. I. & Lichtenstein, A. I. Adhesion and electronic structure of graphene on hexagonal boron nitride substrates. *Phys. Rev. B* **84**, 195414, (2011).

10 Bonilla, L. L. & Carpio, A. Model of ripples in graphene. *Phys. Rev. B* **86**, 195402 (2012).

11 Carpio, A. & Bonilla, L. L. Periodized discrete elasticity models for defects in graphene. *Phys. Rev. B* **78**, 085406, (2008).

12 Griffiths, D. J. *Introduction to Electrodynamics*. (Pearson, 2012).

13 Geick, R., Perry, C. H. & Rupprech.G. Normal modes in hexagonal boron nitride. *Phys. Rev.* **146**, 543-547, (1966).

14 Pease, R. S. An X-ray study of boron nitride. *Acta Crystallogr*. **5**, 356-361, (1952).

15 Rostami, H., Guinea, F., Polini, M. & Roldán, R. Piezoelectricity and valley chern number in inhomogeneous hexagonal 2D crystals. *NPJ 2D Mater. Appl.* **2**, 15, (2018).

16 Glatzel, T. & Sadewasser, S. *Kelvin Probe Force Microscopy, Measuring & Compensating Electrostatic Forces*. (Springer Series in Surface Sciences, 2012).

17 Zerweck, U., Loppacher, C., Otto, T., Grafstrom, S. & Eng, L. M. Accuracy and resolution limits of Kelvin probe force microscopy. *Phys. Rev. B* **71**, 125424, (2005).

18 Pittenger, B. B., Erina, N. & Su, C. Application Note #128. Quantitative Mechanical Property Mapping at the Nanoscale with PeakForce QNM. *Bruker*, (2012).

Chapter 8

Convergent beam electron holography for analysis of van der Waals heterostructures

The results are from a published paper in PNAS, 17th July 2018, 115 (29) 7473-7478

In this work, convergent beam electron holography used as a technique to investigate the stacking order of aligned graphene/hBN heterostructures. It provides visual information of defects in heterostructures at the atomic scale, with a field of view of the order of thousands of square nanometre.

My contribution to the work includes: flake preparation and fabrication of aligned graphene/hBN heterostructures, AFM studies of the topography and moiré period of aligned heterostructures.

Convergent beam electron holography for analysis of van der Waals heterostructures

Tatiana Latychevskaia[1], Colin Robert Woods[2,3], Yi Bo Wang[2,3], Matthew Holwill[2,3], Eric Prestat[4], Sarah J. Haigh[2,4], Konstantin S. Novoselov[2,3]

[1]Institute of Physics, LUMES, École Polytechnique Fédérale de Lausanne (EPFL) , CH-1015 Lausanne, Switzerland

[2]National Graphene Institute, University of Manchester, Oxford Road, Manchester, M13 9PL, UK

[3]School of Physics and Astronomy, University of Manchester, Oxford Road, Manchester, M13 9PL, UK

[4]School of Materials, University of Manchester, Oxford Road, Manchester, M13 9PL, UK

Corresponding author:

Tatiana Latychevskaia (tatiana@physik.uzh.ch)

Kostya S. Novoselov (konstantin.novoselov@manchester.ac.uk)

Abstract

The Van der Waals heterostructures, which explore the synergetic properties of 2D materials when assembled into 3D stacks, have already brought to life a number of exciting new phenomena and novel electronic devices. Still, the interaction between the layers in such assembly, possible surface reconstruction, intrinsic and extrinsic defects are very difficult to characterise by any method, because of the single-atomic nature of the crystals involved. Here we present a convergent beam electron holographic technique which allows imaging of the stacking order in such heterostructures. Based on the interference of electron waves scattered on different crystals in the stack, this approach allows one to reconstruct the relative rotation, stretching, out-of-plane corrugation of the layers with atomic precision. Being holographic in nature, our approach allows extraction of quantitative information about the three-dimensional structure of the typical defects from a single image covering thousands of square nanometres. Furthermore, qualitative information about the defects in the stack can be extracted from the convergent diffraction patterns even without reconstruction – simply by comparing the patterns in different diffraction spots. We expect that convergent beam

electron holography will be widely used to study the properties of van der Waals heterostructures.

Significance statement

Assembling 2D materials into vertically stacked heterostructures allows an unprecedented control over their properties. The interaction between the individual crystals plays the crucial role here, thus, the information about the local atomic stacking is of great importance. Still, there are no techniques which would allow investigating the stacking between such crystals with any reasonable throughput. We present the use of convergent beam electron diffraction (CBED) to investigate the quality of the interface in such heterostructures. We demonstrate that defects such as crystallographic misorientation, strain, ripples, and others can be visualized and quantitative information about such structures can be easily extracted. Furthermore, CBED images can be treated as holograms, thus their reconstruction gives three-dimensional profiles of the heterostructures over a large area.

Main Text:

Stacking 2D materials into the van der Waals heterostructures offers an unprecedented control over the attributes of the resulting devices (1, 2). Initially the individual layers in the stack were considered to be independent, which, offers a reasonable zero-order approximation of the properties of such heterostructures. However, as we gain better and better control over the stacking arrangement between the individual components and the cleanliness of the interfaces – the interaction between the individual crystals becomes more and more important, and can even dominate the performance of the structures.

Still, it is very difficult to extract the detailed information about the stacking. Cross-sectional transmission electron microscopy (TEM) imaging (3) allows atomic scale information on the structure and chemistry of the buried interface between the individual crystals to be obtained. Unfortunately, this technique requires a sophisticated sample preparation, is time consuming, and only yields data on a thin slice of the sample, which is not necessarily representative for the large area device. Preferential scattering detection in the scanning TEM has been recently demonstrated to allow determination of atomic stacking for well-aligned graphene/boron nitride heterostructures, but it requires a custom aperture configuration and is based on atomic resolution imaging compared

with relaxed DFT modelling so is inherently limited to a small field of view (4). Thus, the whole field of van der Waals heterostructures would benefit enormously from a technique which allows one to extract three-dimensional structure of the buried interfaces inside such stacks on a larger scale.

Convergent beam electron diffraction (CBED) (5) has been previously applied to three-dimensional crystals where it provides a valuable method for studying crystallographic structure (6-9), measurements of strain (10, 11) and specimen thickness (12, 13) for a nanoscale volume. The choice of the electron beam convergence angle (14, 15), defocusing distance, lens aberrations and specimen thickness allow precise control of the volume of material analysed in a single measurement. However, accurate interpretation of a general CBED pattern is not straightforward, requiring careful comparison to simulated structures, which often limits application of the technique. CBED on thin van der Waals heterostructures (1, 2) would deliver a dramatically larger amount of information, which is intuitively easy to interpret and immediately results in both qualitative and quantitative data about the stack. Furthermore, CBED of van der Waals heterostructures can be considered as a hologram, so conventional holographic reconstruction techniques can be applied, thus delivering information about the three-dimensional arrangement between the crystals in the stack (including the local strain, lattice orientations, local vertical separation between the layers, *etc*.) which is not accessible by conventional TEM imaging (16, 17).

A CBED pattern from a single layer of graphene or hBN consists of finite-sized spots arranged into a six-fold symmetrical pattern. The centres of the spots have the same positions as the diffraction peaks, given by $\sin\vartheta = \lambda / a$, where λ is the wavelength, ϑ is the diffraction angle and a is the period of the crystallographic planes. The size of a CBED spot on the defector depends on the convergent angle and the diameter of the limiting aperture, and it remains the same independent of the z-position of the sample (or defocusing distance Δf). The sample area imaged within a CBED spot corresponds to the illuminated area, whose diameter can be approximated as $2\Delta f \tan\alpha$, where α is the convergence semi angle of the electron beam, Fig. 1a. Probing the samples by convergent (underfocus, $\Delta f < 0$) or divergent (overfocus, $\Delta f > 0$) incident wavefront is achieved by changing the z -position of the sample.

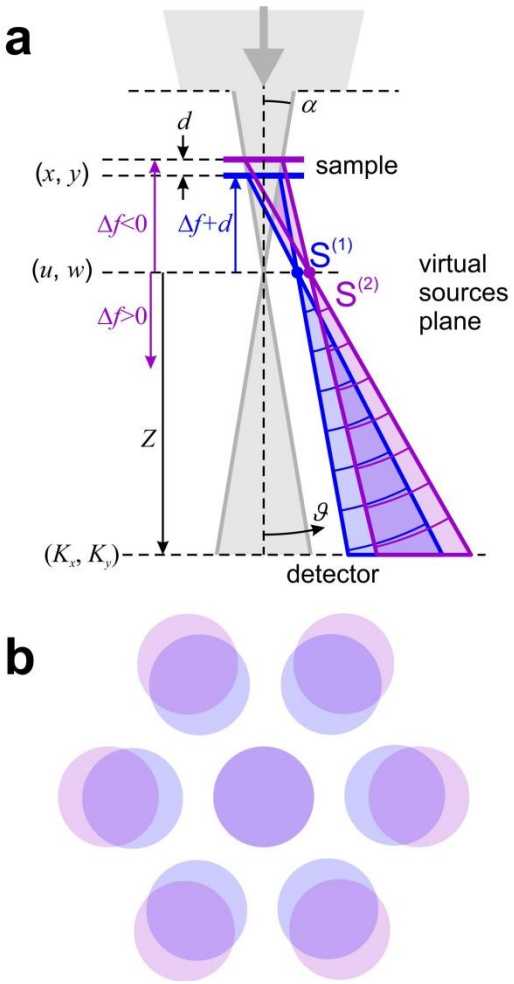

Fig. 1. Experimental arrangement for convergent beam electron diffraction. (a) Schematics of CBED on a bilayer system. Here Δf is the sample z-position counted from the focus of the electron beam (in this particular case underfocus $\Delta f < 0$ CBED conditions are shown), Z is the distance from the virtual sources plane to the detector, $S^{(1)}$ and $S^{(2)}$ are the virtual sources for the first-order CBED spots of bottom (1) and top (2) crystals in the heterostructure stack respectively. ϑ is the angular coordinate on the detector. (b) Distribution of CBED spots on a detector in the case of two aligned crystals with slightly different lattice constants.

In case of a CBED on a bilayer structure (for instance graphene/hBN stack – the type of devices we concentrate on in this paper), the electron beams diffracted on each layer interfere at the positions where the CBED patterns of individual layers overlap (Fig. 1b), thus creating a specific interference pattern (Fig. 2). Such interference patterns contain information about the local interatomic spacing (local strain), the vertical distance between the crystal layers, the relative orientation between the layers, etc.

Results

Simulated CBED of perfect crystals.

Fig. 2 demonstrates modelling of CBED for several typical bilayer heterostructures consisting of perfect crystals (the simulation procedure is described in Supporting Information). The interference pattern in a CBED spot can be interpreted as being created by a superposition of two waves originating from two corresponding virtual sources, as sketched in Fig. 1a. If the two stacked crystals have the same lattice constant and the same orientation (as, for instance, in the case of AA or AB stacked bilayer graphene) then the virtual spots are found almost at the same position, and no interference pattern is observed in CBED spots. A relative rotation between the layers (Fig. 2a – d), or a slight mismatch of the lattice constants (Fig. 2e – h), lead to the virtual sources, and correspondingly, the CBED spots, to appear at slightly different positions, Fig. 1b. As a result, the interference between the CBED spots occurs, and a fringed interference pattern is observed where the spots overlap. If the two graphene crystals in the double layer are rotated with respect to each other by a small angle β, the CBED patterns from the two crystals will be rotated relative to each other by the same angle. Diffracted electron waves, which originate from the separate layers, but arrive to the same point in the CBED detector plane, gain different phases, and the difference is now proportional to the rotation between the layers. As a result, radially distributed interference fringes will be observed, with the period of fringes within a particular CBED spot, dependent on the angle of the rotation between the layers, Fig. 2a – d.

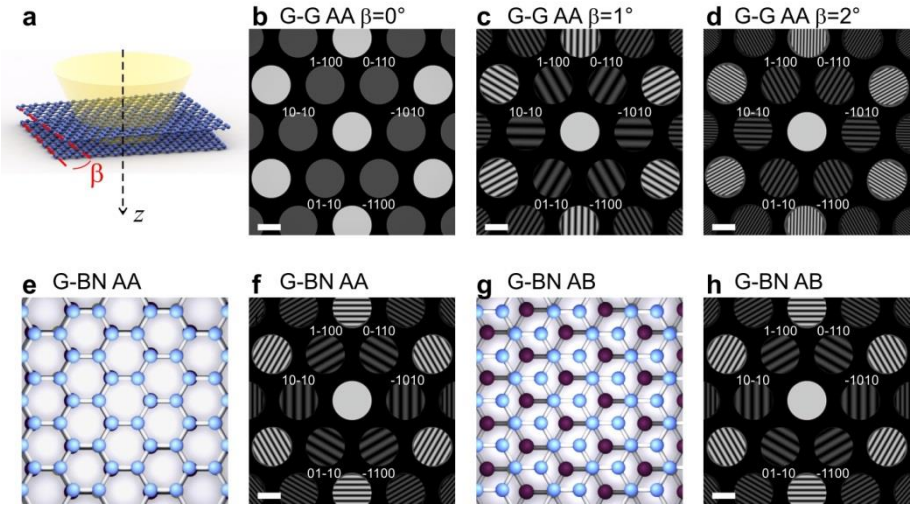

Fig. 2 Simulated CBED patterns for various 2D bilayer heterostructures. (a) Illustration of a bilayer graphene illuminated by a convergent electron beam with one graphene layer rotated by an angle β. (b) – (d) Simulated CBED patterns of a double layer graphene for different β. (e)

Sketch of the top view of a graphene-hBN stack with AA atomic stacking in the centre of the beam, and (f) the simulated CBED pattern. (g) Sketch of the top view of graphene-hBN with AB stacking in the centre of the beam, and (h) the simulated CBED pattern. For these simulations the distance between the layers is 3.35 Å, $\Delta f = -3\ \mu\text{m}$, and the imaged area is about 50 nm in diameter. (All scale bars correspond to 2 nm^{-1}.)

In the case of two crystals with aligned crystallographic directions but with slightly different interatomic spacing (as, for instance, the case for graphene and hBN) – the CBED spots will be shifted in the radial direction, Fig. 1b. hBN has a 1.8% larger basal plane lattice spacing than graphene and this will result in the appearance of an interference patterns with tangentially distributed fringes, Fig. 2e – h. The period and the tilt of the fringes are unambiguously defined by the lattices' periods, the probing electron beam wavelength, the z -position of the sample, the relative rotation between the layers, and the distance between the layers (as shown in Supporting Information). Interestingly, CBED patterns of such bilayer samples are extremely sensitive to the atomic arrangements in the layers. If the local stacking under the centre of the electron beam is AA (Fig. 2e) – the pattern of interference fringes has maxima at the centre of the CBED spots, Fig. 2f. If the local atomic stacking is AB (Fig. 2g) – the pattern of interference fringes in the CBED spots is shifted and as a result, the intensity distribution in the opposite CBED spots (such as 1-100 and -1100) are not mirror-symmetric, Fig. 2h.

Also the distance between the layers affects the interference pattern. The phase difference between the electron waves diffracted from the two identical and aligned crystals separated by a distance Δz is given by

$$\Delta\varphi_z = \Delta z \frac{2\pi}{\lambda}\left(1-\cos\vartheta\right), \tag{1}$$

where λ is the electron wavelength – 4.2 pm for 80 keV electrons. Since $\sin\vartheta = \frac{\lambda}{a}$, the phase shift within the CBED spot can be approximated as:

$$\Delta\varphi_z \approx \frac{\pi\lambda\Delta z}{a^2}, \tag{2}$$

where a is the lattice period which defines the order of the particular CBED spot. It is clear that for a bilayer graphene ($a = 2.13$ Å for the first-order CBED spots), with a typical interlayer distance of about 3.35 Å, the phase difference is negligible (about 0.1

rad) and remains almost constant over the entire CBED spot and thus no interference fringes should be observed within the CBED spots (as indeed has been reported previously (18)). Further discussion on the period of the interference fringes and examples of the reconstruction of the exact interlayer distances from CBED patterns are provided in Supporting Information.

We should stress that even in the case of a monolayer, the intensity distribution within each CBED spot is not an image of the sample but a far-field distribution of the intensity of the wave scattered by the sample, which in fact is an inline hologram of the sample area.

Simulated CBED for crystals with out-of-plane atomic displacements.

To quantitatively study the relation between the atomic defects and the CBED pattern we simulated out-of-plane and in-plane displacements of atoms in the graphene lattice and the corresponding phase distributions in the detector (far-field) plane, shown in Fig. 3. When atoms are displaced out of the crystal plane by a distance Δz, the scattered wave gains additional phase shift given by Eq. 1. Because $\Delta\varphi_z$ is an even function of ϑ, the added phase shift causes equal intensity change (increase or decrease of the intensity) in opposite CBED spots (see Supporting Information for the derivation of the formulae for the phase shift). A simulated CBED pattern of an out-of-plane defect (bubble, Fig. 3a) with a maximum height in the centre of 2 nm is presented in Fig. 3b, with the phase distribution in the far-field is shown in Fig. 3c. Formular 2 allows reconstruction of the shape of the bubble from the measured phase with 90% precision. The discrepancy is due to diffraction effects (which are strong for 4nm wide bubble) and assumed perfect coherence of the elctron beam. This Fresnel diffraction effect can be compensated, and the true shape of the bubble restored by performing deconvolution with the free-space propagator as explained in detail in Supporting Information. Such diffraction effects are much less pronounced in the experimental images where electron waves are only partially coherent, and where the use of formula (2) gives excellent level of accuracy.

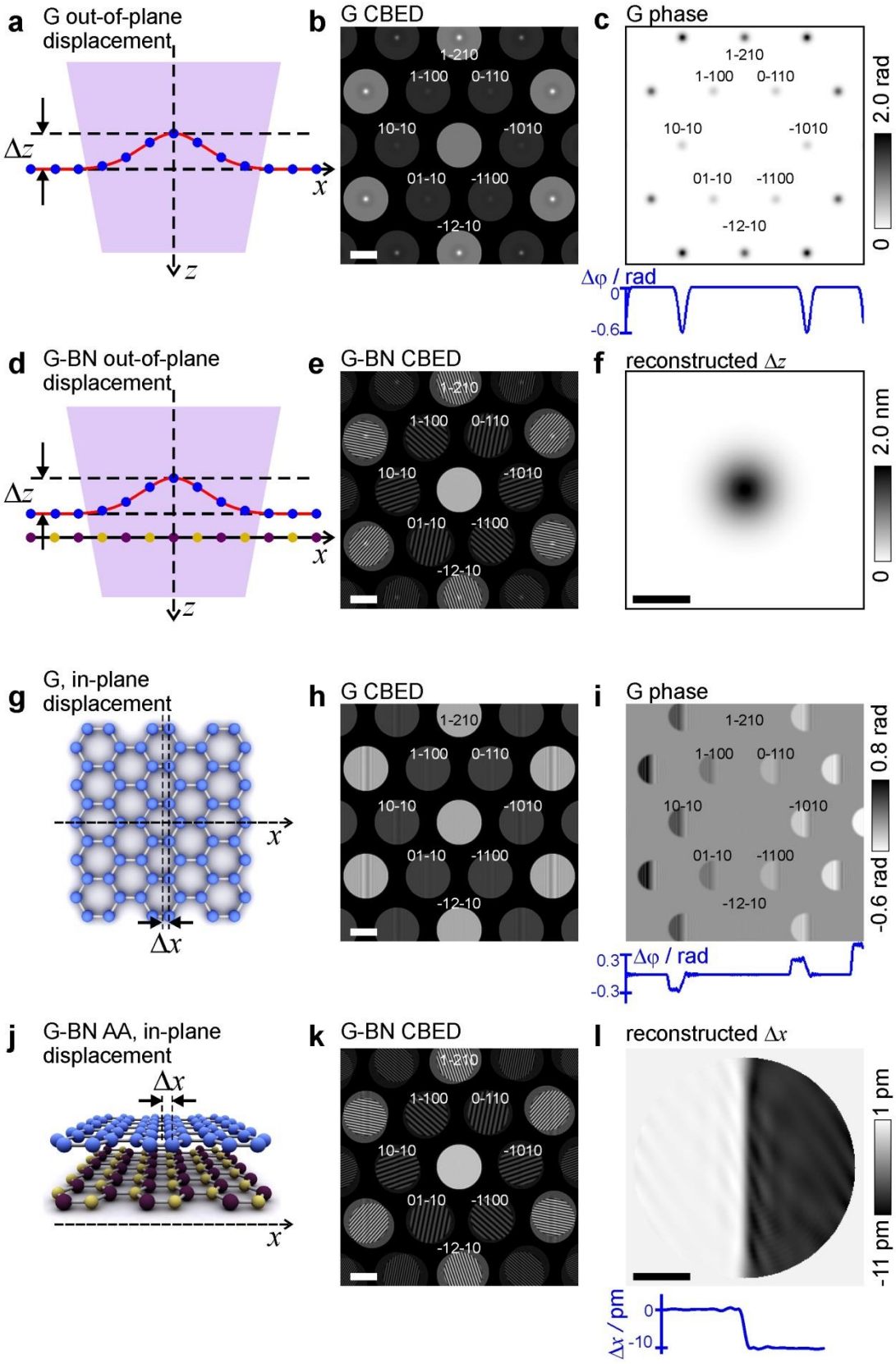

Fig. 3. Simulated CBED patterns for graphene and graphene-BN bilayer heterostructures where graphene lattice is deformed.

(a) Side view illustration of a graphene layer with atoms displaced out of plane, not drawn to scale.

(b) Corresponding simulated CBED pattern where the atoms are displaced out of plane in the form of a bubble. The atomic z -positions are shifted by $\Delta z = -A_{\mathrm{B}} \exp\left(-\frac{x^2+y^2}{2\sigma_{\mathrm{B}}^2}\right)$, $A_{\mathrm{B}} = 2$ nm, $\sigma_{\mathrm{B}} = 2$ nm.

(c) The difference of the phases of the wavefronts scattered by graphene with and without the out-of-plane atomic displacement due to the bubble. The blue curve shows the profile through the center of the distribution, that is at $K_y = 0$.

(d) Sketch of the side view of a graphene-BN bilayer with AA stacking area but with atoms in graphene displaced out of plane due to the presence of a bubble.

(e) Corresponding simulated CBED pattern for (d). The graphene atoms displacement same as in (b).

(f) Reconstructed distribution of the atomic out-of-plane displacement due to the bubble in the graphene layer. The scale bar corresponds to 5 nm.

(g) Sketch of the top view of the graphene layer with atoms displaced laterally (within the crystal plane).

(h) Simulated CBED pattern where the atoms positioned at $x > 0$ are displaced by $\Delta x = -10$ pm.

(i) The difference between the phases of the wavefronts scattered from graphene with and without in-plane atomic displacement. The blue curve shows the profile through the center of the distribution, that is at $K_y = 0$.

(j) Sketch of the side view of a graphene-BN bilayer, AA stacking area, with atoms in graphene displaced within graphene plane as in (h).

(k) Corresponding simulated CBED pattern for graphene-hBN heterostructures described in (j).

(l) Reconstructed distribution of the atomic in-plane Δx displacement in the graphene layer. The scale bar corresponds to 5 nm.

For these simulations the distance between the layers is 3.35 Å, $\Delta f = -2\ \mu\mathrm{m}$, and the imaged area is about 28 nm in diameter. The scale bars in (b), (e), (h) and (k) correspond to 2 nm^{-1}.

A CBED pattern of a monolayer contains only the amplitude information of the wave, losing the phase part of the signal. Consequently a direct recalculation of the CBED pattern into the atomic distribution is impossible. However, the CBED pattern intensity distribution unambiguously relates to the atomic three-dimensional displacements, and the atomic displacements in principle can be recovered by simulating a matching CBED pattern of a lattice with modelled displacements. The-situation is considerably improved

in the case of CBED of a bilayer system. Here, the second layer adds a second wavefront that acts as a reference wave. This situation can be considered as a form of an off-axis holography, where the wavefront, scattered on one of the crystals, is treated as the object wave, and the wavefront scattered on the other layer – as the reference wave. The resulting interference pattern forms an off-axis hologram, which can be reconstructed to give the amplitude and phase distributions of the wavefront at the position of each CBED spot. The reconstruction approach which we use here is based on an established procedure for reconstruction of off-axis holograms (19-21), and involves two Fourier transforms (22) (more details are provided in Supporting Information). From the set of the phase distributions recovered for individual CBED spots, the atomic displacements in the layers can be immediately recovered.

Fig. 3d shows a sketch of a bilayer graphene/hBN heterostructure with out-of-plane displacement of atoms in the graphene layer. The corresponding simulated CBED pattern is shown in Fig. 3e. An out-of-plane atomic displacement results in an additional phase shift, which is the same for all CBED spots of the same order. Thus, in order to extract the out-of-plane atomic displacements, the symmetric component of the CBED signal is extracted by averaging the phase distribution from all CBED spots of the same order, producing $\Delta\varphi_z$. Δz is calculated from $\Delta\varphi_z$ by applying Eq. 2, Fig. 3f.

Simulated CBED of crystals with in-plane atomic displacement.

When atoms are displaced within the crystal plane by a distance Δx the additional phase shift is given by

$$\Delta\varphi_x = -K_x \Delta x, \tag{3}$$

where $\left(K_x, K_y\right)$ are the coordinates in the far-field (detector) plane. Fig. 3g shows a sketch of graphene layer with an in-plane displacement $\Delta x = -10$ pm for the atoms in the positive semiplane ($x > 0$). The corresponding simulated CBED pattern is shown in Fig. 3h. Because the phase shift $\Delta\varphi_x$ is an odd function of K_x, an in-plane displacement give rise to opposite intensity variation in opposite CBED spots, as shown in Fig. 3h. As follows from Eq. 3, for $\Delta x = 10$ pm, the maximal phase shift in the first-order CBED spots amounts to ±0.3 radian, which is confirmed by the phase distribution shown in Fig. 3i. In Fig. 3i, vertical interference fringes observed in the centre of each CBED spots are

due to diffraction on a knife-edge. Because infinite coherence is assumed in the simulation, Fresnel fringes appear in the region of about $2.4\sqrt{\lambda\Delta f/2}$. Again, if we perform deconvolution with the free-space propagator (see Supporting Information) this Fresnel diffraction effect can be completely compensated. Such diffraction effects should be much less pronounced in experimental images where electron waves are only partially coherent.

According to Eq. 3, an in-plane displacement does not cause intensity variations (irregularities of fringes) in CBED spots that are orthogonal to the direction of the displacement (see no change in the intensity distributions in (1-210) and (-12-10) spots, Fig. 3h,i). In order to quantitatively reconstruct the in-plane atomic shifts in the x-direction, the difference between the phase distributions in the opposite CBED spots along the K_x-direction should be calculated and divided by 2, thus extracting only the antisymmetric component of the signal. Δx is then calculated from $\Delta\varphi_x$ by applying Eq. 3.

Fig. 3j shows a sketch of a graphene/hBN hetrostructure with atomic in-plane displacement of some of graphene atoms (the whole right semiplane is shifted by 10 pm). The corresponding simulated CBED pattern is shown in Fig. 3k. The phase distributions were reconstructed for each CBED spot, and Δx was obtained from the reconstructed phase distributions as described above. Fig. 3l shows the reconstructed Δx which matches the pre-defined values: 0 for $x<0$ and -10 pm for $x>0$. An example of reconstruction when both Δx and Δz occur simultaneously with more details about the reconstruction procedure, is provided in Supporting Information.

As one can see, it is easy to distinguish between the out-of-plane and in-plane atomic displacements even without performing a reconstruction by simply comparing the intensity contrast in the opposite CBED spots of monolayers or the regularity of interference fringes for bilayer samples. An out-of-plane defect will always result in a symmetric phase distribution between the mirror-symmetric CBED spots, and an in-plane defect – in an antisymmetric one.

Experimental results.

Fig. 4 shows CBED patterns for three of our samples: aligned graphene on hBN (Fig. 4a), graphene rotated with respect to hBN by a small angle (Fig. 4b), and a multilayered sample (Fig. 4c). As predicted by the simulations (Fig. 2), the interference patterns are tangential and radial in Fig. 4a and Fig. 4b respectively. The particular arrangement of the interference patterns (for instance, the number of interference fringes) depends on Δf as well as the misorientation angle between the two crystals, among other parameters. The misorientation angle calculated for this particular sample is 2.5°±0.1° (see Supporting Information). More examples of experimental CBED patterns for graphene-hBN heterostructures are provided in Supporting Information.

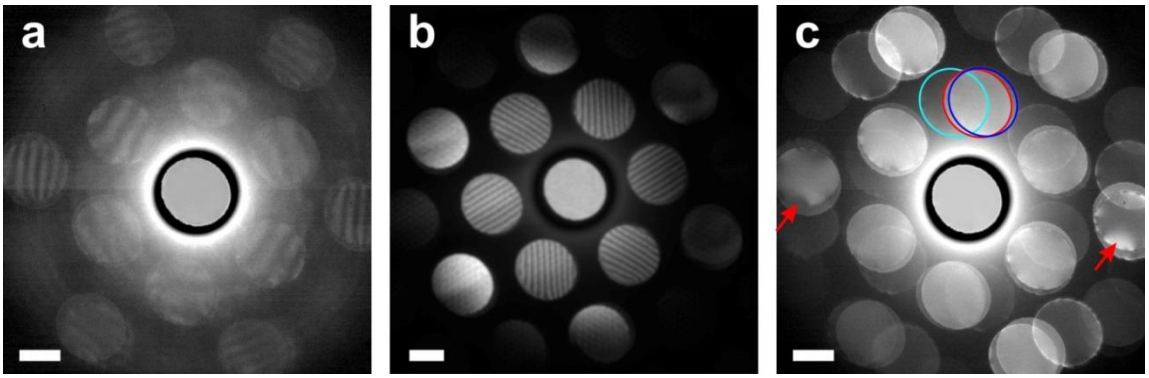

Fig. 4. Experimental CBED patterns of graphene-hBN samples. (a) CBED pattern where the direction of fringes indicates that there is almost no relative rotation between the layers, $\Delta f = -5$ μm, $\alpha = 6.93$ mrad, which gives the diameter of the imaged area of about 70 nm. (b) CBED pattern of another sample where the direction of fringes indicate a relative rotation between the layers, $\beta = 2.5°$, $\Delta f = -3$ μm, $\alpha = 8.023$ mrad, which gives the diameter of the imaged area of about 48 nm. (c) CBED pattern of graphene/hBN/graphene heterostructure sample, $\Delta f \approx 0$, $\alpha = 8.023$ mrad, the diameter of the imaged area is about 1 nm (more information on the distribution of the probing wavefront is provided in Supporting Information). The intensity of the central spot is reduced by factor 0.002 in (a), 0.1 in (b) and 0.005 in (c). The scale bars are 2 nm^{-1}.

Figure 4c shows a CBED pattern of a three layers system (hBN sandwiched between two layers of graphene) acquired at $\Delta f \approx 0$. Because Δf is so small, the period of the interference fringes is very large and no interference fringes are observed within the overlapping CBED spots. From the position of the spots, we measure that the relative rotation between hBN and one of the graphene layers is 2.5°, and the relative rotation between the two graphene layers is 17°. Two of the three layers exhibit unperturbed

crystalline structure as evident from the homogeneous intensity within their CBED spots. The intensity variations of opposite contrast in opposite CBED spots of the hBN layer indicate the presence of an in-plane strain (as indicated by the red arrows in Fig. 4c). The contrast variation on the circumference of each CBED discs in Fig. 4 and 5 are attributed to charging of the dust particles at the condenser aperture.

To demonstrate the holographic nature of our CBED patterns, we imaged a ripple defect in stacking between the two layers. Such defects are often associated with basal plane dislocations and have also been referred to as ripplocations (23). Fig. 5a presents a CBED pattern from an area with a stacking fault between slightly misoriented graphene and hBN, which is evident by the presence of a distinctive ridge in the interference patterns in the first- and higher-order CBED spots (see also Fig. 5b). We note that no features are visible in the zero-order spot, suggesting that the defect induces only marginal additional absorption. However, this defect introduces a significant additional phase shift between the electron waves scattered from the top and bottom crystals, which is readily picked up in the CBED interference patterns. If it were not for this interference, quantitative imaging of such a defect would be next to impossible. CBED spots which originate from graphene are found at a slightly larger diffraction angle allowing differentiation of the spots corresponding to graphene from those for hBN. The overlap between CBED spots from the two crystals is less in the higher diffraction orders but the intensity contrast due to corrugation is more pronounced in the higher order CBED spots. Thus, by visual inspection of the high-order CBED spots, the type of corrugation and the layer with the corrugation can be readily identified. For example, in the CBED pattern shown in Fig. 5a, the ripple marked by the cyan arrows in Fig. 5a (also in magnified image in Fig. 5b) manifests itself identically in all the higher-order CBED spots, which suggests that this is an out-of plane ripple. Also, it is clearly seen in the third-order CBED spots, where the spots from hBN and graphene are sufficiently separated (as indicated by the yellow arrows in Fig. 5a), that the projection of the ripple exists only in one of the spots (hBN), unambiguously identifying the corrugated layer.

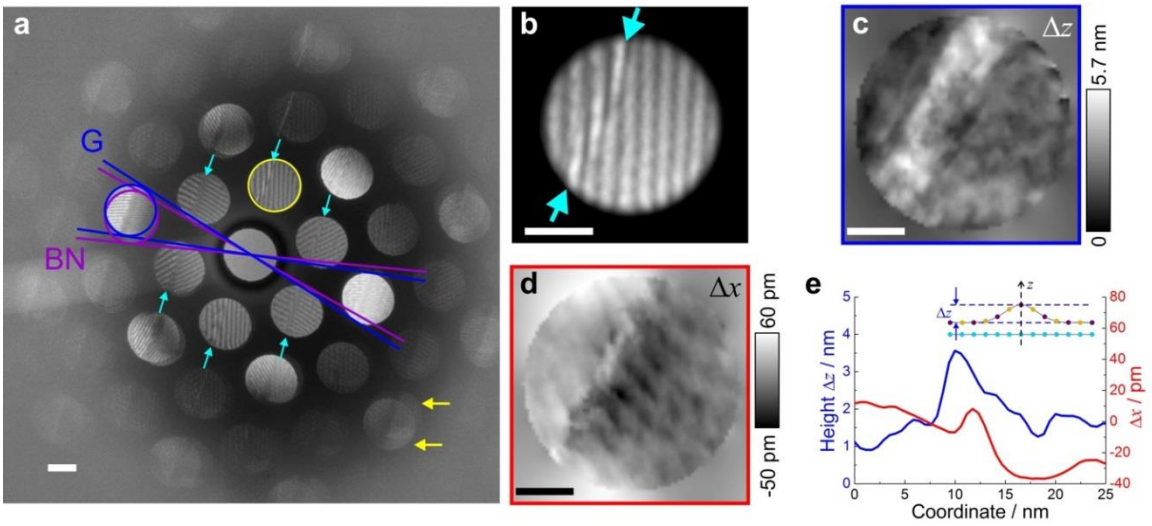

Fig. 5. Extracting the shape of the out-of-plane ripple from a CBED pattern. (a) Experimental CBED pattern acquired at $\Delta f = -3$ μm, with defects in the interference patterns marked by the arrows. The blue and purple lines indicate the relative rotation between graphene and hBN layers, which amounts to 3°. The cyan arrows indicate an out-of-plane ripple observed in the first-order CBED spots. The yellow arrows indicate the separation of CBED spots originating from graphene and hBN layers, where it becomes clear that the ripple is in the hBN layer. The intensity of the central spot is reduced by a factor of 0.1. The scale bar corresponds to 2 nm^{-1}. (b) Magnified selected spot (circled in (a)) where irregularities of the fringe pattern can be seen. The scale bar corresponds to 1 nm^{-1}. (c) The reconstructed distribution of the ripple height Δz. (d) The reconstructed distribution of the lateral shift Δx. (e) Profiles for the magnitude of Δz and Δx profiles perpendicular to the ripple in (c) and (d). The scale bars in (c) and (d) correspond to 10 nm in real space.

To extract quantitative information about the defect we performed holographic reconstruction of the CBED pattern image presented in Fig. 5a as described above. The phase unwrapping was applied by using a procedure introduced by Schofield and Zhu (24). Fig. 5c shows the recovered out-of-plane Δz atomic displacements obtained from symmetric component of the CBED picture by averaging the reconstructed phase distributions from all six first-order CBED spots and applying Eq. 1. Fig. 5d shows the recovered in-plane Δx atomic displacements obtained by extracting the antisymmetric component of the phase distribution from two opposite first-order CBED spots and by applying Eq. 3. Fig. 5e compares the out-of-plane and in-plane atomic shifts along the ripple. In our case the retrieved height of the out-of-plane ripple in BN layer is about 2

nm. This is reasonable, since out of plane ripples are often observed for graphene/hBN stacks due to self-cleansing effects (25).

Discussion

We demonstrated that single CBED pattern of van der Waals heterostructures allows for a direct visualization of a three-dimensional atomic distribution in each individual layer. Even without reconstruction, qualitative information about the type (stretching or out-of-plane rippling) and the extent of lattice deformation can be directly obtained by simple comparison of intensities distributions in the opposite CBED spots. For bilayer materials, a holographic approach can be applied to quantitatively reconstruct the values of three-dimensional atomic displacements.

The resolution provided with our technique depends on the size of the imaged area, that is, on Δf and the corresponding magnification. To evaluate the sensitivity of our method to atomic shifts we estimate that a phase shift of 0.1 rad is sufficient to cause detectable variations in intensity distribution. Such a phase shift can be caused by out-of-plane atomic shifts of $\Delta z \approx 0.35$ nm or by an in-plane atomic shift of $\Delta x \approx 3.4$ pm (in accordance to Eq. 2 and Eq. 3). Thus, the sensitivity to in-plane atomic displacements is about 100 times higher than the sensitivity to out-of-plane displacements. The sensitivity to spatial position is of the order of 1 nm when the location of atomic displacements are obtained by comparing intensity distributions from the opposite CBED spots and is a few nanometers when the holographic reconstruction is applied (as discussed in Supporting Information).

Quantitative information in the z direction (parallel to the electron beam) is notoriously difficult to obtain from a projection imaging technique such as transmission electron microscopy. Thus the ability to obtain quantitative information about the relative location of the atomic sheets in the z-direction is one of the strengths of our approach. Furthermore, our approach does not require any special sample preparation – it can be applied to any samples being observed in TEM in traditional modes. Classical electron tomography methods used to gain three-dimensional positional data struggle except when the target is a perfectly crystalline nano-object that can be imaged along several zone axes (26). Van Dyck et al have demonstrated that atomic resolution three-

dimensional coordinates could be achieved from only a single projection using a combination of exit wave reconstruction from a focal series of images and a "Big Bang" analysis of the quantitative phase shift for individual atomic columns (27). Their approach requires a sequence of atomically resolved high-resolution images (to recover the complex-valued exit wave which is a complicated analysis by itself) and only obtains a single z-location for each atom column position. By contrast our approach gains high resolution z-positional data on the relative position of the two separate layers from a *single* CBED pattern. Although currently the lateral resolution we obtain is poorer than that demonstrated by Van Dyck et al, our approach requires orders of magnitude lower electron exposures so it has a potential to be applied to heterostructures containing beam-sensitive 2D materials and even overlapping protein membranes. In addition, our approach can be further advanced by obtaining many CBED patterns to reconstruct a large area (diffractive imaging). Also, depending on Δf, the area studied by our approach can be tuned from gaining sensitive relative atomic displacements for just a few nm^2, to regions ~1 μm wide, as is typical of the active area of lithographically patterned 2D heterostructure devices.

Our results demonstrate that CBED on van der Waals heterostructures can be applied to yield a plethora of information about the stacks. This technique has not previously been applied to van der Waals heterostuctures but we have shown that it is highly versatile and as it can be performed on any conventional TEM instrumentation. We expect that this approach will find a progressive use in the expanding field of 2D materials. Furthermore it could be extended to the analysis of dopant atoms, local oxidation or trapped species within the heterostructures, as all of these will affect the interference patterns obtained.

Materials and Methods

The samples were obtained by mechanical stacking of mechanically exfoliated graphene and hBN layers on a Si/SiO_2 substrate. By using “pick and lift” technique (28) - the whole stack was then transferred on a quantifoil carbon support film for observation in the TEM. CBED was realized in a probe side aberration corrected scanning TEM at an accellerating voltage of 80 keV and a convergence semi angle, α, of ~6 – 8 mrad. During experiment, the focal lengths of the objective and condenser lenses were kept constant, thus there was no change in the convergence angle. The sample *z*-position was

changed by moving the sample along the optical axis. Bilayer structure significantly improves the stability of 2D crystals upon exposure to high-energy electrons and the electron dose required for CBED imaging is low, so no evidence of knock-on damage was observed during prolonged data acquisition (29, 30).

Acknowledgements

This work was supported by the EU Graphene Flagship Program, European Research Council Synergy Grant Hetero2D, and EvoluTEM Starter Grant, the Royal Society, Engineering and Physical Research Council (UK), US Army Research Office (W911NF-16-1-0279). S.J.H and E.P. acknowledge funding from the Defense Threat Reduction Agency (grant HDTRA1-12-1-0013) and the Engineering and Physical Sciences Research Council (UK) (grants EP/K016946/1, EP/L01548X/1, EP/M010619/1 and EP/P009050/1).

References

1. Geim AK & Grigorieva IV (2013) Van der Waals heterostructures. *Nature* 499(7459):419-425.
2. Novoselov KS, Mishchenko A, Carvalho A, & Castro Neto AH (2016) 2D materials and van der Waals heterostructures. *Science* 353(6298):aac9439-aac9439.
3. Haigh SJ, *et al.* (2012) Cross-sectional imaging of individual layers and buried interfaces of graphene-based heterostructures and superlattices. *Nat. Mater.* 11(9):764–767.
4. Argentero G, *et al.* (2017) Unraveling the 3D Atomic Structure of a Suspended Graphene/hBN van der Waals Heterostructure. *Nano Lett.* 17(3):1409-1416.
5. Kossel W & Möllenstedt G (1939) Elektroneninterferenzen im konvergenten Bündel. *Ann. Phys.* 36:113.
6. Goodman P (1975) A practical method of three-dimensional space-group analysis using convergent-beam electron diffraction. *Acta Crystallogr. Sect. A* 31(6):804–810.
7. Buxton BF, Eades JA, Steeds JW, & Rackham GM (1976) The symmetry of electron diffraction zone axis patterns. *Philos. Trans. Royal Soc. A* 281(1301):171–194.

8. Tanaka M, Sekii H, & Nagasawa T (1983) Space-group determination by dynamic extinction in convergent-beam electron diffraction *Acta Crystallogr. Sect. A* 39(NOV):825–837.
9. Tanaka M, Saito R, & Sekii H (1983) Point-group determination by convergent-beam electron diffraction. *Acta Crystallogr. Sect. A* 39(MAY):357–368.
10. Jones PM, Rackham GM, & Steeds JW (1977) Higher-order Laue zone effects in electron-diffraction and their use in lattice-parameter determination. *Proc. R. Soc. London Ser. A-Math. Phys. Eng. Sci.* 354(1677):197-222.
11. Carpenter RW & Spence JCH (1982) Three-dimensional strain-field information in convergent beam electron diffraction patterns. *Acta Crystallogr. Sect. A* 38(JAN):55–61.
12. Kelly PM, Jostsons A, Blake RG, & Napier JG (1975) The determination of foil thickness by scanning transmission electron microscopy. *physica status solidi (a)* 31(2):771–780.
13. Champness PE (1987) Convergent beam electron diffraction. *Mineral. Mag.* 51(359):33–48.
14. Tanaka M, Saito R, Ueno K, & Harada Y (1980) Large-angle convergent-beam electron diffraction. *J. Electron Microsc.* 29(4):408–412.
15. Morniroli JP (2006) CBED and LACBED characterization of crystal defects. *J. Microsc.-Oxf.* 223:240–245.
16. Gabor D (1948) A new microscopic principle. *Nature* 161(4098):777–778.
17. Gabor D (1949) Microscopy by reconstructed wave-fronts. *Proc. R. Soc. A* 197(1051):454–487.
18. Meyer JC, *et al.* (2007) On the roughness of single- and bi-layer graphene membranes. *Solid State Communications* 143(1-2):101-109.
19. Leith EN & Upatnieks J (1962) Reconstructed wavefronts and communication theory. *J. Opt. Soc. Am.* 52(10):1123–1130.
20. Leith EN & Upatnieks J (1963) Wavefront reconstruction with continuous-tone objects. *J. Opt. Soc. Am.* 53(12):1377–1381.
21. Mollenstedt G & Wahl H (1968) Electron holography and reconstruction with laser light. *Naturwissenschaften* 55(7):340–341.
22. Lehmann M & Lichte H (2002) Tutorial on off-axis electron holography. *Microsc. Microanal.* 8(6):447–466.

23. Kushima A, Qian X, Zhao P, Zhang S, & Li J (2015) Ripplocations in van der Waals Layers. *Nano Lett.* 15(2):1302-1308.
24. Schofield MA & Zhu YM (2003) Fast phase unwrapping algorithm for interferometric applications. *Opt. Lett.* 28(14):1194–1196.
25. Kretinin AV, *et al.* (2014) Electronic properties of graphene encapsulated with different two-dimensional atomic crystals. *Nano Lett.* 14(6):3270-3276.
26. Van Aert S, Batenburg KJ, Rossell MD, Erni R, & Van Tendeloo G (2011) Three-dimensional atomic imaging of crystalline nanoparticles. *Nature* 470:374–377.
27. Van Dyck D & Chen F-R (2012) 'Big Bang' tomography as a new route to atomic-resolution electron tomography. *Nature* 486(7402):243–246.
28. Wang L, *et al.* (2013) One-dimensional electrical contact to a two-dimensional material. *Science* 342(6158):614-617.
29. Zan R, *et al.* (2013) Control of radiation damage in MoS2 by graphene encapsulation. *ACS Nano* 7(11):10167-10174.
30. Algara-Sillera G, Kurascha S, Sedighi M, Lehtinen O, & Kaiser U (2013) The pristine atomic structure of MoS2 monolayer protected from electron radiation damage by graphene. *Appl. Phys. Lett.* 103(20):203107.

Supplementary

S1. CBED pattern of an edge

CBED patterns shown in Fig. S1 demonstrate how the interference pattern disappears when part of one of the layers is missing. Note that in the simulated images, where infinite coherence is assumed, the diffraction causes interference pattern to be continued into the regions where there is no second layer, Fig. S1b. In the experimental images, due to partial coherence of electron waves, the edge of the layer appears almost sharp without noticeable diffraction effects.

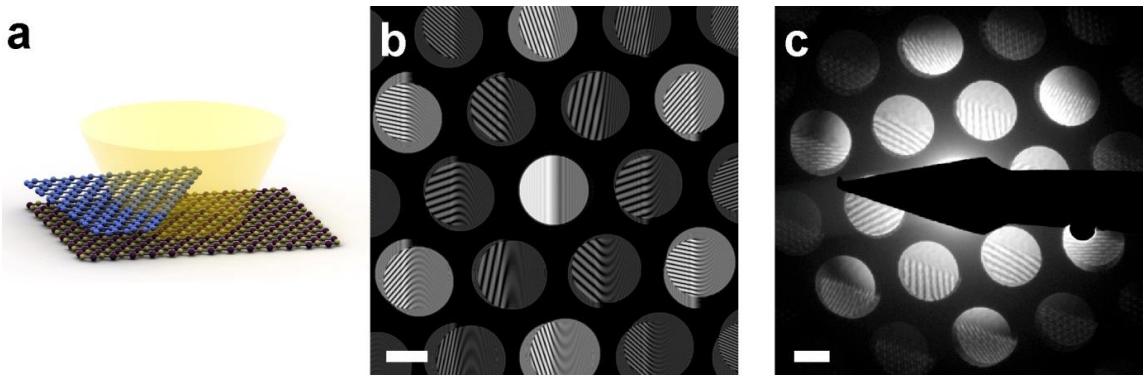

Fig. S1. Simulated and experimental CBED pattern of a graphene-BN sample at the edge of one layer. (a) Illustration of experimental arrangement. (b) Simulated CBED pattern. For these simulations the distance between the layers is 3.35 Å, $\Delta f = -2$ μm, and the imaged area is about 28 nm in diameter. (c) Experimental CBED pattern. The scale bars in (c) and (d) correspond to 2 nm^{-1}.

S2. Origin of rippling

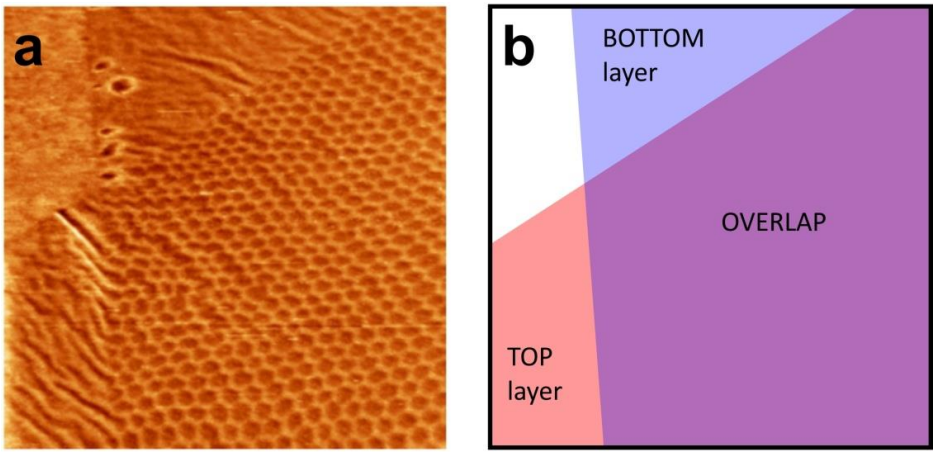

Fig. S2. (a) Topographic image of a monolayer-hBN (mhBN) on graphene sample on SiO_2. The size of the scan is 400 nm. Z-contrast (from black to white): 6 nm. (b). Cartoon illustrating 4 regions formed by the overlapping layers in (a).

Even though we only extract the relative information between the layers – we still can know the particular layer which contains the ripple due to specific sample preparation procedure. Here we used the pick and lift method. This involves exfoliating graphene onto a PMMA substrate and the hBN onto a SiO_2 substrate. Then, the PMMA is used as a membrane to suspend the graphene over the hBN crystal as the two are brought into contact. The crystals adhere and the membrane is lifted again with the two crystals attached. The two crystals are then positioned over a hole in the TEM grid and brought into contact with it. The PMMA is then removed with acetone.

We anticipate that the PMMA is ultimately responsible for the rippling of the crystal exfoliated onto it, perhaps as a result of uneven drying when the polymer layer is spin-coated. This is corroborated by the sample in the figure above. Fig. S2 shows topography image of monolayer-hBN (mhBN) on graphene sample on SiO_2. Four distinct regions are present in the image; SiO_2 only (top left), graphene on SiO_2 (top right), mhBN on SiO_2 (bottom left), and mhBN on graphene on SiO_2 (bottom right). The angular dependant moiré pattern is clearly visible in the overlap regions. However, also observable is that there is a large amount of rippling in the mhBN flake. This suggests the PMMA introduces (or allows) significant amounts of wrinkling into the crystal in contact with it.

S3. Alternative methods of observing defects in graphene/hBN heterostructures

CBED is uniquely positioned for the observation of atomic scale defects in van der Waals heterostructures. However, here we made an attempt of independent verification of our CBED observation. We used AFM to investigate the same area we observed in TEM. We would like to point out that AFM would be sensitive only to certain types of defects (like out-of-plane ripples) and would be completely insensitive to such defects as in-plane ripples, local strain, etc – which are still observable by CBED.

The AFM image of approximately the same region as we observed in TEM is presented in Fig. S3. We would like to point out that it is very difficult to identify the exact region we observed in TEM: our membranes are few micrometre in diameter and the region we observe in CBED is few tens of nanometres. The AFM image demonstrates surface with high roughness (~1nm), which is probably due to residual contamination acquired through the transfer process (wet transfer is usually used for transfer of van der Waals heterostructures on TEM grids) and a contamination layer due to exposure to the electron beam.

Also, we observed linear defects, which might be identified as ripples. Their height is a few nanometres, similar to the ripples heights reconstructed from CBED patterns. We would like to stress, that the information obtained by AFM cannot allow us to be more conclusive about the nature of the defects. It is only possible to say that the AFM observation is in agreement with our CBED finding. Note, our AFM study doesn't provide any information on the width of the ripple as an AFM image is always a convolution between the shape of the ripple and the shape of the AFM tip.

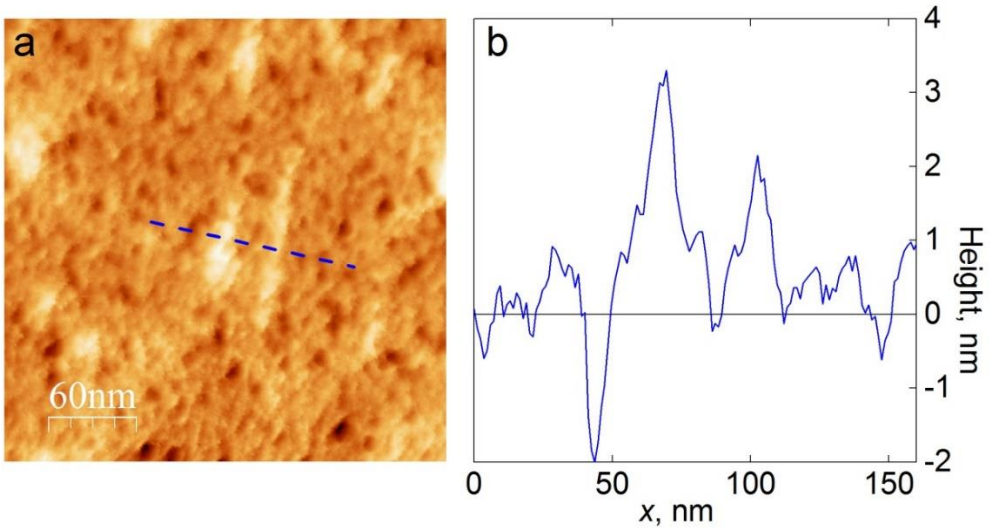

Fig. S3. AFM investigation of the atomic scale defects in van der Waals heterostructures. (a) Topographic image of the same graphene-hBN sample and approximately the same spot as observed in Fig. 5 in the main text. Linear defects which can be ripples are visible. (b) Cross-section of (a) along the dashed blue line.

References

1. Castro Neto, A. H., Guinea, F., Peres, N. M. R., Novoselov, K. S. & Geim, A. K. The electronic properties of graphene. *Rev. Mod. Phys.* **81**, 109–162 (2009).

2. Smalley, R. GREAT BALLS OF CARBON: The Story of Buckminsterfullerene. *Sciences (New. York).* **31**, 22–28 (1991).

3. Geim, A. K. & Novoselov, K. S. The rise of graphene. *Nat. Mater.* **6**, 183–91 (2007).

4. Iijima, S. & Ichihashi, T. Single-shell carbon nanotubes of 1-nm diameter. *Nature* **363**, 603–605 (1993).

5. Novoselov, K. S. *et al.* Electric field in atomically thin carbon films. *Science* **306**, 666–669 (2004).

6. Peierls, R. Quelques propriétés typiques des corps solides. *Ann. l'institut Henri Poincaréfile* **3**, 177–222 (1935).

7. Münster, A. Über eine allgemeine Theorie der Phasenumwandlungen. *Zeitschrift für Elektrochemie und Angew. Phys. Chemie* **55**, 593–597 (1951).

8. Müller, B., Nedelmann, L., Fischer, B., Brune, H. & Kern, K. Initial stages of Cu epitaxy on Ni(100): Postnucleation and a well-defined transition in critical island size. *Phys. Rev. B-Condens. Matter Mater. Phys.* **54**, 17858–17865 (1996).

9. Frank, S. *et al.* Approaching the low-temperature limit in nucleation and two-dimensional growth of fcc (100) metal films Ag/Ag(100). *Phys. Rev. B* **66**, 155435 (2002).

10. Venables, J. A., Spiller, G. D. T., Hanbucken, M. Nucleation and Growth of Thin Films. *Rep. Prog. Phys.* **47**, 399–495 (1984).

11. Evans, J. W., Thiel, P. A. & Bartelt, M. C. Morphological evolution during epitaxial thin film growth: Formation of 2D islands and 3D mounds. *Surf. Sci. Rep.* **61**, 1–128 (2006).

12. Venable, J. A., Spiller, G. D. T. & Hanbucken, M. Nucleation and growth of thin

film. *Rep. Prog. Phys.* **47**, 399–459 (1984).

13. Meyer, J. C. *et al.* The structure of suspended graphene sheets. *Nature* **446**, 60–63 (2007).

14. Stankovich, S. *et al.* Graphene-based composite materials. *Nature* **442**, 282–286 (2006).

15. Geim, A. K. Graphene : Status and Prospects. *Science* **324**, 1530–1534 (2009).

16. Novoselov, K. S. *et al.* A roadmap for graphene. *Nature* **490**, 192–200 (2012).

17. Mayorov, A. S. *et al.* Micrometer-scale ballistic transport in encapsulated graphene at room temperature. *Nano Lett.* **11**, 2396–2399 (2011).

18. Balandin, A. A. Thermal properties of graphene and nanostructured carbon materials. *Nat. Mater.* **10**, 569–581 (2011).

19. Moser, J., Barreiro, A. & Bachtold, A. Current-induced cleaning of graphene. *Appl. Phys. Lett.* **91**, 3–6 (2007).

20. Torres, L. E. F. F., Roche, S. & Charlier, J.-C. *Introduction to graphene-based nanomaterials: from electronic structure to quantum transport*. 11-17 (Cambridge University Press, 2014).

21. Kevin, M. & Boudreaux, A. *General Chemistry Chemistry: The Science in Context.* 10-15 (Gilbert, 4 th. (2015).

22. Tilley, R. J. D. *Crystals and crystal structures*. 20-27 (John Wiley & Sons, 2006).

23. Reich, S., Maultzsch, J., Thomsen, C. & Ordejón, P. Tight-binding description of graphene. *Phys. Rev. B* **66**, 035412 (2002).

24. Wallace, P. R. The band theory of graphite. *Phys. Rev.* **71**, 622–634 (1947).

25. Yi, M. & Shen, Z. A review on mechanical exfoliation for the scalable production of graphene. *J. Mater. Chem. A* **3**, 11700–11715 (2015).

26. Novoselov, K. S., Mishchenko, A., Carvalho, A. & Castro Neto, A. H. 2D materials and van der Waals heterostructures. *Science* **353**, (2016).

27. Frank, O. & Kalbac, M. Chemical vapor deposition (CVD) growth of graphene films. *Graphene Prop. Prep. Characterisation Devices* **2**, 27–49 (2014).

28. Bae, S. *et al.* 30 inch Roll-Based Production of High-Quality Graphene Films for Flexible Transparent Electrodes. **5**, 1–5 (2009).

29. Bae, S. *et al.* Roll-to-roll production of 30-inch graphene films for transparent electrodes. *Nat. Nanotechnol.* **5**, 574–578 (2010).

30. Huang, P. Y. *et al.* Grains and grain boundaries in single-layer graphene atomic patchwork quilts. *Nature* **469**, 389–392 (2011).

31. Yan, Z., Peng, Z. & Tour, J. M. Chemical Vapor Deposition of Graphene Single Crystals. *Acc. Chem. Res.* **47**, 1327–1337 (2014).

32. Ruiz-Vargas, C. S. *et al.* Softened Elastic Response and Unzipping in Chemical Vapor Deposition Graphene Membranes. *Nano Lett.* **11**, 2259–2263 (2011).

33. Yu, Q. *et al.* Control and characterization of individual grains and grain boundaries in graphene grown by chemical vapour deposition. *Nat. Mater.* **10**, 443–449 (2011).

34. Yan, Z. *et al.* Toward the Synthesis of Wafer-Scale Single-Crystal Graphene on Copper Foils. *ACS Nano* **6**, 9110–9117 (2012).

35. Wu, T. *et al.* Triggering the Continuous Growth of Graphene Toward Millimeter-Sized Grains. *Adv. Funct. Mater.* **23**, 198–203 (2013).

36. Petrescu, M. I. & Balint, M. G. Structure and properties modifications in boron nitride. part II: Hardness modification induced by the polymorphic transformations. *UPB Sci. Bull. Ser. B Chem. Mater. Sci.* **69**, 43–52 (2007).

37. Dean, C. R. *et al.* Boron nitride substrates for high-quality graphene electronics. **5**, 722–726 (2010).

38. Dean, C. R. *et al.* Boron nitride substrates for high-quality graphene electronics. *Nat. Nanotechnol.* **5**, 722–726 (2010).

39. Boron nitride as solid lubricant [SubsTech]. Available at: https://www.substech.com/dokuwiki/doku.php?id=boron_nitride_as_solid_lubrica

nt.

40. Wang, J., Ma, F. & Sun, M. Graphene, hexagonal boron nitride, and their heterostructures: properties and applications. *RSC Adv.* **7**, 16801–16822 (2017).

41. Ando, T. Screening Effect and Impurity Scattering in Monolayer Graphene. *J. Phys. Soc. Japan* **75**, 074716 (2006).

42. Chen, J.-H., Jang, C., Xiao, S., Ishigami, M. & Fuhrer, M. S. Intrinsic and extrinsic performance limits of graphene devices on SiO2. *Nat. Nanotechnol.* **3**, 206–209 (2008).

43. Morozov, S. V. *et al.* Giant Intrinsic Carrier Mobilities in Graphene and Its Bilayer. *Phys. Rev. Lett.* **100**, 016602 (2008).

44. Wang, Q. H., Kalantar-Zadeh, K., Kis, A., Coleman, J. N. & Strano, M. S. Electronics and optoelectronics of two-dimensional transition metal dichalcogenides. *Nat. Nanotechnol.* **7**, 699–712 (2012).

45. Radisavljevic, B., Radenovic, A., Brivio, J., Giacometti, V. & Kis, A. Single-layer MoS2 transistors. *Nat. Nanotechnol.* **6**, 147–50 (2011).

46. Coleman, J. N. *et al.* Coleman2011.Pdf. *Science* **331**, 568–571 (2011).

47. Smith, R. J. *et al.* Large-Scale Exfoliation of Inorganic Layered Compounds in Aqueous Surfactant Solutions. *Adv. Mater.* **23**, 3944–3948 (2011).

48. Li, X. *et al.* Large-Area Synthesis of High-Quality and Uniform Graphene Films on Copper Foils. *Science* **324**, 1312–1314 (2009).

49. Hass, J., de Heer, W. A. & Conrad, E. H. The growth and morphology of epitaxial multilayer graphene. *J. Phys. Condens. Matter* **20**, 323202 (2008).

50. Lee, Y.-H. *et al.* Synthesis of Large-Area MoS_2 Atomic Layers with Chemical Vapor Deposition. *Adv. Mater.* **24**, 2320–2325 (2012).

51. Zhan, Y., Liu, Z., Najmaei, S., Ajayan, P. M. & Lou, J. Large-Area Vapor-Phase Growth and Characterization of MoS_2 Atomic Layers on a SiO_2 Substrate. *Small* **8**, 966–971 (2012).

52. Liu, K.-K. *et al.* Growth of Large-Area and Highly Crystalline MoS2 Thin Layers on Insulating Substrates. *Nano Lett* **12**, 1538–1544 (2012).

53. Mak, K. F., Lee, C., Hone, J., Shan, J. & Heinz, T. F. Atomically thin MoS2: A new direct-gap semiconductor. *Phys. Rev. Lett.* **105**, 2–5 (2010).

54. Splendiani, A. *et al.* Emerging photoluminescence in monolayer MoS2. *Nano Lett.* **10**, 1271–1275 (2010).

55. Li, T. & Galli, G. Electronic properties of MoS2 nanoparticles. *J. Phys. Chem. C* **111**, 16192–16196 (2007).

56. Böker, T. *et al.* Band structure of MoS2, MoSe2, and α−MoTe2: Angle-resolved photoelectron spectroscopy and ab initio calculations. *Phys. Rev. B* **64**, 235305 (2001).

57. Liu, L., Kumar, S. B., Ouyang, Y. & Guo, J. Performance Limits of Monolayer Transition Metal Dichalcogenide Transistors. *IEEE Trans. Electron Devices* **58**, 3042–3047 (2011).

58. Ding, Y. *et al.* First principles study of structural, vibrational and electronic properties of graphene-like MX2 (M=Mo, Nb, W, Ta; X=S, Se, Te) monolayers. *Phys. B Condens. Matter* **406**, 2254–2260 (2011).

59. Ataca, C., Şahin, H. & Ciraci, S. Stable, single-layer MX 2 transition-metal oxides and dichalcogenides in a honeycomb-like structure. *J. Phys. Chem. C* **116**, 8983–8999 (2012).

60. Coehoorn, R., Haas, C. & de Groot, R. A. Electronic structure of MoSe2, MoS2, and WSe2. II. The nature of the optical band gaps. *Phys. Rev. B* **35**, 6203–6206 (1987).

61. Ramasubramaniam, A. Large excitonic effects in monolayers of molybdenum and tungsten dichalcogenides. *Phys. Rev. B* **86**, 115409 (2012).

62. Kuc, A., Zibouche, N. & Heine, T. Influence of quantum confinement on the electronic structure of the transition metal sulfide TS2. *Phys. Rev. B - Condens. Matter Mater. Phys.* **83**, 1–4 (2011).

63. Zhang, N. *et al.* Moiré Intralayer Excitons in a MoSe2 /MoS2 Heterostructure. *Nano Lett.* **18**, 7651–7657 (2018).

64. Alexeev, M. *et al.* Resonantly hybridized excitons in moiré superlattices in van der Waals heterostructures. *Nature* **567**, 81–86 (2019).

65. Rayleigh, Lord. XII. *On the manufacture and theory of diffraction-gratings*. *London, Edinburgh, Dublin Philos. Mag. J. Sci.* **47**, 81–93 (1874).

66. Guild, J. The interference systems of crossed diffraction gratings : theory of moiré fringes. *Publ. 1956 Oxford by Clarendon Press* 1–152 (1956).

67. Nishijima, Y. & Oster, G. Moiré Patterns: Their Application to Refractive Index and Refractive Index Gradient Measurements. *J. Opt. Soc. Am.* **54**, 1 (1964).

68. Oster, G., Wasserman, M. & Zwerling, C. Theoretical Interpretation of Moiré Patterns. *J. Opt. Soc. Am.* **54**, 169 (1964).

69. Woods, C. R. *et al.* Commensurate–incommensurate transition in graphene on hexagonal boron nitride. **10**, 451–456 (2014).

70. Wallbank, J. R., Mucha-Kruczyński, M., Chen, X. & Fal'Ko, V. I. Moiré superlattice effects in graphene/boron-nitride van der Waals heterostructures. *Ann. Phys.* **527**, 359–376 (2015).

71. Xue, J. *et al.* Scanning tunnelling microscopy and spectroscopy of ultra-flat graphene on hexagonal boron nitride. *Nat. Mater.* **10**, 282–285 (2011).

72. Decker, R. *et al.* Local Electronic Properties of Graphene on a BN Substrate via Scanning Tunneling Microscopy. *Nano Lett.* **11**, 2291–2295 (2011).

73. Yankowitz, M. *et al.* Emergence of superlattice Dirac points in graphene on hexagonal boron nitride. *Nat. Phys.* **8**, 382–386 (2012).

74. Ponomarenko, L. A. *et al.* Cloning of Dirac fermions in graphene superlattices. *Nature* **497**, 594–597 (2013).

75. Dean, C. R. *et al.* Hofstadter's butterfly and the fractal quantum Hall effect in moiré superlattices. *Nature* **497**, 598–602 (2013).

76. Woods, C. R. *et al.* Macroscopic self-reorientation of interacting two-dimensional crystals. *Nat. Commun.* **7**, 1–5 (2016).

77. Binnig, G., Rohrer, H., Gerber, C. & Weibel, E. Surface Studies by Scanning Tunneling Microscopy. *Phys. Rev. Lett.* **49**, 57–61 (1982).

78. Binnig, G. & Rohrer, H. Scanning tunneling microscopy. *Surf. Sci.* **126**, 236–244 (1982).

79. Binnig, G. & Quate, C. F. Atomic Force Microscope. *Phys. Rev. Lett.* **56**, 930–933 (1986).

80. Rugar, D. & Hansma, P. Atomic force microscopy. *Phys. Today* **43**, 23–30 (1990).

81. Bhushan, B. & Marti, O. Scanning Probe Microscopy – Principle of Operation, Instrumentation, and Probes. in *Nanotribology and Nanomechanics* 37–110 (Springer Berlin Heidelberg, 2008).

82. Cellular and Molecular Biomechanics Laboratory. ATOMIC FORCE MICROSCOPY. (2011). Available at: http://biomechanicalregulation-lab.org/afm/.

83. Zhong, Q., Innis, D., Kjoller, K., Elings, V. B., Zhong, Q., Inniss, D., Kjoller, K. & Elings, V. B. Fractured polymer/silica fiber surface studied by tapping mode atomic force microscopy. *Surf. Sci. Lett.* **290**, L688–L692 (1993).

84. Nanosurf. AFM Theory—Contact Modes. Available at: https://www.nanosurf.com/en/how-afm-works/contact-modes.

85. Bruker Corporation. *Introduction to Bruker's ScanAsyst and PeakForce Tapping Atomic Force Microscopy Technology*. 1-12 (2014).

86. Bruker Corporation. Phase Imaging. (2013). Available at: http://www.nanophys.kth.se/nanophys/facilities/nfl/afm/fast-scan/bruker-help/Content/TappingMode AFM/PhaseImaging.htm.

87. Nanosurf. AFM Theory—Dynamic Modes. Available at: https://www.nanosurf.com/en/how-afm-works/dynamic-modes#tapping.

88. Bruker Corporation. TappingMode AFM. (2013). Available at:

http://www.nanophys.kth.se/nanophys/facilities/nfl/afm/fast-scan/bruker-help/Content/TappingMode AFM/TappingMode AFM.htm.

89. Nanosurf. Conductive Atomic Force Microscopy (C-AFM). Available at: https://www.nanosurf.com/en/how-afm-works/conductive-afm-c-afm.

90. Bruker Corporation. Conductive AFM (C-AFM)-Nanoelectrical Characterization Modes. (2013). Available at: https://www.bruker.com/products/surface-and-dimensional-analysis/atomic-force-microscopes/modes/modes/nanoelectrical-modes/c-afm.html.

91. Nanosurf. AFM Modes and Theory—AFM Force Spectroscopy. Available at: https://www.nanosurf.com/en/how-afm-works/force-spectroscopy#mapping.

92. Bruker Corporation. Force Calibration. (2011). Available at: http://www.nanophys.kth.se/nanophys/facilities/nfl/afm/icon/bruker-help/Content/Force Imaging/Force Calibration.htm.

93. Pittenger, B., Erina, N. & Su, C. Quantitative Mechanical Property Mapping at the Nanoscale with PeakForce QNM. *Burker Appl. Note* **128**, 1–12 (2009).

94. Bruker Corporation. Contact Mode Force Calibration. (2011). Available at: http://www.nanophys.kth.se/nanophys/facilities/nfl/afm/icon/bruker-help/Content/Force Imaging/Contact Mode Force Calibration.htm.

95. Bruker Corporation. Force Modulation. (2011). Available at: http://www.nanophys.kth.se/nanophys/facilities/nfl/afm/icon/bruker-help/Content/Force Imaging/Force Modulation.htm.

96. Bruker Corporation. Force Volume. (2011). Available at: http://www.nanophys.kth.se/nanophys/facilities/nfl/afm/icon/bruker-help/Content/ForceVolume/ForceVolRealtime.htm.

97. Bruker Corporation. FASTSCAN-A-Bruker AFM Probes. (2015). Available at: https://www.brukerafmprobes.com/Product.aspx?ProductID=3759.

98. Lin, D. C., Dimitriadis, E. K. & Horkay, F. Robust Strategies for Automated AFM Force Curve Analysis—II: Adhesion-Influenced Indentation of Soft, Elastic Materials. *J. Biomech. Eng.* **129**, 904 (2007).

99. Rashid, A. M. F. & Hossain, Z. Morphological and nanomechanical analyses of ground tire rubber-modified asphalts. *Innov. Infrastruct. Solut.* **1**, 36 (2016).

100. Maugis, D. *Contact, adhesion, and rupture of elastic solids*. 99-105 (Springer, 2000).

101. Israelachvili, J. N. *Intermolecular and surface forces*. 253-263 (Academic Press, 2011).

102. Bruker Corporation. SCANASYST-FLUID+-Bruker AFM Probes. (2015). Available at: https://www.brukerafmprobes.com/Product.aspx?ProductID=3728.

103. Sadewasser, S. & Glatzel, T. *Kelvin probe force microscopy: measuring and compensating electrostatic forces*. 11-20 (Springer-Verlag Berlin Heidelberg, 2012).

104. Nabhan, W., Equer, B., Broniatowski, A. & De Rosny, G. A high-resolution scanning Kelvin probe microscope for contact potential measurements on the 100 nm scale. *Rev. Sci. Instrum.* **68**, 3108–3111 (1997).

105. Kelvin, Lord. V. *Contact electricity of metals*. *London, Edinburgh, Dublin Philos. Mag. J. Sci.* **46**, 82–120 (1898).

106. Weaver, J. M. R. & Abraham, D. W. High resolution atomic force microscopy potentiometry. *J. Vac. Sci. Technol. B Microelectron. Nanom. Struct.* **9**, 1559 (1991).

107. Le Ru, E. C. & Etchegoin, P. G. *Principles of surface-enhanced Raman spectroscopy: and related plasmonic effects*. 29-40 (Elsevier, 2009).

108. Colthup, N. B., Daly, L. H. & Wiberley, S. E. *Introduction to infrared and Raman spectroscopy*. 2-8 (Academic Press, 1975).

109. Smith, E. & Dent, G. *Modern Raman spectroscopy: a practical approach*. 23-30 (2004).

110. Malard, L. M., Pimenta, M. A., Dresselhaus, G. & Dresselhaus, M. S. Raman spectroscopy in graphene. *Phys. Rep.* **473**, 51–87 (2009).

111. Harvey, D. 10.6: photoluminescence spectroscopy. 1–12 (2018).

112. HORIBA. Description of a combined/hybrid/hyphenated Raman system. Available at: http://www.horiba.com/en_en/raman-imaging-and-spectroscopy-combined-hybrid-hyphenated-system/.

113. Bonaccorso, F., Sun, Z., Hasan, T. & Ferrari, A. C. Graphene photonics and optoelectronics. *Nat. Photonics* **4**, 611–622 (2010).

114. Pease, R. F. W. Electron beam lithography. **22**, 265–289 (2006).

115. Groves, T. R. Electron beam lithography. *Nanolithography* **3**, 80–115 (2014).

116. Cornell NanoScale Science and Technology Facility. SPIE Handbook, Volume 1: Microlithography, Section 2.1. Available at: http://www.cnf.cornell.edu/cnf_spie1.html#2.1.1.

117. Journal, T., Business, I., Corporation, M., Watson, T. J. & Heights, Y. Electron Resists for Microcircuit and Mask Production. **11**, 1033–1037

118. Landis, S. *Lithography*. 101-182 (John Wiley & Sons, 2013).